PRACTICAL CONSIDERATION

FOR APPLICATION OF FAST MARCHING METHOD

INTO HETEROGENEOUS DUAL POROSITY RESERVOIR MODELS

A Thesis

by

KENTA NAKAJIMA

Submitted to the Office of Graduate and Professional Studies of
Texas A&M University
in partial fulfillment of the requirements for the degree of

MASTER OF SCIENCE

Chair of Committee,	Akhil Datta-Gupta
Committee Members,	Michael J. King
	Debjyoti Banerjee
Head of Department,	A. Daniel Hill

December 2017

Major Subject: Petroleum Engineering

ABSTRACT

The shale oil/gas is one of the most prospective natural resources due to its huge amount of reserves, and, thus, its development plays a role in making a great contribution to resolve the problem of energy deficiency all over the world. However, because of the uniqueness of shale reservoirs, it is by no means easy to expect reservoir performance from current commercial reservoir simulators. Hence, the improvement of practical shale reservoir simulators is significant to make progress on the development of shale reservoirs. As for this, Fast Marching Method has shown its strength of fast prediction of reservoir performance. This research employs two approaches to improve the applicability of Fast Marching Method: the use of Multistencil Fast Marching and the application of Fast Marching Method into heterogeneous dual porosity models.

In this study, Multistencil Fast Marching Method is employed to improve the accuracy of Diffusive Time of Flight (DTOF) calculation. Originally, Fast Marching Method has taken into account only directly adjacent cells to derive DTOF, which ends up with smaller transmissibility than that of commercial softwares. In case of Multistencil Fast Marching Method, the derivation of more accurate DTOF is achieved by considering the diagonal cells in addition to the directly adjacent cells. In the following study, Fast Marching Method is applied into heterogeneous dual porosity reservoir models (DPSP). In this model, Fast Marching grids are generated based on DTOF of fracture. Matrix grids are supposed to belong to their fracture grids. Thus, appropriate averaging methods for matrix

properties need to be investigated so that it selects most representative parameters among heterogeneous matrices. Subsequently, Fast Marching Method is extended to multiple phase reservoir models, and then some case studies not only with heterogeneous matrix properties but also with heterogeneous fracture properties are conducted in order to show the robustness of this method. Lastly, the field application was conducted to show the wide applicability of FMM.

DEDICATION

To my family: Yuka, Tetsuya, Yoko, Shinichi and Yoshiko

ACKNOWLEDGEMENTS

I would like to thank my advisor, Dr. Datta-Gupta, and my committee members, Dr. King and Dr. Banerjee for their supports.

I would like to acknowledge the help and instruction from Dr. Kurihara during my undergraduate days at Waseda University and his recommendation into this research group in Texas A&M University.

I would like to show my gratitude to Atsushi Iino for his enthusiastic guidance regarding my research analysis.

Thank you, my friends, research group members, the department faculty and staff for making my life at Texas A&M University fruitful.

Finally, I would like to acknowledge the support from my family members.

CONTRIBUTORS AND FUNDING SOURCES

Contributors

This work was supervised by a thesis committee consisting of Professors Akhil Datta-Gupta. [advisor] and Michael J. King. Holditch [committee member] of the Department of Petroleum Engineering and Professor Debjyoti Barnerjee [committee member] of the Department of Mechanical Engineering at Texas A&M University.

All other work conducted for the thesis was completed by the student independently.

Funding Sources

There are no outside funding contributions to acknowledge related to the research and compilation of this document.

TABLE OF CONTENTS

Page

LIST OF FIGURES

Page

LIST OF TABLES

Page

CHAPTER I

INTRODUCTION AND OBJECTIVES

1.1 Characteristics of Unconventional Reservoirs

Shale gas and oil are categorized into one of the most typical unconventional resources with huge reserves. More in detail, in terms of the reserves, the EIA (2013) estimates that technically recoverable shale oil is composed of 58 billion barrels of crude oil, which occupies about 26% of the total domestic oil reserves in the U.S. As for the shale gas, technically recoverable shale gas is estimated to be composed of 665 trillion cubic feet of natural gas, which is as much as 27% of the total domestic natural gas reserves in the U.S. From the viewpoint of the amount of annual production, the shale gas and oil production compose approximately 29% of the total domestic U.S. crude oil production and 40% of the total domestic U.S. natural gas production in 2012.

Previously, shale reservoirs were not considered to be pay zones due to their complex nature. The main difficulty in producing shale gas and oil is its extremely small pore throat. In 2009, Nelson investigated the distribution of the size of the pore throat in shales, sandstones and tight sands. According to the study, the size of pore throat in conventional sandstones distributes from 2 to 20 μm, and that of tight sand ranges between 20 nm to 1 μm. However, that of shales ranges from 5 to 100 nm, which is about 100 times smaller compared to that of conventional sandstones.

In addition to the extremely small pore throat, there remains uniqueness which makes shale production more complicated. The main difficulties are summarized below: (1) high capillarity due to large surface area in pores, (2) highly heterogeneous media because of the existence of the inorganic / organic matters, (3) adsorption / desorption from the surface of organic rocks, (4) Knudsen diffusion and slippage effect in matrices, (5) complex geomechanics of fracture system, and (6) turbulent flow in hydraulic fractures and perforation. Because of these complexities above, it was considered to be unrealistic to produce oil and gas from shale zones.

However, shale oil and gas became technically available due to the enhancement of the production efficiency. There are mainly three factors which enabled shale gas and oil evolution: the improvement of drilling technology, the enhancement of completion and the deeper understanding of the transport mechanism in shale reservoirs. The first contribution factor to shale gas and oil evolution is the improvement of drilling technology, which is the development of horizontal wells. In general, the advantage of horizontal wells is as follows: increased production rate due to bigger wellbore length, reduced pressure drop at the wellbore, reduced sand production originating from lower velocity at the wellbore, reduced gas and water coning and larger drainage volume. According to Browning et al. (2013), almost all the wells were drilled vertically until the early 2000s. However, in the first 7 months of 2011, approximately 98% of wells had been changed into horizontal. The second contributing factor to the success of shale evolution is the development of the completion technique, which means efficient multistage hydraulic fracturing. The main advantage of this method is as follows: to increase flow rate at

extremely low permeability reservoirs, to increase stimulated drainage volume and to decrease the pressure drop at the production wells. Recently, multistage hydraulic fracturing technique has been widely applied in several U.S. shale plays such as Bakken, Barnett, Eagle Ford, Haynesville, Marcellus, Utica, Marcellus and Niobrara. The last factor is deeper understanding of fluid transport mechanism in shale reservoirs. The unique flow characteristic of shale reservoirs originates from the nano-scale pore structure. This structure plays two important roles in shale gas reservoirs: larger exposed surface area and the exception from Darcy's law. First of all, due to the nano-scale pore, the exposed surface area is much larger than that of micropores with the same pore volume, which promotes more absorption of gas into the surface. Suppose all the pores have ideally spherical shape and gas molecules are absorbed into the pore surface. In this case, the volume of free gas is equal to the pore volume, $4\pi r^3/3$, where r represents the radius of the pore itself. On the other hand, the absorbed gases are stuck into the pore surface, which is equal to $4\pi r^2$. This fact suggests the importance of pore surface which gases can be absorbed into. The second critical characteristic of nano pore is the exception from Darcy's law. In case of conventional black oil type reservoirs, Darcy's law is considered to be the underlying governing law for fluid flow. This assumption is valid only under the conditions listed below:

(1) Flow direction aligns with that of pressure gradient (convective transport).

(2) Laminar flow condition

(3) No slippage effect and diffusion on pore wall.

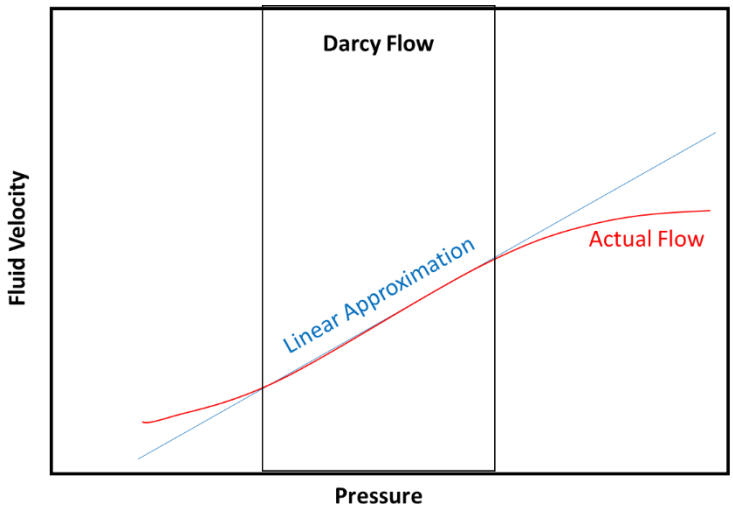

Fig. 1.1 – Fluid Velocity with respect to Pressure (Adapted from Klinkenberg et al. 1941)

The figure above illustrates the relationship between Darcy's approximation and actual fluid velocity. In this figure, the black curve represents the actual velocity of gas phase with respect to each pressure. On the other hand, the red dot curve represents fluid velocity approximated by Darcy's law. From the figure above, there are deviations in high and low pressure zones. In the high pressure region, this deviation is caused from turbulent flow called Forchheimer flow, which contradicts to the assumption of laminar flow condition. This is common in the perforations or fractures near wellbores. In contrast, in the low pressure region, the deviation is originated from slippage and Knudsen diffusion. As for the slippage effect, Klinkenberg (1941) observed gas slippage at the surface of porous media and noticed that the gas flow rate significantly deviates from that of Darcy's law in the extremely low pressure region. This phenomenon occurs under the very low pressure usually below 1,000 psia or in nanodarcy-scale permeable regions. In his study, he

proposed the following relationship between them to take into consideration the slippage effect.

$$k_{app} = k_{\infty}\left(1 + \frac{b}{P}\right) \tag{1.1}$$

In the above equation, k_{∞} represents Darcy's permeability and b represents the slippage factor. As for this factor, several authors have conducted experiments to decide the constant value (Jones et al. 1980, Sampath et al. 1982, Ertekin et al. 1986, Florence et al. 2007, Javadpour et al. 2007, Civian 2010, Michel et al. 2011, Swami et al. 2012).

From the viewpoint of the unique characteristics described above, the research focuses on the development of fast shale gas and oil simulator which can consider the complex nature of shale reservoirs.

1.2 Asymptotic Approach

In order to maximize the profit and to reduce the risk of oil and gas production, it is essential for reservoir engineers to reduce uncertainties when they take charge of field explorations. Generally, the tasks of reservoir engineers can be composed of two parts: inverse modeling and forward modeling. Inverse modeling is the process to match the past behavior of actual wells with that of simulated wells, and so it is commonly called history matching. The objective of this process is to improve the reservoir models the reservoir engineers have previously estimated. In comparison with the actual well performance and the simulated well performance based on the estimated reservoir model, they need to select the best estimated realization model which generates closest well performance to that of actual wells. This process requires trial and error to compare all the realization models and

select the best one which is closest to the actual reservoir among them, and thus, it usually takes long time to obtain the best match. Thus, the development of the fast reservoir simulators can promote the inverse modeling process. The next task of reservoir engineers is called forward modeling. This process is to forecast the future well performance and includes reservoir optimizations. Based on the assumption that the history matching conducted above should be accurate, reservoir engineers try to optimize the well performance and to maximize the oil and gas production in the future. For instance, the construction of new wells is one of the most common forward modeling processes. In order to select the best new well locations, it is also required to run reservoir simulators repeatedly, which accordingly takes a long time as well. In both inverse and forward modeling, the development of fast reservoir simulators can improve the efficiency of reservoir engineering tasks and make it possible to test more realization models, which finally results in the reduction of uncertainties.

Usually, the conventional finite difference-based reservoir simulators are widely used to conduct the inverse and the forward modeling processes. This simulator is assumed to be most accurate, but it takes too long to conduct these modeling processes. Regarding the history matching process, it takes at least one month to get the best realization model whose well performance is close to that of actual wells. As for the computational time, streamline-based flow simulators were considered to be the best solution for the problem. The principal concept is the decomposition of multidimensional governing equations into 1-D equations based on convective time of flight (TOF). This method has shown its strength in terms of visualization of flow paths and its short computational time. However,

in order to apply this approach, it is required to obtain flux field at every time step, which means it is not useful to forecast the reservoir performance in transient flow regime with streamline method. As for shale reservoirs, it is more important to forecast transient flow regime rather than to estimate pseudo steady flow regime. This is because, in the case of shale reservoirs, transient flow regime tends to be long-lasting due to its extremely small permeability, whereas this regime quickly gets through for conventional reservoirs. Because of the reason above, it is necessary to develop alternative fast reservoir simulators, which is applicable for shale reservoirs to realize more efficient inverse and forward modeling processes.

As for the problem of computational time, the asymptotic approach based on Fast Marching Mehtod (FMM) is proposed as an alternative solution. This method originates from the concept of 'radius of investigation'. Lee (1982) defined radius of investigation as the propagation distance of peak pressure disturbance from an impulse sink or source point, which means injection or production wells. Outside of the radius, the impact of pressure disturbance is assumed to be negligible. According to the original definition of radius of investigation, this can be calculated under the limitation that the reservoir has homogeneous and isotropic properties, so it was not practical in the actual field exploration at first. However, Datta-Gupta et al. (2011) generalized this concept to take into account the application into heterogeneous reservoirs by introducing the theory of diffusive time of flight (DTOF) which represents the travel time of peak pressure front. This theory regards the pressure propagation as wave propagation and transforms diffusivity equation into Eikonal equation in terms of pressure front. The asymptotic solution can be efficiently

obtained in use of FMM. FMM is a class of front tracking algorithm to solve Eikonal equation and the concept is similar to Dijkstra algorithm (1959) which calculates the shortest path from the source point. Making use of DTOF, the corresponding drainage volume can be efficiently calculated. Through the process, the 3-D spatial coordinate can be converted into a 1-D coordinate along DTOF. In the end, the reduction of dimension can realize the reduction of computational time. In this research, FMM-based reservoir simulator is developed further in terms of its accuracy and its applicability for shale reservoirs.

1.3 Research Outline

There are two objectives in this research: improvement of accuracy of FMM and broadening its applicability.

In Chapter II of this study, Multistencil Fast Marching Method is employed to improve the accuracy of Diffusive Time of Flight (DTOF) calculation. Originally, FMM has taken into account only directly adjacent cells to derive DTOF, which ends up with smaller transmissibility than that of commercial software. In this research, the derivation of more accurate DTOF is achieved by considering the diagonal cells in addition to the directly adjacent cells.

In Chapter III of this study, Fast Marching Method is applied into heterogeneous dual porosity reservoir models (DPSP). In this model, Fast Marching grids are generated based on DTOF of fracture, and matrix grids are supposed to belong to their fracture grids. Thus,

appropriate averaging methods for matrix properties need to be investigated so that it selects the most representative parameters among heterogeneous matrices.

In Chapter IV of this study, Fast Marching Method is extended to multi-phase reservoir models. In this case, it is necessary to consider more parameters to be averaged so that mass balance in each grid should be preserved. Next, some case studies are conducted not only with heterogeneous matrix properties but also with heterogeneous fracture properties in order to show the robustness of this method. Finally, the wide applicability of FMM is proved in the use of the actual reservoir field data.

CHAPTER II

THE USE OF MULTISTENCIL FAST MARCHING METHOD

2.1 Introduction to Fluid Flow Mechanism

Fluid flow mechanism in porous media is governed by the following fundamental equations: mass conservation, momentum equation and equation of state. The fluid transport equation is based on the assumption that diffusion and dispersion effects are small enough to be ignored compared to convective flux. Besides, no chemical reaction is assumed. In this chapter, the fluid flow equation is derived from the three fundamental equations under the assumptions. First of all, mass conservation means that the mass in a closed system should be constant unless there is production from the system or injection into it. For the purpose of simplicity, we consider mass conservation equation under the single phase flow shown below:

$$\frac{\partial(\phi\rho)}{\partial t} = -\nabla \bullet (\rho \mathbf{u}) \tag{2.1}$$

where ϕ represents porosity, ρ represents fluid density, t represents time and $\mathbf{u}$ is the Darcy velocity, respectively. In the above equation, Left Hand Side (LHS) represents the derivative of mass in the target cell by time. On the other hand, Right Hand Side (RHS) represents the flux into the cell. This equation suggests that the amount of the mass accumulated in each cell is equal to the amount of mass flux into or from the cell per time. In the 3-D Cartesian grid system, since fluid density is scalar property and Darcy velocity has its own direction, RHS can be transformed into the following form.

$$\nabla \bullet \mathbf{u} = \frac{\partial u_x}{\partial x} + \frac{\partial u_y}{\partial y} + \frac{\partial u_z}{\partial z} \tag{2.2}$$

In addition to the equation above, there are two conditions to complete the equation: inner boundary condition and outer boundary condition. The inner boundary condition is given as sink or source term which means injection or production well in the system. The outer boundary condition is usually supposed to be a no-flow boundary in a closed domain.

As for the second governing equation, momentum equation, it is expressed below in the use of linear fluid flow approximation (Darcy's law). For the sake of simplicity, ignore gravity term.

$$\mathbf{u} = -\frac{\mathbf{k}}{\mu}\nabla P \tag{2.3}$$

This equation above states that the amount of fluid flow has a linear relationship with the pressure gradient and its direction is along the pressure gradient direction. Substituting the above equation into **Eq. (2.1)**, the following form can be obtained.

$$\frac{\partial(\phi\rho)}{\partial t} = \nabla \bullet \left(\rho \frac{\mathbf{k}}{\mu}\nabla P\right) \tag{2.4}$$

Lastly, the third principal equation, equation of state, explains the relationship between static properties such as volume or density, and the system condition such as pressure or temperature. As for the fluid density, it can be approximated in the use of Taylor series expansion. In the case of slightly compressible flow, fluid density is expressed in the form of linear approximation in terms of pressure, neglecting second or higher order terms:

$$\rho = \rho^o e^{c_f(P-P^o)} \approx \rho^o \left(1 + c_f(P - P^o)\right) \tag{2.5}$$

where ρ^o and P^o represent the reference fluid density and pressure and c_f is a fluid compressibility, respectively. On the other hand, volume, which corresponds to porosity, is transformed into the equation below:

$$\phi = \phi e^{c_r(P-P^o)} \approx \phi^o\left(1 + c_r(P - P^o)\right) \tag{2.6}$$

where c_r represents rock compressibility. Substituting **Eq. (2.5)** and **(2.6)** into **Eq. (2.4)** leads to the well-known diffusivity equation for slightly-compressible fluids.

$$\phi(\mathbf{x})\mu c_t \frac{\partial P(\mathbf{x},t)}{\partial t} = \nabla \bullet \left(k(\mathbf{x})\nabla P(\mathbf{x},t)\right) \tag{2.7}$$

On the other hand, in the case of compressible fluid (gas case), the approximation is not valid and fluid compressibility is no longer constant. In this case, the equation of state is derived from the real gas law.

$$\rho = \frac{PM_w}{zRT} \tag{2.8}$$

where M_w, z and R represent molecular weight, compressibility factor and universal gas constant, respectively. Using **Eq. (2.8)** instead of **Eq. (2.5)**, the diffusivity equation for gas flow is expressed below.

$$\phi(\mathbf{x})\mu c_t \frac{\partial m(\mathbf{x},t)}{\partial t} = \nabla \bullet \left(k(\mathbf{x})\nabla m(\mathbf{x},t)\right) \tag{2.9}$$

Where

$$m(\mathbf{x},t) = 2\int_{P^o}^{P} \frac{P}{z\mu} dP \tag{2.10}$$

2.2 Methods: Asymptotic Approach

2.2.1 Asymptotic Pressure Solution

In the case of single phase and slightly compressible fluid, the fluid flow mechanism is governed by the diffusivity equation shown in the previous chapter. **Eq. (2.7)** can be further expanded into **Eq. (2.11)**.

$$\phi(\mathbf{x})\mu c_t \frac{\partial P(\mathbf{x},t)}{\partial t} = \nabla k(\mathbf{x}) \bullet \nabla P(\mathbf{x},t) + k(\mathbf{x}) \bullet \nabla^2 P(\mathbf{x},t) \tag{2.11}$$

From the equation shown above, we consider a conversion with respect to frequency domain in the use of Fourier transformation:

$$\tilde{P}(\mathbf{x},\omega) = \int_{-\infty}^{\infty} P(\mathbf{x},t) e^{-i\omega t} dt \tag{2.12}$$

$$= e^{-\sqrt{-i\omega}\tau(\mathbf{x})} \sum_{k=0}^{\infty} \frac{A_k(\mathbf{x})}{\left(\sqrt{-i\omega}\right)^k} \tag{2.13}$$

where $\tau(\mathbf{x})$ is the phase of a propagating wave, which describes the geometry of a propagation front and $A_k(\mathbf{x})$ corresponds to the amplitude of the wave. The equation above can be interpreted based on the physical scale of each term. The solution of **Eq. (2.13)** is expressed as the sum of infinite number of $\frac{A_k(\mathbf{x})}{\left(\sqrt{-i\omega}\right)^k}$. However, from the view point of scale, the most important physical quantity is represented only in the first order term especially in the high frequency zone. Thus, **Eq. (2.13)** can be approximated as follows.

$$\tilde{P}(\mathbf{x},\omega) = e^{-\sqrt{-i\omega}\tau(\mathbf{x})} A_0(\mathbf{x}) \tag{2.14}$$

The first order and the second order derivative of $\tilde{P}(\mathbf{x},\omega)$ with respect to x is expressed below.

$$\nabla\tilde{P}(\mathbf{x},\omega) = -\sqrt{-i\omega}\nabla\tau(\mathbf{x})e^{-\sqrt{-i\omega}\tau(\mathbf{x})}A_0(\mathbf{x}) + e^{-\sqrt{-i\omega}\tau(\mathbf{x})}\nabla A_0(\mathbf{x}) \tag{2.15}$$

$$\begin{aligned}\nabla^2\tilde{P}(\mathbf{x},\omega) = {} & (-i\omega)\left(\nabla\tau(\mathbf{x})\right)^2 e^{-\sqrt{-i\omega}\tau(\mathbf{x})}A_0(\mathbf{x}) \\ & - \sqrt{-i\omega}\nabla^2\tau(\mathbf{x})e^{-\sqrt{-i\omega}\tau(\mathbf{x})}A_0(\mathbf{x}) \\ & - 2\sqrt{-i\omega}\nabla\tau(\mathbf{x})e^{-\sqrt{-i\omega}\tau(\mathbf{x})}\nabla A_0(\mathbf{x}) + e^{-\sqrt{-i\omega}\tau(\mathbf{x})}\nabla^2 A_0(\mathbf{x})\end{aligned} \tag{2.16}$$

On the othrer hand, **Eq. (2.11)** can be transformed below in terms of frequency.

$$\phi(\mathbf{x})\mu c_t(-i\omega)\tilde{P}(\mathbf{x},\omega) = \nabla k(\mathbf{x}) \bullet \nabla\tilde{P}(\mathbf{x},\omega) + k(\mathbf{x}) \bullet \nabla^2\tilde{P}(\mathbf{x},\omega) \tag{2.17}$$

Substituting **Eq. (2.14) - Eq. (2.16)** into **Eq. (2.17)** leads to the following quadratic equation in terms of $\sqrt{-i\omega}$.

$$\begin{aligned}&[\phi(\mathbf{x})\mu c_t - k(\mathbf{x})\nabla^2\tau(\mathbf{x})]A_0(\mathbf{x})\left(\sqrt{-i\omega}\right)^2 \\ &+[k(\mathbf{x})\nabla^2\tau(\mathbf{x})A_0(\mathbf{x}) + 2k(\mathbf{x})\nabla\tau(\mathbf{x})\nabla A_0(\mathbf{x}) + \nabla k(\mathbf{x})\nabla\tau(\mathbf{x})A_0(\mathbf{x})]\sqrt{-i\omega} \\ &-[\nabla k(\mathbf{x})\nabla A_0(\mathbf{x}) + k(\mathbf{x})\nabla^2 A_0(\mathbf{x})] = 0\end{aligned} \tag{2.18}$$

Since both LHS and RHS should be equal with respect to each term, all of the coefficients should be zeros. Thus, the coefficient of the first order term should be also zero, which leads to the propagation equation shown below.

$$\phi(\mathbf{x})\mu c_t - k(\mathbf{x})\nabla^2\tau(\mathbf{x}) = 0 \tag{2.19}$$

$$\nabla\tau(\mathbf{x}) \bullet k(\mathbf{x}) \bullet \nabla\tau(\mathbf{x}) = \phi(\mathbf{x})\mu c_t \tag{2.20}$$

In use of diffusivity $\alpha_{\text{diff}}(\mathbf{x})$, this equation can be further transformed below.

$$|\nabla\tau(\mathbf{x})|\sqrt{\alpha_{\text{diff}}(\mathbf{x})} = 1 \tag{2.21}$$

where

$$\alpha_{\text{diff}}(\mathbf{x}) = \frac{k(\mathbf{x})}{\phi(\mathbf{x})\mu c_t} \tag{2.22}$$

In the above equation, the physical meaning of diffusivity is the propagation speed of the peak pressure disturbance. It is worth noting that **Eq. (2.21)** has a form of well-known Eikonal equation governing wave propagation behavior. By integrating throughout the whole trajectory of pressure propagation,

$$\tau(\mathbf{x}) = \int_{\Sigma} \frac{1}{\sqrt{\alpha_{\text{diff}}(\mathbf{x})}} dr \tag{2.23}$$

where Σ denotes all the trajectory of pressure propagation. The above equation means the pressure front with the velocity of $\sqrt{\alpha_{\text{diff}}(\mathbf{x})}$. By imitating the concept of the convective time of flight (CTOF) used in the streamline simulation, Datta-Gupta et al. (2001) defined $\tau(\mathbf{x})$ as 'diffusive time of flight (DTOF)' with the unit of the square root of time. As Vasco and Finstele pointed out (2004), the corresponding trajectory does not have the form of streamlines in transient flow regime.

2.2.2 Fast Marching Method

Eq. (2.20) denotes that the travel time of pressure front is inversely proportional to square root of diffusivity, $\alpha_{\text{diff}}(\mathbf{x})$, which corresponds to velocity of propagation speed. This equation has a form of Eikonal equation, and this can be efficiently solved in the use of the algorithm called Fast Marching Method (FMM). This algorithm is a class of front tracking methods proposed by Sethian (1996). The principal algorithm is summarized below.

(1) Label all node points as '*unknown'*.

(2) Initialize the nodes corresponding to the start points of the pressure front to zeros and label them as '*accepted'*.

(3) For each accepted node point, locate its immediate neighboring nodes with the label of '*unknown'* and update their status as '*considered'*.

(4) For each node in the status of '*considered'*, update its τ calculated from its '*accepted'* neighbors using the local minimum solution of **Eq. (2.20)**.

(5) Once all nodes labeled '*considered'* have been updated, we select the node which has the minimum τ among them and attach the label as '*accepted'*.

(6) Go to step (3) until all nodes become '*accepted'*.

For the purpose of simplicity, consider the 2-D 5-stencil Cartesian grid model. In this case, the process explained above is illustrated below (Xie et al. 2012). First of all, the starting point of the pressure propagation is labeled as '*accepted'* and initialized into zero as described in **(a)**. Next, its immediate neighbor A, B, C, and D are labeled as '*considered'*, and their values are updated from their neighboring '*accepted'* point based on the solution of **Eq. (2.20)**, whose process corresponds to **(b)**. After all the τ in points A, B, C and D have been updated, the smallest τ among them, which is supposed to be A in the figure below, is selected, and its label is changed into '*accepted'* as described in **(c)**. In step **(d)** in the figure, its neighboring nodes, E, F and G are added into newly '*considered'* lists. The series of the updating process (**(b)** and **(c)**) is to be continued until the next '*accepted'*

point, which is supposed to be D in the figure **(e)** and **(f)**, is obtained. Finally, the overall flow described here is to be repeated until all the nodes are labeled as '*accepted'*.

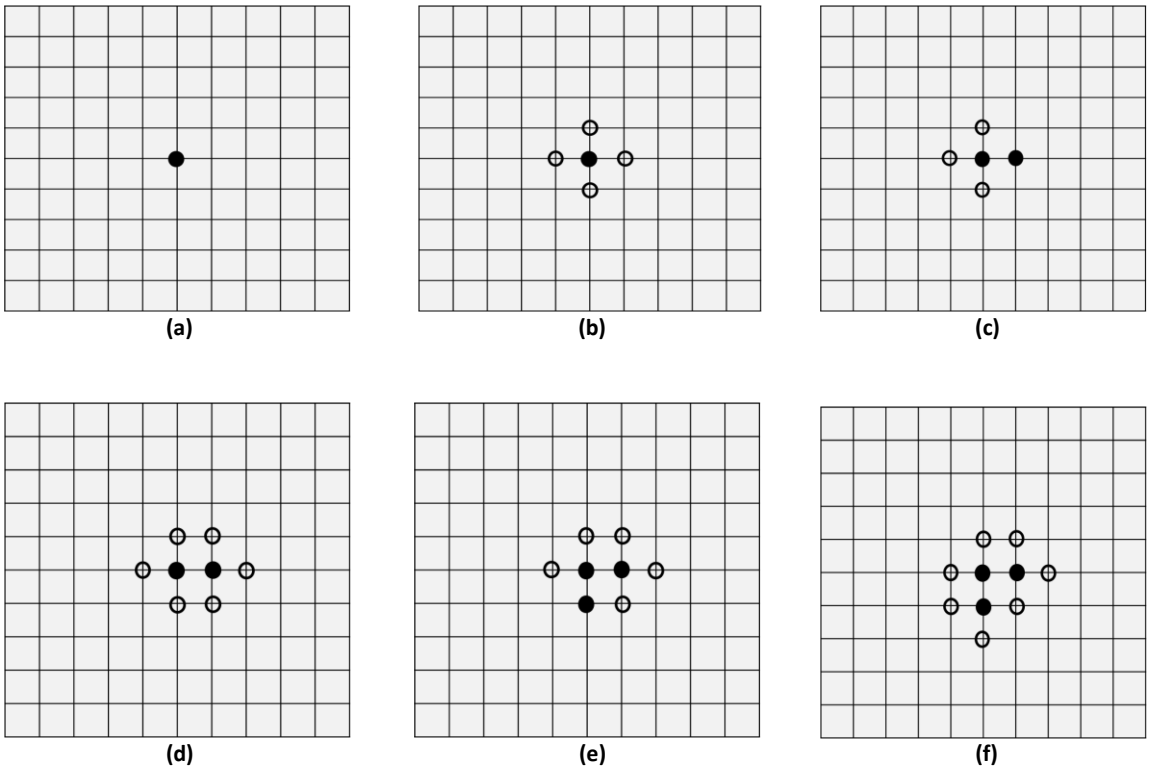

Fig. 2.1 – Illustration of Fast Marching Method (Adapted from Xie et al. 2012)

As for the minimum local solution of **Eq. (2.20)**, it can be calculated from the standard finite difference equation shown below (Sethian 1996).

$$\max\left(D_{ij}^{-x}\tau, -D_{ij}^{+x}\tau, 0\right)^2 + \max\left(D_{ij}^{-y}\tau, -D_{ij}^{+y}\tau, 0\right)^2 = \frac{1}{\alpha_{\text{diff}}} \tag{2.24}$$

In the case of original FMM calculation, D represents a gradient of finite difference scheme approximated with first order truncation error. For the purpose of simplicity, assume the 5-stencil FMM for 2-D Cartesian grid model. In this case, $D_{ij}^{-x}\tau =$

$\left(\tau_{i,j} - \tau_{i-1,j}\right)/\Delta x$ and $D_{ij}^{+x}\tau = \left(\tau_{i+1,j} - \tau_{i,j}\right)/\Delta x$. The same equations hold in the y-direction as well: $D_{ij}^{-y}\tau = \left(\tau_{i,j} - \tau_{i,j-1}\right)/\Delta y$ and $D_{ij}^{+y}\tau = \left(\tau_{i,j+1} - \tau_{i,j}\right)/\Delta y$.

It is worth noting that τ solutions are calculated in the ascending order, which describes the propagation of peak pressure disturbance in the reservoir. Hence, this transformation enables to define drainage pore volume as the pore volume inside the range of τ contour. In this way, the drainage pore volume can be visually grasped even in case of heterogeneous reservoirs, which is one of the strengths of FMM.

2.2.3 Multistencil FMM

As mentioned in the above section, original FMM calculation is expressed in **Eq. (2.24)**. In a more general form it can be expressed as follows.

$$\sum_{\gamma=1}^{n} max(\frac{\tau - \tau_\gamma}{\Delta_\gamma}, 0)^2 = \frac{1}{(\sqrt{\alpha})^2} \tag{2.25}$$

Or it can be expressed below by dividing both sides of the denominators by $(\sqrt{\alpha})^2$:

$$\sum_{\gamma=1}^{n} max(\frac{\tau - \tau_\gamma}{\frac{\Delta_\gamma}{\sqrt{\alpha}}}, 0)^2 = 1 \tag{2.26}$$

where n corresponds to the reservoir dimension (i.e. if the reservoir model is 2-D, n is two and if 3-D, n is three), Δ_γ represents the distance between the known node and the target node and τ_γ denotes DTOF at each known point. It is important to notice that the diffusivity, α, is dependent on the grid and fluid dependent parameters, and thus it takes a different value grid by grid in the heterogeneous reservoir models. For the purpose of simplicity, we begin with the 2-D case illustrated below.

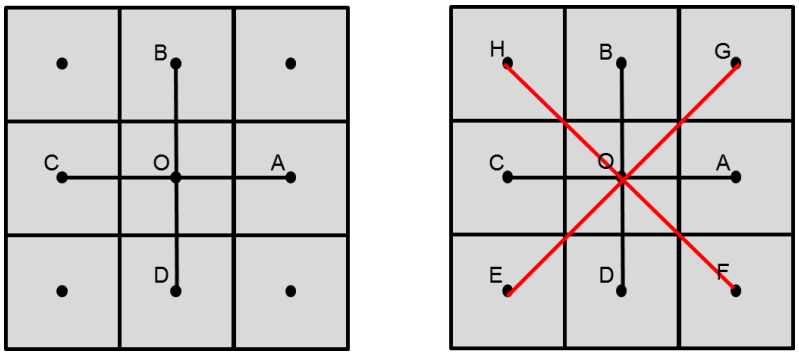

Fig. 2.2 – Illustration of Multistencil Fast Marching Method for 2-D (7-stencil, Left and 9-stencil, Right)

In the 2-D case, n should be equal to one and τ_γ is expressed below.

$$\tau_1 = \min(\tau_{i-1,j}, \tau_{i+1,j}) \tag{2.27}$$

$$\tau_2 = \min(\tau_{i,j-1}, \tau_{i,j+1}) \tag{2.28}$$

Eq. (2.25), **(2.27)** and **(2.28)** denote that in order to calculate the unknown value at node point O, it considers four node points A, B, C and D, thus it is commonly known as 5-stencil FMM. In its calculation, to solve **Eq. (2.25)**, consider the four triangles OAD, OAB, OBC and OCD. Based on these triangles, calculate four DTOF at unknown point O, and then select the smallest DTOF among them. Each triangle assumes the case when the pressure front arrives at the node point O from a different direction. For instance, the triangle OAD assumes that the peak pressure disturbance from the well comes from the direction between A and D, which means the pressure front is assumed to be almost parallel to AD.

On the other hand, multi-stencil FMM takes into account not only the triangles listed above, but also the triangles OEF, OFG, OGH and OHE. Among these 8 calculated DTOF,

pick up the smallest one as the final value at unknown point O. This denotes that multi-stencil FMM considers more directions where the pressure disturbance comes. Accordingly, the calculated DTOF at the node O should be smaller and more accurate than that of the original 5-stencil FMM.

Next, in the case of 3-D reservoir models, **Eq. (2.25)**, **(2.27)** and **(2.28)** become as follows.

$$\sum_{\gamma=1}^{3} max(\frac{\tau-\tau_\gamma}{\Delta_\gamma}, 0)^2 = \frac{1}{(\sqrt{\alpha})^2} \tag{2.29}$$

where

$$\tau_1 = \min(\tau_{i-1,j,k}, \tau_{i+1,j,k}) \tag{2.30}$$

$$\tau_2 = \min(\tau_{i,j-1,k}, \tau_{i,j+1,k}) \tag{2.31}$$

$$\tau_3 = \min(\tau_{i,j,k-1}, \tau_{i,j,k+1}) \tag{2.32}$$

As represented in the above equations, the multi-stencil FMM needs to consider more cases to update the unknown node. In total, in order to calculate DTOF at the unknown node, 26 stencils are considered on top of the unknown node, and this is why multi-stencil FMM in 3-D is also called 27 stencil FMM. On the other hand, the original FMM takes into account only the 6 stencils, $\pm$x, $\pm$y, $\pm$z, to obtain the unknown. Thus, it is called 7-stencil FMM as well.

As for the computational time, since multi-stencil FMM needs to consider more triangles than 5-stencil FMM, it takes a longer time to solve the Eikonal equation. However, throughout the overall calculation of the fluid flow simulation, the part of FMM calculation accounts for only a small portion of computational time because it takes the

longest for pressure calculation based on derived FMM grid coordinates. Thus, overall elapsed time does not change a lot even when multi-stencil FMM is conducted instead of 5-stencil.

2.2.4 Advantage of Multistencil FMM

In the above section, the algorithm of multi-stencil FMM is explained. In this section, the advantages of multi-stencil FMM is described. There are two main advantages to use multi-stencil FMM: the accuracy and the causality issue.

The first merit is its accuracy of calculated DTOF. This can be easily understood considering the 2-D homogeneous case.

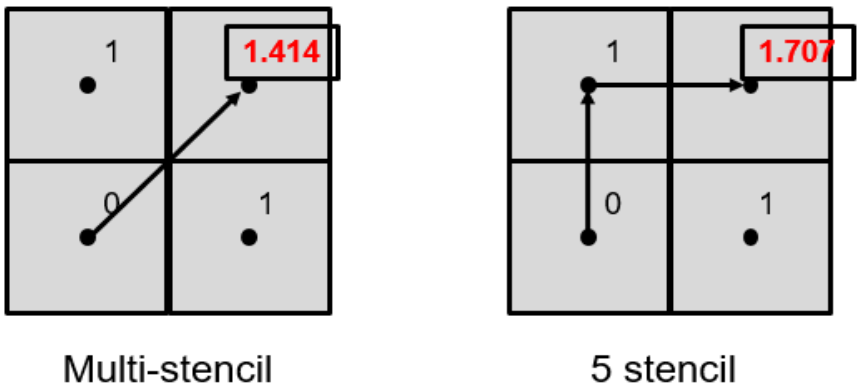

Fig. 2.3 – Comparison of 7-stencil FMM with 5-stencil FMM for the Homogenous Case

The figure demonstrated above illustrates the DTOF based on multi-stencil FMM and the original 5-stencil FMM in the case of 2-D homogeneous case. The upper right node point is supposed to be unknown, and the lower left is assumed as the source of pressure disturbance in both of the cases. As for multi-stencil FMM, the DTOF at the destination

point is first calculated at the same time with the upper left point and the lower right point based on the source point. If DTOF at the upper left and the lower right nodes are supposed to be 1 in the 2-D homogeneous model, DTOF at the destination point is calculated as 1.414 based on the source point. On the other hand, in the case of the original 5-stencil FMM, DTOF at the destination point is considered only after DTOF at the upper left and the lower right nodes is derived based on these two DTOF. Accordingly, the DTOF based on the original 5-stencil FMM is bigger than that of the multi-stencil FMM, which leads to smaller transmissibility of fluid flow than the actual one. This will be explained in a later chapter in detail.

The second advantage is causality issue. This problem appears only in heterogeneous reservoir models. Previously, Zhang et al (2013) categorized 12 different high/low permeability patterns for 2 by 2 local solutions. Among them, he pointed out that the error between 5-stencil FMM and the multi-stencil FMM becomes big, especially in the figures described below.

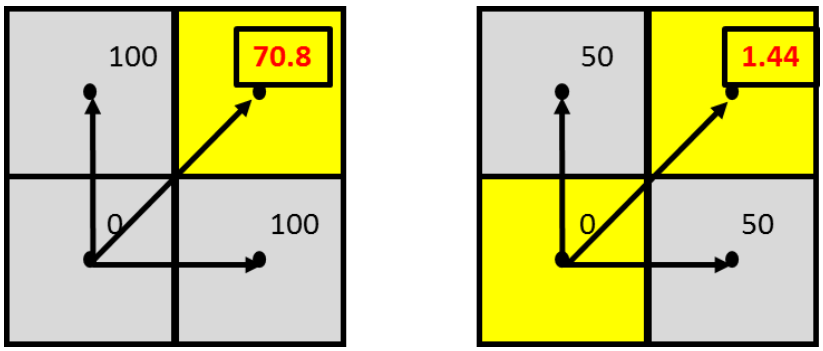

Fig. 2.4 – Illustration of Causality Problem (Adapted from Zhang et al, 2013)

In the above figure, grey cells represent the low permeability grids and the yellow ones denote the grids with high permeability. These cases assume the pressure front comes from the source point at the upper right cell to the destination point at the lower left cell. In both of these cases, the pressure front arrives sooner at the destination point than at its adjacent cells, the upper left and the lower right cell in the use of the multi-stencil FMM. The original 5-stencil FMM starts considering DTOF at the destination point only after DTOF at its adjacent grids are calculated. Thus, Zhang pointed out the 5-stencil FMM might overestimate the travel time due to the local violation of causality, which leads to smaller fluid flow transmissibility between grids.

Because of these reasons, multi-stencil FMM is better than the original 5-stencil FMM in terms of accuracy of DTOF. DTOF based on the multi-stencil FMM is more accurate even in the case of homogeneous reservoirs, and it can prevent local causality violation. In the end, this can lead to more accurate transmissibility between adjacent grids.

2.2.5 FMM with Second Order Truncation Error

As Zhang et al (2014) pointed out, multi-stencil FMM can make a significant contribution to the improvement of accuracy in DTOF calculation. However, in the case of highly heterogeneous reservoirs, the effect of missing higher order terms in the asymptotic solution is no longer negligible. Thus, in this section, the formulation is derived based on the asymptotic solution with higher order truncation errors (Sabry, M., Aly, A., et al. 2007). For the purpose of simplicity, we derive the equation based on the original 5-stencil FMM for the 2-D reservoir model expressed in **Eq. (2.33)**.

$$\max\left(D_{ij}^{-x}\tau, -D_{ij}^{+x}\tau, 0\right)^2 + \max\left(D_{ij}^{-y}\tau, -D_{ij}^{+y}\tau, 0\right)^2 = \frac{1}{\alpha_{\text{diff}}} \tag{2.33}$$

As previously mentioned, the gradient is approximated as follows: $D_{ij}^{-x}\tau = \left(\tau_{i,j} - \tau_{i-1,j}\right)/\Delta x$ and $D_{ij}^{+x}\tau = \left(\tau_{i+1,j} - \tau_{i,j}\right)/\Delta x$. The same equations hold in y-direction as well: $D_{ij}^{-y}\tau = \left(\tau_{i,j} - \tau_{i,j-1}\right)/\Delta y$ and $D_{ij}^{+y}\tau = \left(\tau_{i,j+1} - \tau_{i,j}\right)/\Delta y$.

In this section, consider the approximation with the higher order truncation error. Taylor Series Expansion is expressed below. In the use of the approximation, DTOF at each node is expanded as well.

$$\tau_{i,j} \quad = \tau_{i,j} \tag{2.34}$$

$$\tau_{i-1,j} = \tau_{i,j} - h\,\tau'_{i,j} + \frac{h^2}{2!}\tau''_{i,j} - \frac{h^3}{3!}\tau'''_{i,j} + \cdots \tag{2.35}$$

$$\tau_{i-2,j} = \tau_{i,j} - 2h\,\tau'_{i,j} + \frac{4h^2}{2!}\tau''_{i,j} - \frac{8h^3}{3!}\tau'''_{i,j} + \cdots \tag{2.36}$$

In the use of these three equations, we can approximate the gradient of DTOF.

$$D_{ij}^{-x}\tau = \tau'_{i,j} = \frac{3\tau_{i,j} - 4\tau_{i-1,j} + \tau_{i-2,j}}{h} + O_{(h^2)} \tag{2.37}$$

$$D_{ij}^{-x}\tau \approx \frac{3\tau_{i,j} - 4\tau_{i-1,j} + \tau_{i-2,j}}{2h} \tag{2.38}$$

Substituting these two equation above into **Eq. (2.24)**, the following form can be obtained.

$$\sum_{\gamma=1}^{n} max(\frac{3(\tau - \tau_\gamma^*)}{2\Delta_\gamma}, 0)^2 = \frac{1}{(\sqrt{\alpha})^2} \tag{2.39}$$

Where n is equal to two for 2-D and three for 3-D, respectively. τ_γ^* is expressed below.

$$\tau_1^* = min\left(\frac{4\tau_{i-1,j,k} - \tau_{i-2,j,k}}{3}, \frac{4\tau_{i+1,j} - \tau_{i+2,j,k}}{3}\right) \tag{2.40}$$

$$\tau_2^* = min(\frac{4\tau_{i,j-1,k} - \tau_{i,j-2,k}}{3}, \frac{4\tau_{i,j+1,k} - \tau_{i,j+2,k}}{3}) \tag{2.41}$$

$$\tau_3^* = min(\frac{4\tau_{i,j,k-1} - \tau_{i,j,k-2}}{3}, \frac{4\tau_{i,j,k+1} - \tau_{i,j,k+2}}{3}) \quad (2.42)$$

As a reference, the approximation with first order truncation error is shown below.

$$D_{ij}^{-x}\tau = \tau'_{i,j} = \frac{\tau_{i,j} - \tau_{i-1,j}}{h} + O_{(h)} \quad (2.43)$$

$$D_{ij}^{-x}\tau \approx \frac{\tau_{i,j} - \tau_{i-1,j}}{h} \quad (2.44)$$

$$\sum_{\gamma=1}^{n} max(\frac{(\tau - \tau_\gamma)}{\Delta_\gamma}, 0)^2 = \frac{1}{(\sqrt{\alpha})^2} \quad (2.45)$$

In comparison of **Eq. (2.37)** with **Eq. (2.43)**, you can confirm that the missing error term regarding the approximation in **Eq. (2.37)** is one order higher than that of **Eq. (2.43)**, which means the approximation expressed in **Eq. (2.38)** is more accurate, accordingly. Lastly, it is worth noting that computational time does not change even if the higher order FMM is employed since the number of cases to be considered is the same, unlike the multi-stencil FMM expressed in Fig2.2 and Fig2.3.

2.2.6 Governing Equation in FMM Grids

The governing equation for fluid system in the Cartesian grid model expressed in **Eq. (2.7)** can be transformed into that of the FMM grid model. The DTOF-based fluid flow equation was proposed by Zhang et al. (2014) first. In the process of transformation, the multi-dimensional fluid flow equation can be decomposed into the 1-D equation along τ-contours. This coordinate transformation is based on the assumption that the pressure gradient is along τ gradient direction.

$$\nabla P = \frac{\partial P}{\partial \tau} \nabla \tau \quad (2.46)$$

Furthermore, the grid permeability, which appears in **Eq. (2.19)**, can be transformed with respect to τ.

$$k = \frac{1}{(\nabla\tau)^2}(\phi\mu c_t)_{\text{init}} \tag{2.47}$$

In the use of **Eq. (2.46)** and **(2.47)**, Darcy's law (**Eq. (2.3)**) can be expressed in terms of τ.

$$u = -\frac{(\phi\mu c_t)_{\text{init}}}{\mu}\frac{1}{|\nabla\tau|}\frac{\partial P}{\partial\tau} \tag{2.48}$$

As previously mentioned, the corresponding drainage volume surrounded by τ–contour evolves from the sink or source of pressure disturbance, which is usually injection wells or production wells, to entire domain Ω. Now, in order to obtain the fluid flow equation based on τ–contour, consider a thin layer enclosed by two τ–contours with the surface area of $d\Omega(\tau)$ and $d\Omega(\tau+\Delta\tau)$. In this case, the volume in this domain can be approximated by the product of surface area, dA, and the layer thickness, $\Delta\tau/|\nabla\tau|$.

$$dV = \frac{\nabla\tau}{|\nabla\tau|}dA \tag{2.49}$$

Taking the volumetric integral of mass balance equation expressed in **Eq. (2.1)**, the following equation can be derived.

$$\int_{\Omega}\frac{\partial(\phi\rho)}{\partial t}dV = -\int_{\Omega}\nabla\bullet(\rho\mathbf{u})dV \tag{2.50}$$

As for the RHS, which represents the flux term, it can be expressed as surface integral in the use of divergence theorem.

$$\int_{\Omega}\nabla\bullet(\rho\mathbf{u})dV = \int_{d\Omega}(\rho\mathbf{u})\bullet\vec{\mathbf{n}}\,dA = \int_{d\Omega(\tau)}(\rho\mathbf{u})\bullet\frac{\nabla\tau}{|\nabla\tau|}\,dA \tag{2.51}$$

On the other hand, the LHS, the accumulation term, in **Eq. (2.50)** can also be expressed as surface integral below.

$$\int_{\Omega} \frac{\partial(\phi\rho)}{\partial t} dV = \nabla\tau \int_{d\Omega(\tau)} \frac{\partial(\phi\rho)}{\partial t} \frac{1}{|\nabla\tau|} dA \tag{2.52}$$

Substituting **Eq. (2.51)** and **(2.52)** into **Eq. (2.50)**, the following mass balance equation as a form of surface integral is obtained.

$$\nabla\tau \int_{d\Omega(\tau)} \frac{\partial(\phi\rho)}{\partial t} \frac{1}{|\nabla\tau|} dA = -\int_{d\Omega(\tau)} (\rho\mathbf{u}) \bullet \frac{\nabla\tau}{|\nabla\tau|}\, dA \tag{2.53}$$

In the use of the velocity expressed in terms of DTOF (**Eq. (2.47)**),

$$\int_{d\Omega(\tau)} \frac{\partial(\phi\rho)}{\partial t} \frac{1}{|\nabla\tau|} dA = \frac{1}{\nabla\tau} \left(\int_{d\Omega(\tau)} \rho \frac{(\phi\mu c_t)_{\text{init}}}{\mu} \frac{\partial P}{\partial \tau} \bullet \frac{1}{|\nabla\tau|} dA \right) \tag{2.54}$$

by using the following definition of exponential rock compressibility function M_ϕ

$$M_\phi = e^{c_r(P - P_{\text{init}})} \tag{2.55}$$

Eq. (2.54) can be transformed below,

$$\int_{d\Omega(\tau)} \frac{\partial\left(M_\phi \rho\right)}{\partial t} \frac{\phi_{\text{init}}}{|\nabla\tau|} dA = \frac{\partial}{\partial \tau} \left(\int_{d\Omega(\tau)} \rho \frac{(\mu c_t)_{\text{init}}}{\mu} \frac{\partial P}{\partial \tau} \bullet \frac{\phi_{\text{init}}}{|\nabla\tau|} dA \right) \tag{2.56}$$

where ϕ_{init} represents initial porosity. Taking the surface integral of **Eq. (2.48)**, let us define the $w(\tau)$ function below.

$$w(\tau) = \int_{d\Omega(\tau)} \frac{\phi_{\text{init}}}{|\nabla\tau|} dA = \frac{dV_p}{d\tau} \tag{2.57}$$

$w(\tau)$ is equal to the derivative of the drainage pore volume by diffusive time of flight. Multiplying $w(\tau)$ with both sides of **Eq. (2.56)**, the following equation can be obtained.

$$w(\tau) \int_{d\Omega(\tau)} \frac{\partial\left(M_\phi \rho\right)}{\partial t} dA = \frac{\partial}{\partial \tau} \left(w(\tau) \int_{d\Omega(\tau)} \rho \frac{(\mu c_t)_{\text{init}}}{\mu} \frac{\partial P}{\partial \tau} dA \right) \tag{2.58}$$

In the above equation, P represents the reservoir pressure, which is location and time dependent variable. Thus, in the FMM coordinate, it depends on τ and t. By transforming **Eq. (2.56)** further, we obtain the DTOF-based material balance equation expressed below.

$$w(\tau)\frac{\partial\left(M_\phi \rho\right)}{\partial t} = \frac{\partial}{\partial \tau}\left(w(\tau)\rho\frac{(\mu c_t)_{\text{init}}}{\mu}\frac{\partial P}{\partial \tau}\right) \tag{2.59}$$

In comparison of the equation above with the general material balance equation, the flux term in DTOF-based flow equation corresponds the following part.

$$\nabla \bullet (\rho \mathbf{u}) \equiv -\frac{\phi_{\text{init}}}{w(\tau)}\frac{\partial}{\partial \tau}\left(w(\tau)\rho\frac{(\mu c_t)_{\text{init}}}{\mu}\frac{\partial P}{\partial \tau}\right) \tag{2.60}$$

Eq. (2.56) is a 1-D fluid transport equation, which embeds the reservoir heterogeneity into the DTOF coordinates, and it can be easily solved with finite difference scheme. Notice this coordinate transformation is similar to the concept of streamline simulators, which consider reservoir pressure along CTOF coordinates. However, it is worth noting that only FMM is applicable not only for (pseudo) steady state flow but also for transient flow regime, which has significant importance in shale gas and oil production.

2.2.7 Discretization Model

In order to conduct numerical simulation based on **Eq. (2.60)**, we need to discretize the equation for space and time. In the FMM grid coordinates, two boundary conditions are imposed at the first and the last grids, which correspond to inner and outer boundaries, respectively. The inner boundary represents the wellbore properties of the production well or the injection well, such as bottom hole pressure or oil rate, and the outer boundary is imposed as no flow boundary in many cases. Adding the sink/source term to **Eq. (2.60)**, we can derive the following equation.

$$\frac{\partial(\phi\rho)}{\partial t} = \frac{\phi_{\text{init}}}{w(\tau)}\frac{\partial}{\partial\tau}\left(w(\tau)\rho\frac{(\mu c_t)_{\text{init}}}{\mu}\frac{\partial P}{\partial\tau}\right) + \rho q \tag{2.61}$$

where q is the fluid production/injection rate per unit volume at wellbore condition. In this equation, LHS denotes the accumulation term, ρq corresponds to sink/source term and the rest of RHS expresses the flux term, respectively. As mentioned above, sink/source term, ρq, is imposed only in the first grid. Dividing both sides of **Eq. (2.61)** by fluid density at the surface condition, ρ_{sc}, and initial porosity, ϕ_{init}, the following form of the equation can be obtained,

$$\frac{\partial}{\partial t}\left(\frac{M_\phi}{B}\right) = \frac{1}{w(\tau)}\frac{\partial}{\partial\tau}\left(w(\tau)\frac{(\mu c_t)_{\text{init}}}{B\mu}\frac{\partial P}{\partial\tau}\right) + \frac{1}{\phi_{\text{init}}}\frac{q}{B} \tag{2.62}$$

where B is the formation volume factor (= FVF). We consider discretizing **Eq. (2.61)** in terms of grid block i. In the use of grid dependent parameter, C, the following transformation can be conducted.

$$\begin{aligned}\frac{\partial}{\partial\tau}\left(C\frac{\partial P}{\partial\tau}\right)\Big|_i &= \frac{1}{\tau_{i+1/2}-\tau_{i-1/2}}\left(C_{i+1/2}\frac{\partial P}{\partial\tau}\Big|_{i+1/2} - C_{i-\frac{1}{2}}\frac{\partial P}{\partial\tau}\Big|_{1-1/2}\right)\\ &= \frac{1}{\Delta\tau_i}\left[C_{i+1/2}\left(\frac{P_{i+1}-P_i}{\tau_{i+1}-\tau_i}\right) - C_{i-1/2}\left(\frac{P_i-P_{i-1}}{\tau_i-\tau_{i-1}}\right)\right]\\ &= \frac{1}{\Delta\tau_i}\left[\frac{C_{i+1/2}}{\Delta\tau_{i+1/2}}(P_{i+1}-P_i) - \frac{C_{i-1/2}}{\Delta\tau_{i-1/2}}(P_i-P_{i-1})\right]\end{aligned} \tag{2.63}$$

In the FMM grid coordinate, $\Delta\tau_i$ and $\Delta\tau_{i\pm1/2}$ represent full grid length and half grid length of grid i, respectively. With the transformation expressed above, the flux term in **Eq. (2.62)** can be converted below.

$$\begin{aligned}&\frac{\partial}{\partial\tau}\left(w(\tau)\frac{(\mu c_t)_{\text{init}}}{B\mu}\frac{\partial P}{\partial\tau}\right)\\ &\qquad= \frac{T_{i-1/2}P_{i-1/2} - \left(T_{i-1/2}-T_{i+1/2}\right)P_i + T_{i+1/2}P_{i+1}}{\Delta\tau_i}\end{aligned} \tag{2.64}$$

We define $T_{i\pm1/2}$ as the transmissibility between grid i and grid $i \pm 1$, which can be expressed in the following form.

$$T_{i\pm1/2} = \frac{w_{i\pm1/2}}{\Delta\tau_{i\pm1/2}} (\mu c_t)_{\text{init},i\pm1/2} \left(\frac{1}{B\mu}\right)_{up} \tag{2.65}$$

As for the partial derivatives, $w(\tau)$, there are several ways to calculate it: backward difference, forward difference, central difference and numerical derivative methods.

$$w_i = \left(\frac{dV_p}{d\tau}\right)_i = \frac{V_{p,i+1/2} - V_{p,i-1/2}}{\tau_{i+1/2} - \tau_{i-1/2}} \tag{2.66}$$

$$w_{i-1/2} = \left(\frac{dV_p}{d\tau}\right)_{i-1/2} = \frac{V_{p,i} - V_{p,i-1}}{\tau_i - \tau_{i-1}} \tag{2.67}$$

$$w_{i+1/2} = \left(\frac{dV_p}{d\tau}\right)_{i+1/2} = \frac{V_{p,i+1} - V_{p,i}}{\tau_{i+1} - \tau_i} \tag{2.68}$$

$$w_i = \left(\frac{dV_p}{d\tau}\right)_i = \frac{1}{\tau_i}\left[\frac{\ln(\tau_i/\tau_{i-k})V_{p,i+j}}{\ln(\tau_{i+j}/\tau_i)\ln(\tau_{i+j}/\tau_{i-k})} + \frac{\ln(\tau_{i+j}\tau_{i-k}/\tau_i^2)V_{p,i}}{\ln(\tau_{i+j}/\tau_i)\ln(\tau_i/\tau_{i-k})} - \frac{\ln(\tau_{i+j}/\tau_i)V_{p,i-k}}{\ln(\tau_i/\tau_{i-k})\ln(\tau_{i+j}/\tau_{i-k})}\right] \tag{2.69}$$

Eq. (2.66), **(2.67)**, **(2.68)** and **(2.69)** correspond to central difference, backward difference, forward difference and numerical derivative, respectively. At first, we used to use central difference method to calculate $w(\tau)$, but later on, Atsushi el at (2016) realized numerical derivative based $w(\tau)$ is better in terms of accuracy. Thus, in this research, **Eq. (2.69)** is employed for the $w(\tau)$ calculation.

In the use of transmissibility expressed in **Eq. (2.65)**, **Eq. (2.62)** can be written below.

$$T_{i-1/2}^{n+1}P_{i-1}^{n+1} - \left(T_{i-1/2}^{n+1} + T_{i+1/2}^{n+1}\right)P_i^{n+1} + T_{i+1/2}^{n+1}P_{i+1}^{n+1} = \frac{w_i\Delta\tau_i}{\Delta t^{n+1}}\left[\left(\frac{M_{\phi,i}^{n+1}}{B_i^{n+1}}\right) - \left(\frac{M_{\phi,i}^{n}}{B_i^{n}}\right)\right] - \frac{w_i\Delta\tau_i}{\phi_{\text{init},i}}\frac{q^{n+1}}{B_i^{n+1}} \tag{2.70}$$

As for the exponential rock compressibility, M_ϕ, take a look at **Eq. (2.65)** and the upper suffix, n+1, denotes time step level.

Next, as for the sink/source term, it corresponds to the following part of **Eq. (2.70)** at the surface condition,

$$q_s^{n+1} = \frac{w_1 \Delta\tau_1}{\phi_{\text{init}}} \frac{q^{n+1}}{B_1^{n+1}} \tag{2.71}$$

where the lower suffix s represents the surface condition and 1 denotes the first grid of the FMM coordinates. Substituting **Eq. (2.47)** into the flow rate q^{n+1}, the following equation is obtained.

$$q_s^{n+1} = \frac{w_1 \Delta\tau_1}{\phi_{\text{init}}} \left[\frac{1}{\Delta\tau_1} (\phi\mu c_t)_{\text{init},1} \left(\frac{1}{B\mu} \right)_1^{n+1} \left(\frac{P_1^{n+1} - P_{wf}^{n+1}}{\tau_1 - \tau_{\text{well}}} \right) \right] \tag{2.72}$$

$$q_s^{n+1} = w_1 (\mu c_t)_{\text{init},1} \left(\frac{1}{B\mu} \right)_1^{n+1} \left(\frac{P_1^{n+1} - P_{wf}^{n+1}}{\tau_1 - \tau_{\text{well}}} \right) \tag{2.73}$$

In this way, the governing equation for single phase flow is derived. **Eq. (2.70)** represents the governing equation and the inner boundary condition at production / injection wells given by **Eq. (2.73)**. Thus, you have only to solve the non-linear equations with respect to reservoir pressure.

2.3 Results and Discussion

In this section, the corresponding results based on the algorithm described above are shown in comparison with the multi-stencil FMM and the original (5-stencil for 2-D or 7-stencil for 3-D) FMM. Since the objective of this study is to investigate the strength of the multi-stencil FMM, the input is selected so that other complicating factors, which are not related to this can be ignored such as Dual Porosity models (DPSP), boundary reflection effect and multi-phase flow, etc. First, the synthetic reservoir models used are briefly described, and the corresponding results follow next. In order to show the wide

applicability of the multi-stencil FMM, this is employed both to the homogenous models and to the heterogeneous models for 2-D and 3-D cases.

2.3.1 2-D Reservoir Model

In this section, the results in the case of 2-D reservoirs are shown both for homogeneous and heterogeneous cases. Before jumping into the results, the input data is briefly described first. The properties of the reservoir model used are described below. The fluid in the reservoir exists in single phase (oil), and oil is produced in bottom hole pressure constraint. The production well is set in the middle of the reservoir.

Table. 2.1 – Reservoir Properties for 2-D Model

Region	Name	Value
Reservoir	Grid Number	41 x 41 x 1
	Grid Size	100 x 100 x 10 cu-ft
Well	Location	(21,21,1)
	Control	BHP=5000 psia
Rock	Avg Permeability	1 mD
	Porosity	0.01
	Compressibility	1E-6 /psi @ 6000 psia
Fluid (Oil)	Density (@SC)	63.02 lb/ft^3
Initial Condition	Pressure	8000 psia

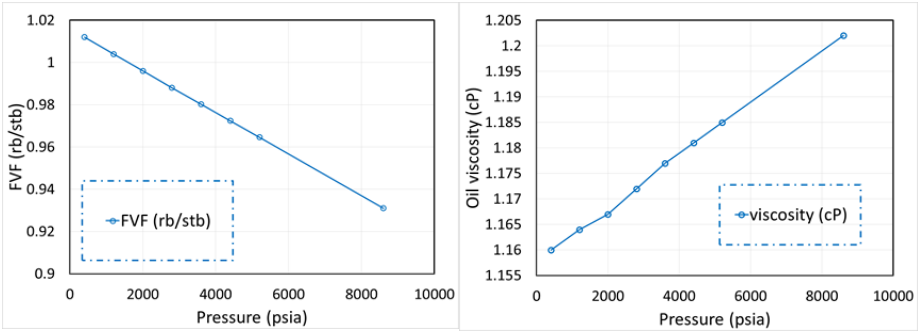

Fig. 2.5 – Pressure Dependent Fluid Properties (Oil Formation Volume Factor, Left and Oil Viscosity, Right)

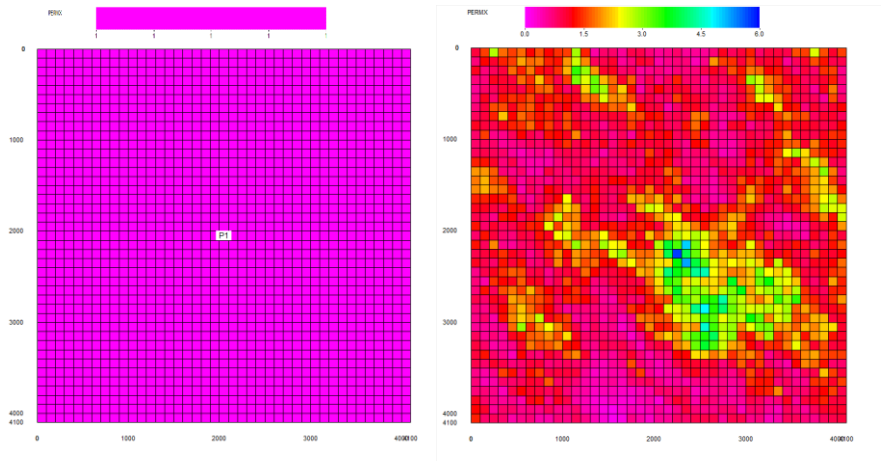

Fig. 2.6 – 2-D Reservoir Model (Homogenous, Left and Heterogeneous, Right)

Based on the reservoir property shown above, FMM simulation is done in comparison with the output of commercial software. First of all, the relationship between drainage pore volume calculated from FMM and DTOF is shown in comparison with that of analytical solution. The gradient of the slope corresponds to $w - tau$, which is closely related to the fluid transmissibility. The analytical solution is in use of the analogy of wave propagation. In the 2-D homogeneous media, the wave propagates circularly at the same speed shown below. In the following equation, V_p denotes the drainage pore volume, h denotes the grid height and v is the fluid velocity. Here, for the purpose of the comparison with analytical solution, constant values are used for pressure dependent properties: 1.0 (rb/stb) for oil formation volume factor, 1.0 (cP) for oil viscosity and 1.0 (/psia) for rock compressibility, respectively.

$$V_p = \pi \phi h v^2 \tag{2.74}$$

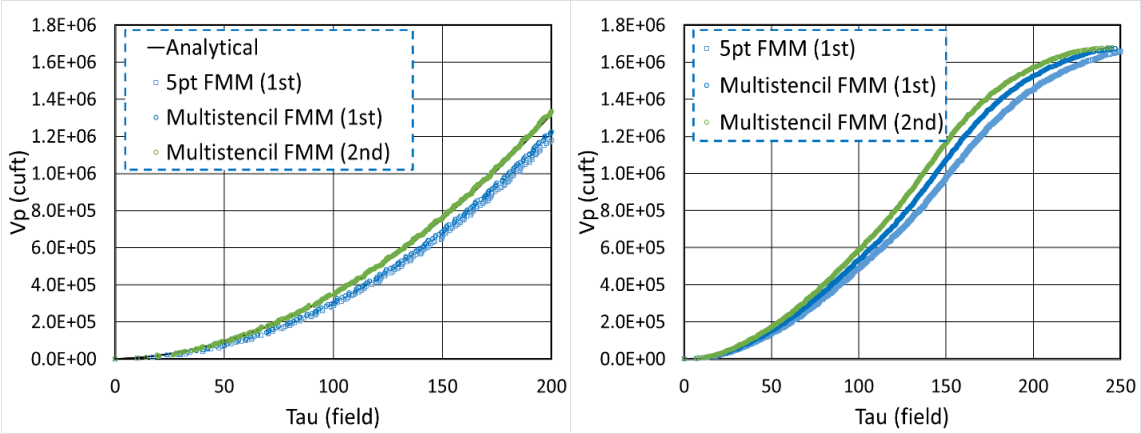

Fig. 2.7 – Drainage Pore Volume V.S. Tau for 2-D (Homogenous, Left and Heterogeneous, Right)

From the result above, you can confirm that the error calculated from the original 5-stencil FMM is the biggest, and it improves in the use of the first order multi-stencil FMM. It is worth noting that the error originating from the second order multi-stencil FMM is the smallest among them.

Lastly, the oil production rate calculated from the multi-stencil FMM based on the input data shown in the above table is presented in comparison with that of commercial software. As expected from Fig.2.8, one can see that, in both homogeneous and heterogeneous cases, the result is most accurate in the use of the second order multi-stencil FMM and the first order multi-stencil FMM follows next. The original first order 5-stencil FMM generates the least accurate result.

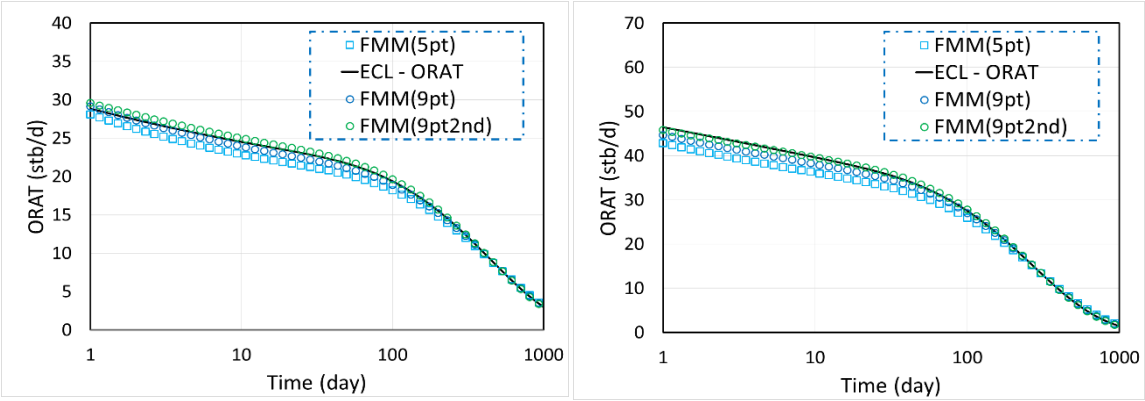

Fig. 2.8 – Oil Production Rate for 2-D (Homogenous, Left and Heterogeneous, Right)

2.3.2 3-D Reservoir Model

In this section, the results in the case of the 3-D reservoirs are shown both for homogeneous and heterogeneous cases. Before jumping into the results, the input data is briefly described first. The properties of the reservoir model used are described below. The fluid in the reservoir exists in single phase (oil), and oil is produced in bottom-hole pressure constraint. The production well is set in the middle of the reservoir and only the bottom layer is completed. Since FMM cannot take into consideration the gravity effect up until now, the corresponding results are to be compared with the results of the commercial software without gravity.

Table. 2.2 – Reservoir Properties for 3-D Model

Region	Name	Value
Reservoir	Grid Number	41 x 41 x 5
	Grid Size	100 x 100 x 100 cu-ft
Well	Location	(21,21,5)
	Control	BHP=3000 psia
Rock	Avg Permeability	1 mD
	Porosity	0.01
	Compressibility	1E-6 /psi @ 6000 psia
Fluid (Oil)	Density (@SC)	63.02 lb/ft^3
Initial Condition	Pressure	5000 psia

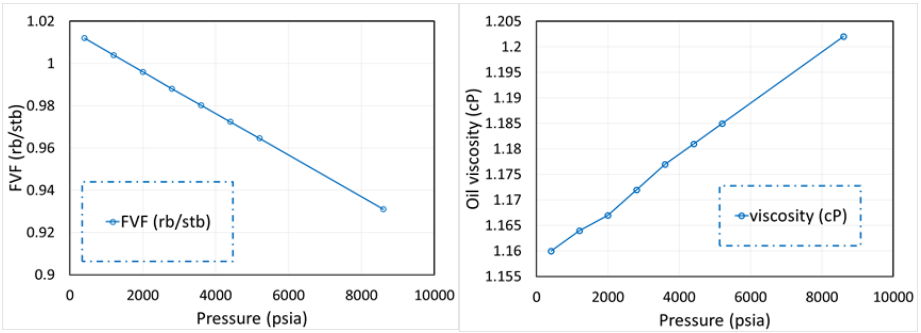

Fig. 2.9 – Pressure Dependent Fluid Properties (Oil Formation Volume Factor, Left and Oil Viscosity, Right)

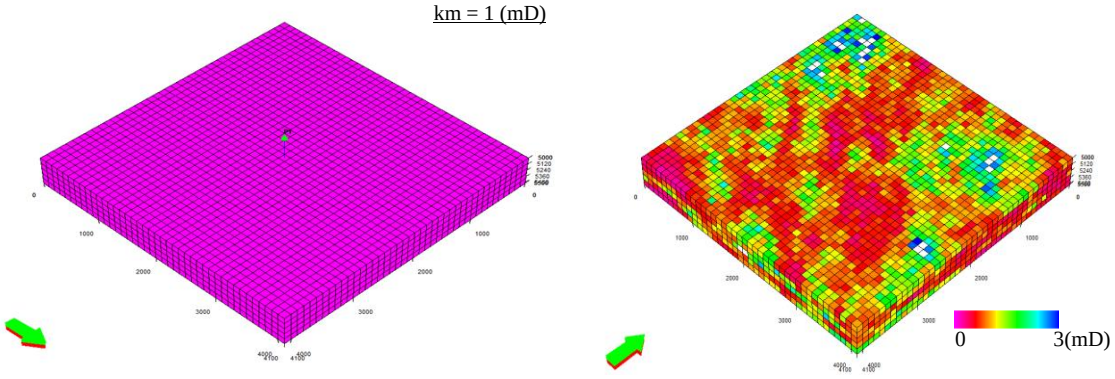

Fig. 2.10 – 3-D Reservoir Model (Homogenous, Left and Heterogeneous, Right)

Based on the reservoir property shown above, FMM simulator is run in comparison with the output of commercial software. First of all, the relationship between drainage pore volume calculated from FMM and DTOF is shown in comparison with that of analytical solution. The gradient of the slope corresponds to $w - tau$, which is closely related to the fluid transmissibility. The analytical solution uses the analogy of wave propagation. In the 2-D homogeneous media, the wave propagates circularly at the same speed. As for 3-D, it can be expressed in the analogy of a sphere shown below. In the following equation, V_p denotes the drainage pore volume, h denotes the grid height, nz represents the number of layers along the z direction and v is the fluid velocity. Here, for the purpose of the comparison with analytical solution, constant values are used for pressure dependent properties: 1.0 (rb/stb) for oil formation volume factor, 1.0 (cP) for oil viscosity and 1.0 (/psia) for rock compressibility, respectively.

$$V_p = \frac{4}{3}\pi\phi v^3 \tag{2.74}$$

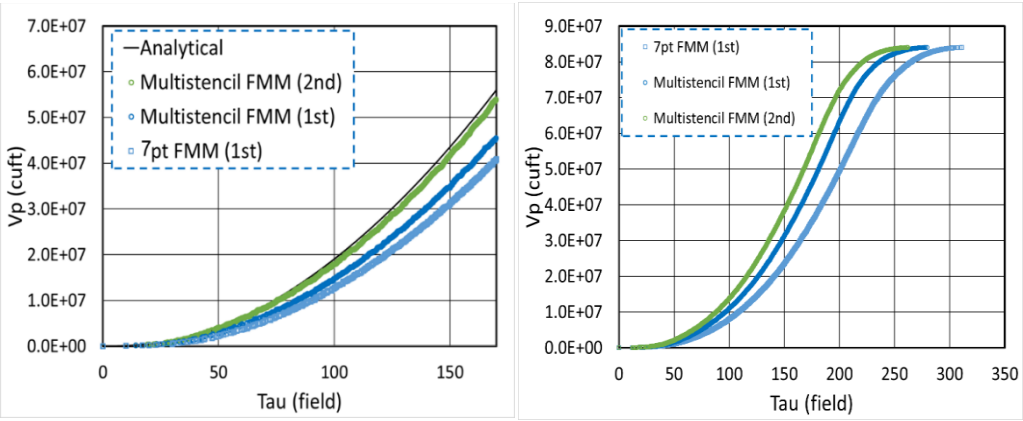

Fig. 2.11 – Drainage Pore Volume V.S. Tau for 3-D (Homogenous, Left and Heterogeneous, Right)

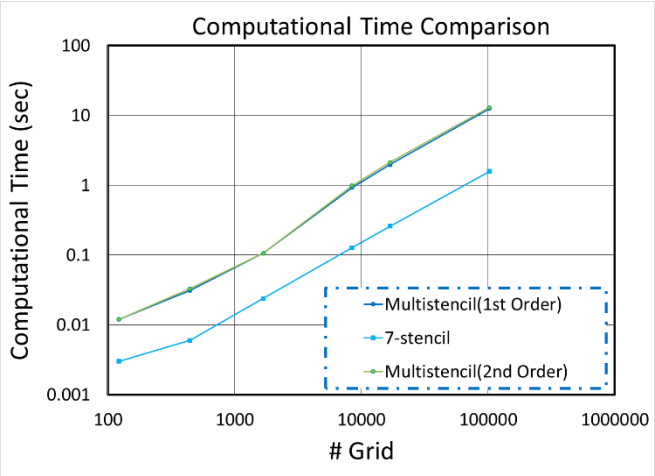

Fig. 2.12 – Computational Time for DTOF Calculation

From the result above, one can confirm that the error calculated from the original 7-stencil FMM is the largest and the error improves in accuracy using the first order multi-stencil FMM. It is worth noting that the error originating from the second order multi-stencil FMM is the smallest among the errors. Next, from the figure shown in the above-right, one can see that how much the computational time increases when using multi-stencil FMM. Although it is true that multi-stencil FMM requires longer elapsed time for DTOF calculation, this part accounts for only a small part of the whole simulation time because the time needed for pressure calculation is dominant in the whole run.

Lastly, the oil production rate calculated from multi-stencil FMM based on the input data shown in Table 2.2 is presented in comparison with the oil production rate calculated from the commercial software. As expected from Fig.2.12, you can see that, in both homogeneous and heterogeneous cases, the results are most accurate when using the second order multi-stencil FMM, and the first order multi-stencil FMM is the second most

accurate. The original first order 7-stencil FMM generates the least accurate result. In case of the heterogeneous case, you can also find that there might be a slight gap between the oil production rate calculated from FMM and that of the commercial software. This is because, in the heterogeneous reservoir, the FMM simulator is still subject to causality issues. In this reservoir model used, the completion is supposed only in the bottom layer, which is quite close to the reservoir boundary. In order to take into consideration the boundary effect properly, it is necessary to use the boundary reflection effect for DTOF calculation. As for the boundary reflection effect for DTOF calculation, please refer to the SPE paper by Zhengzheng and King et al in 2017.

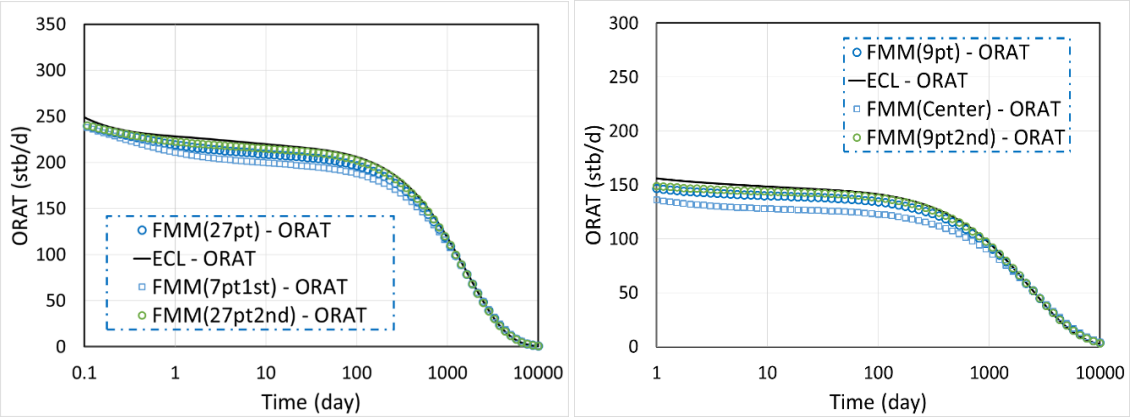

Fig. 2.13 – Oil Production Rate for 3-D (Homogenous, Left and Heterogeneous, Right)

2.4 Conclusion

In this chapter, the strength of multi-stencil FMM is proved. Although it needs longer computational time for DTOF calculation, this part is not significant since the pressure calculation is the most dominant throughout the whole reservoir simulation process. By

using multi-stencil FMM, one can improve the accuracy of DTOF, which leads to better oil production in terms of the accuracy. The higher order FMM can make a great contribution to the accuracy of DTOF calculation as well. This does not require additional computational time. These methods are shown to be applicable for 2-D and 3-D reservoirs in the case of homogeneous and heterogeneous models.

CHAPTER III

APPLICATION OF FMM INTO HETEROGENEOUS DUAL POROSITY MEDIA

3.1 Introduction to Dual Porosity Model

Since Shale reservoirs are usually developed using hydraulic fracturing techniques, shale reservoir models are characterized by two distinct regions: matrix and fracture. In more detail, fractures are composed of two types: hydraulic fractures and natural fractures. In both of the cases, the fluid flux between the fracture and the matrix plays an important role in terms of the recovery. In this system, the fracture network is highly conductive with high permeability, but it has quite small storage because of its small porosity. On the other hand, matrices work as a big storage of fluid, but its conductivity is quite low due to its extremely small permeability. To put it in short, fractures work as conduits of fluids and matrices store fluids. The models considering the dual system can be categorized into the following three types: SPSP (Single Porosity Single Permeability Model), DPSP (Dual Porosity Single Permeability Model) and DPDP (Dual Porosity Dual Permeability Model). Each model is illustrated below.

Fig. 3.1 – The Concept of SPSP Model.

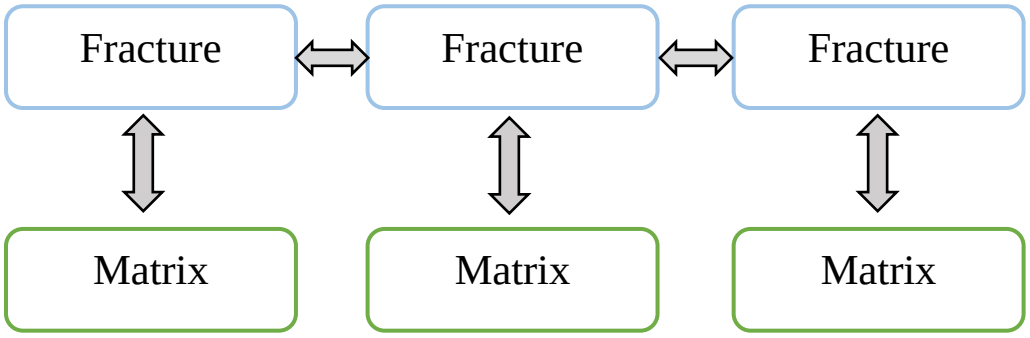

Fig. 3.2 – The Concept of DPSP Model.

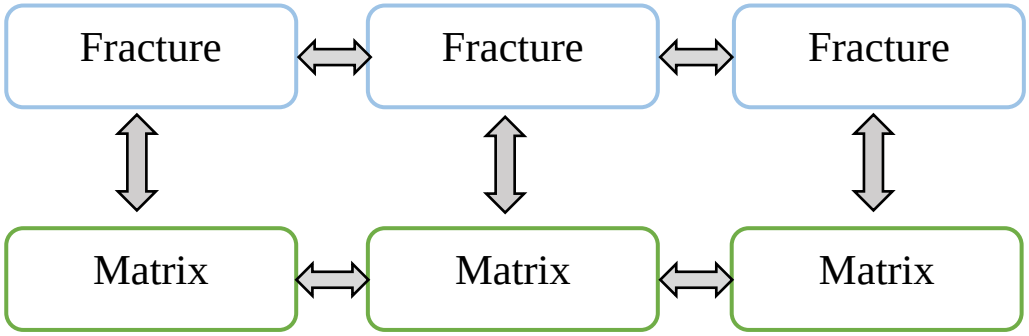

Fig. 3.3 – The Concept of DPDP Model.

As described above, SPSP models assume that there is a fluid flow only between fractures. The second model, DPSP, considers the interaction between fractures and matrices in addition to the flow between fractures. The last case, DPDP, admits the flow between matrices on top of the flow explained above. Generally speaking, SPSP is the most computationally inexpensive but lacks of accuracy because it does not consider the role of matrices, which is one of the unique characteristics of shale reservoirs. On the other hand, DPDP is regarded to be the most accurate but computationally expensive. However, according to the SPE paper about the field application of FMM into the East Texas shale

field (Atsushi Iino et al (2017)), we can realize almost the same accuracy between DPSP and DPDP in the case of FMM, and the former requires less elapsed time. Because of this reason, DPSP is employed to investigate the heterogeneity of matrices in this research. As explained in the previous chapter, the fluid flow equation for SPSP models is expressed in the following form.

$$T_{i-1/2}^{n+1}P_{i-1}^{n+1} - \left(T_{i-1/2}^{n+1} + T_{i+1/2}^{n+1}\right)P_i^{n+1} + T_{i+1/2}^{n+1}P_{i+1}^{n+1} = \frac{w_i\Delta\tau_i}{\Delta t^{n+1}}\left[\left(\frac{M_{\phi,i}^{n+1}}{B_i^{n+1}}\right) - \left(\frac{M_{\phi,i}^{n}}{B_i^{n}}\right)\right] - \frac{w_i\Delta\tau_i}{\phi_{\mathrm{init},i}}\frac{q^{n+1}}{B_i^{n+1}} \quad (2.49)$$

In the case of DPSP, it is necessary to take into account the flux term between matrices and fractures. Thus, the governing equation for fractures is expressed below,

$$T_{i-1/2}^{n+1}P_{f,i-1}^{n+1} - \left(T_{i-1/2}^{n+1} + T_{i+1/2}^{n+1}\right)P_{f,i}^{n+1} + T_{i+1/2}^{n+1}P_{f,i+1}^{n+1} = \frac{w_i\Delta\tau_i}{\Delta t^{n+1}}\left[\left(\frac{M_{\phi,i}^{n+1}}{B_i^{n+1}}\right) - \left(\frac{M_{\phi,i}^{n}}{B_i^{n}}\right)\right] + v_i\Delta\tau_i T_{FM,i}^{n+1}\left(P_{f,i}^{n+1} - P_{m,i}^{n+1}\right) - q_{sf}^{n+1} \quad (3.1)$$

where

$$T_{FM,i}^{n+1} = \sigma k_m\left(\frac{1}{B\mu}\right)_{up} \quad (3.2)$$

This term corresponds to the transmissibility of flux between matrices and fractures. In the above equation, the lower suffix "*up*" represents that this property is governed by upwinding scheme. Likewise, since there is no interaction between matrices in the case of DPSP, the fluid flow equation for matrices is expressed below.

$$\frac{1}{\Delta t^{n+1}}\left[\left(\frac{\phi_{m,i}^{n+1}}{B_i^{n+1}}\right) - \left(\frac{\phi_{m,i}^{n}}{B_i^{n}}\right)\right] - T_{FM,i}^{n+1}\left(P_{f,i}^{n+1} - P_{m,i}^{n+1}\right) = 0 \quad (3.3)$$

In the case of the FMM-based DPSP model, the Cartesian grid coordinate is transformed into DTOF grid coordinate based on fracture properties and the matrix grid is assumed to belong to its fracture grid. Thus, in order to apply FMM into DPSP models, first the coordinate-transformation from Cartesian grid to DTOF grid was conducted, and then the transmissibility between matrices and fractures was averaged so that the mass of flow should become the same as that of the Cartesian grid.

3.2 Parameters to Be Averaged

In the previous section, the necessity of averaging for transmissibility between fractures and matrices is explained. Since the transfer term is composed of the matrix grid properties, such as shape factor and absolute permeability, these matrix dependent properties should be averaged in an appropriate manner. Besides, it is also important to select the best representative value for matrix porosity because it is included in matrix accumulation term in **Eq. (3.2)**. As for the porosity, the average of it must be taken so that the total mass balance is preserved. Thus, the volumetric average is taken for matrix porosity. Therefore, we consider the appropriate averaging methods for shape factor, matrix permeability in the case of single phase flow.

Table. 3.1 – Parameters to be averaged

Parameter	Method	Comment
k_m	Needed to be studied	-
σ_v	Needed to be studied	-
ϕ_m	Volumetric	To preserve MBE

3.3 General Averaging Methods

In this section, the general averaging methods are introduced first. After that, the applicable approach for FMM among them is selected. The following approaches listed below are commonly used for averaging grid properties.

3.3.1 1-D Arithmetic Average

This method outputs the simple arithmetic average of all the permeability within the target area. The following figure describes the concept of arithmetic average method. It can be compared as if all of the reservoirs are re-stacked and placed immediately adjacent to a well. This is exact for uniform layers arranged in parallel. In the actual heterogeneous reservoirs, this tends to calculate the average permeability quite optimistically in comparison to the actual value.

$$\bar{k} = \frac{\sum_{i=1}^{N} k_i h_i}{\sum_{i=1}^{N} h_i} \tag{3.4}$$

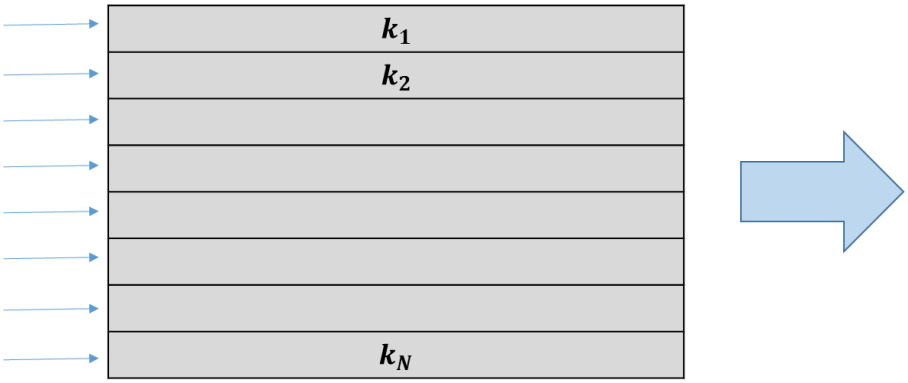

Fig. 3.4 – 1-D Arithmetic Average (Adapted from Cardwell and Parsons et al (1945))

3.3.2 1-D Harmonic Average

This methods outputs the simple harmonic average of all the permeability within the target area. The following figure describes the concept of harmonic average method. It can be compared as if all of the reservoirs are sliced and stacked into one amazingly long core. Based on the assumption, all the flow must run through each piece of rock. Although it gives a good estimate for vertical permeability, in the actual heterogeneous reservoirs, this tends to calculate the average permeability more pessimistically than actual value.

$$\bar{k} = \frac{\sum_{i=1}^{N} h_i}{\sum_{i=1}^{N} \frac{h_i}{k_i}} \tag{3.5}$$

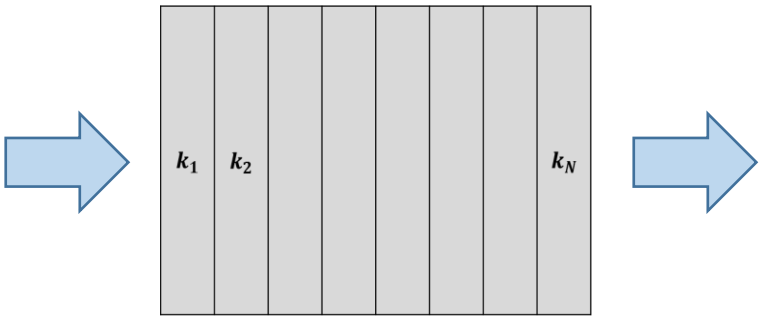

Fig. 3.5 – 1-D Harmonic Average (Adapted from Cardwell and Parsons et al (1945))

3.3.3 1-D Geometric Average

This methods outputs the simple logarithmic average of all the permeability within the target area. The following figure describes the concept of this method. The calculated average is exact for randomly distributed (uncorrelated) permeabilities in 2D with small variance. Generally, this tends to calculate the average permeability which is almost intermediate between the arithmetic average and the harmonic average.

$$\bar{k} = \frac{1}{N}\sum_{i=1}^{N} \log(k_i) \tag{3.6}$$

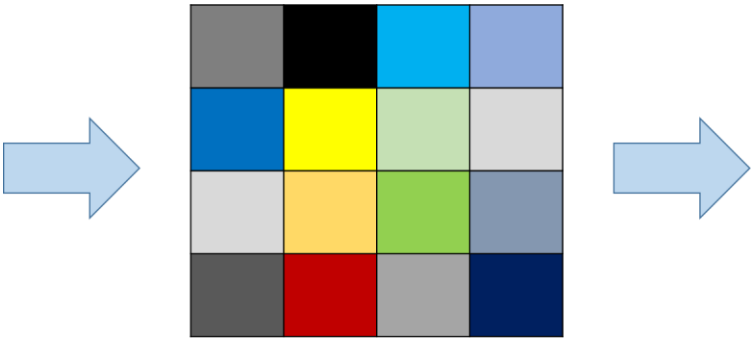

Fig. 3.6 – 1-D Geometric Average (Adapted from Cardwell and Parsons et al (1945))

3.3.4 Harmonic-Arithmetic Average

This methods outputs the simple arithmetic average of all the harmonic means of permeabilities within each layer, turning off all the cross flow between the layers. The following figure describes the concept of this method (Cardwell & Parsons et al (1945)). This method provides the rigorous lower-bound estimate of the permeability.

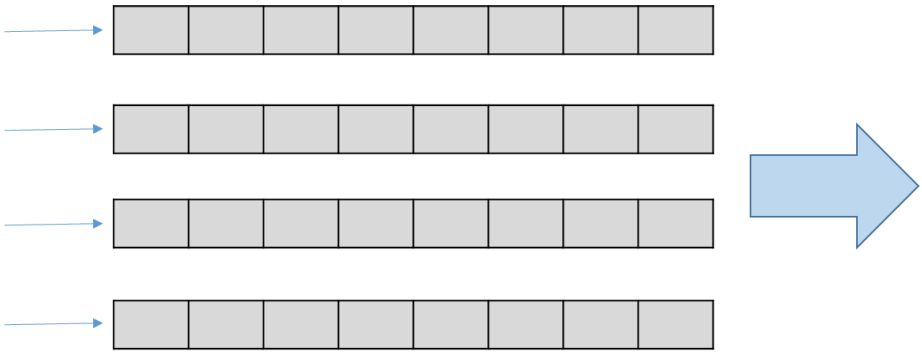

Fig. 3.7 – Harmonic-Arithmetic Average (Adapted from Cardwell and Parsons et al (1945))

3.3.5 Arithmetic-Harmonic Average

This methods generates the average based on each column of the model and on each row of the model. The following figure describes the concept of this method (Cardwell & Parsons et al (1945)). This model is based on the assumption that pressure is in equilibrium for transverse direction. It provides the rigorous upper-bound estimate of the permeability.

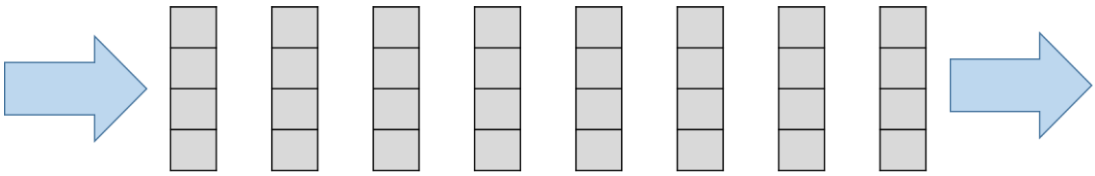

Fig. 3.8 – Arithmetic-Harmonic Average (Adapted from Cardwell and Parsons et al (1945))

3.3.6 Incomplete Layer Method

This methods generates the geometric average of the rigorous analytical upper and lower bound. Usually, Arithmetic-Harmonic average is used for the upper bound and Harmonic-Arithmetic average is used for the lower bound. The following figure describes the concept of this method (Kelkar & Perez et al (2002)). It provides the permeability with no more than 5% error from the true effective permeability when the upper and lower limits do not differ by more than 20% (Kasap, Larry W. Lake et al (1990)).

$$\bar{k} = \sqrt{k_{upper} k_{lower}} \tag{3.7}$$

3.3.7 Effective Medium Theory (EMT)

This method is based on the assumption that an appropriately averaged reservoir model should have the same response at the boundary conditions imposed as the original fine scale model. In order to understand the averaging process, let us consider the following cases: F1 and F2. In F1, the region to be uspcaled is Ω. In case of F1, the domain Ω has a fine-scale permeability and the other yellow parts are supposed to be homogeneous. In case of F2, it has only homogeneous permeability. The value of permeability in both of the yellow domains is the same and it is to be found through the averaging process. We need to keep updating k_Ω until both of the cases come to show the same response at the boundary. When the amount of flow rate becomes the same at the boundary for the same pressure difference, the permeability is determined as a representative permeability of the domain Ω. This method is usually employed for directional permeabilities in the orthogonal directions.

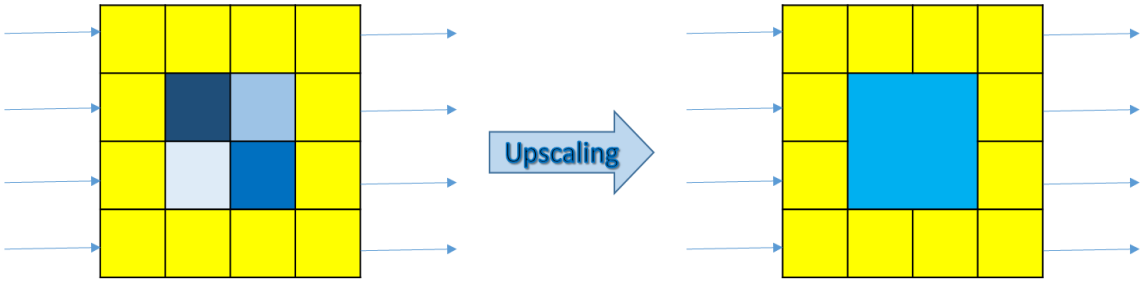

Fig. 3.9 – EMT (Adapted from G.K. Brouwer and P.A. Fokker, TNO et al (2013))

3.3.8 Renormalization Method

This method makes use of the analogy of electric network to porous media (King 1989). The concept is illustrated in the following figure. In this figure, we define the resistance

in terms of permeability. By supposing half a gridblock with a resistivity of $\frac{1}{2k_i}$, the four gridblocks are transformed into an equivalent circuit analog. In use of this analog, we can obtain the corresponding representative permeability along the flow direction. In this 2-by-2 grid case, the calculated representative permeability is expressed in the following equation,

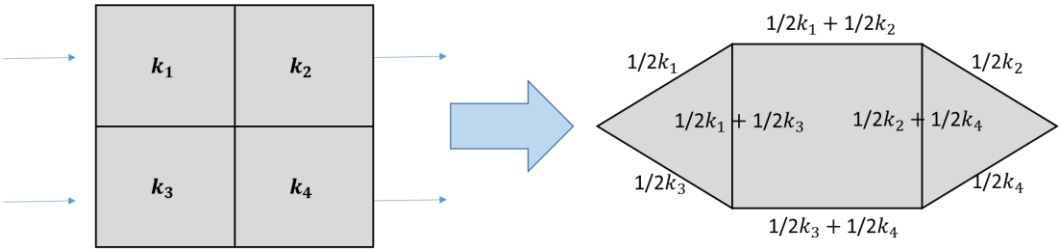

Fig. 3.10 – The Concept of Renormalization (Kelkar and Perez (2002))

$$\bar{k} = \frac{4(k_1 + k_3)(k_2 + k_4)C_1}{(k_1 + k_2 + k_3 + k_4)C_1 + 3C_2} \tag{3.8}$$

where

$$C_1 = k_2k_4(k_1 + k_3) + k_1k_3(k_2 + k_4) \tag{3.9}$$

$$C_2 = (k_1 + k_2)(k_3 + k_4)(k_1 + k_3)(k_2 + k_4) \tag{3.10}$$

3.3.9 Percolation Theory

This method considers all permeability below a threshold to be non-flowing and keeps decreasing the threshold gradually until the percolation threshold is reached. This works best for large models with many flow paths (Ambegaokar, Halperin et al (1971)).

3.3.10 Flow Based Upscaling

This method assumes all the target cells have the same pressure decline rate and generates the representative permeability so that the amount of fluid flow is the same between the fine model and the coarse model when all the grids have the same amount of pressure drop. Farmer (2002) categorized the flow based upscaling into the four different types based on whether or not a single fine grid experiment covers a substantial domain of the whole model: Local-Local, Local-Global, Global-Local and Global-Global. However, it deviates from the objective of this research to go into these approaches, so please refer to the paper (Chaitanya, K, 2014) for further explanation.

This method is useful only when the reservoir is in pseudo steady or steady state flow where all the cells have the same pressure drop rate.

3.4 Evaluation of Applicable Averaging Methods into FMM Based DPSP Models

In this section, ten general averaging methods are listed. Among them, the applicable approaches are to be selected into FMM DPSP model. First of all, the analytical methods (Arithmetic, Harmonic and Geometric) are worth trying because they are inexpensive in terms of computational time and they do not degrade the strength of FMM, to be fast. Next, Arithmetic-Harmonic and Harmonic-Arithmetic approach are not applicable for averaging of matrix properties in DPSP model. This is because this considers the fluid flow between cells to cells, but there is supposed to be no flow between matrix to matrix in DPSP model. As for Incomplete Layer Method, the concept of taking the geometric average of the upper

bound and the lower bound may be applicable, but these bounds cannot be given by Arithmetic-Harmonic and Harmonic-Arithmetic averages. Thus, in this research, arithmetic average is employed as an upper bound and harmonic average is used as lower bound. As per the same reasoning, the rest of the methods (Percolation Theory, Effective Medium Theory and Renormalization Method) cannot be applied into the averaging of matrix properties in DPSP model. Lastly, regarding the flow based methods, they average the representative transmissibility so that the total flow rate becomes the same as that of the original case. However, in the case of DPSP model, the corresponding transmissibility will be the same as that of arithmetic average. Thus, the flow based methods do not need to be tested in this research.

Therefore, the four methods applied into FMM based DPSP model are arithmetic, harmonic, geometric and Incomplete Layer method. Generally, arithmetic tends to generate the most optimistic value, while harmonic tends to provide the most pessimistic value. Geometric is intermediate of these two. Since it usually works better for randomly distributed reservoir models, it is expected to generate more effective results than arithmetic and harmonic methods do. However, as for the Incomplete Layer Method, the range of the variable is restricted more narrowly due to the upper bound (arithmetic average) and the lower bound (harmonic average). It might provide more accurate representative property than geometric based average.

3.5 Approach

In the previous section, the possible averaging approaches in FMM based DPSP models were selected. All the approaches are summarized in the table below. In this section, the more detailed process is explained for all the methods.

Table. 3.2 – Averaging Approach for 2-Phase

Parameter	Method	Comment
k_m	Arithmetic Harmonic Geometric Incomplete Layer	-
σ_v	Arithmetic Harmonic Geometric Incomplete Layer	-
ϕ_m	Volumetric	To preserve MBE

As explained in the Chapter II, FMM grid coordinate is generated by DTOF, which represents the travel time of peak pressure disturbance. However, in many cases, the pressure front may transverse the Cartesian grids as illustrated below. In this kind of situation, it is controversial to decide how to average the parameter within the FMM grid between the two pressure front curves. One possible approach is that when the pressure front has passed through the center of the grid A, you may assume the grid A is included in the FMM grid. Based on the FMM grid coordinate, you may conduct the averaging for

matrix parameters. Although this approach is easy to conduct, it lacks accuracy in that it cannot take into account the properties in partially included grids, such as grid A.

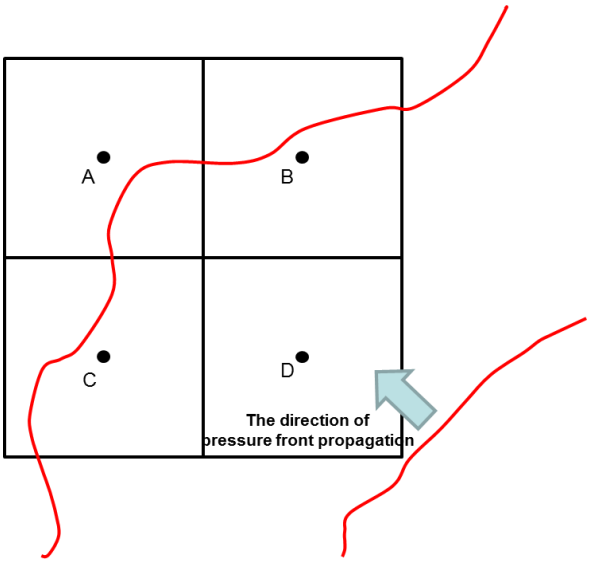

Fig. 3.11 – The Cartesian Grid Partially Included in FMM Grid

The other approach is to take a summation of pore volume weighted average and use a linear interpolation for each DTOF. Take a look at the case of arithmetic average, for instance. The following figure represents how to calculate the bulk volume at FMM grid, i, and its corresponding effective permeability for the matrix.

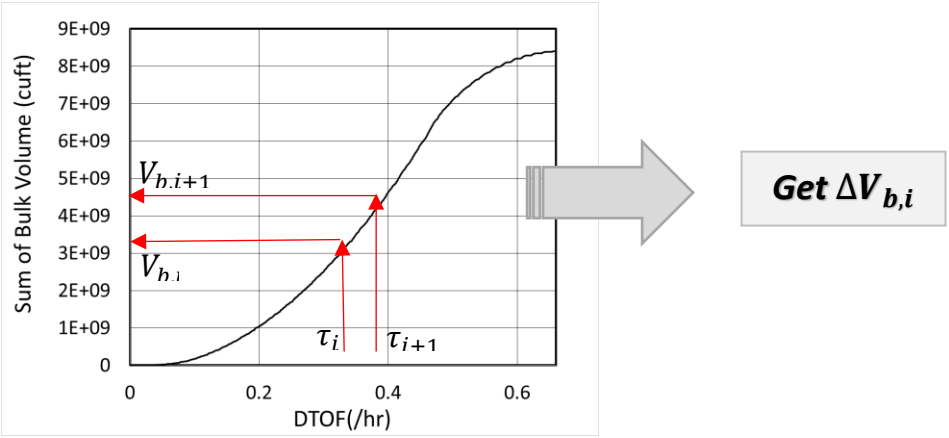

Fig. 3.12 –The Calculation of Bulk Volume of FMM Grid

$$\Delta V_{b,i} = V_{b,i+1} - V_{b,i} \tag{3.11}$$

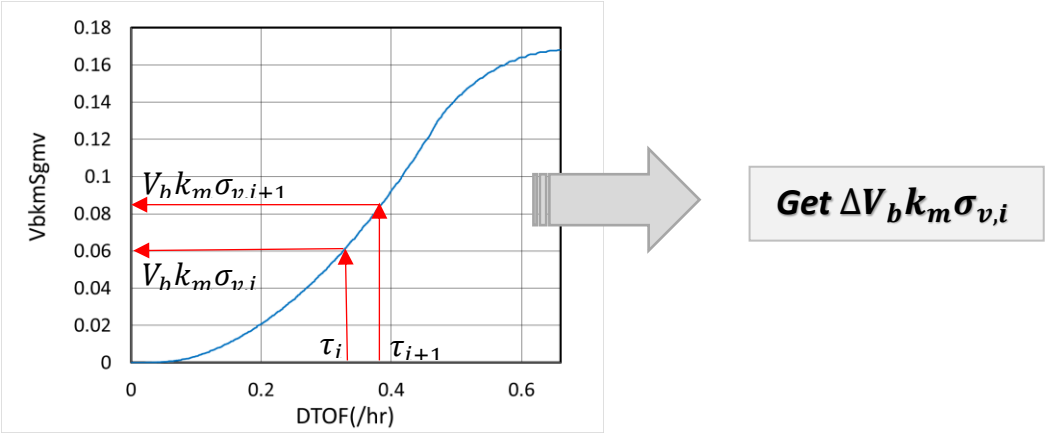

Fig. 3.13 – The Calculation of Vb x km x sigmav (Arithmetic)

$$\Delta V_b k_m \sigma_{v,i} = V_b k_m \sigma_{v,i+1} - V_b k_m \sigma_{v,i} \tag{3.12}$$

$$k_m \sigma_{v,i} = \frac{\Delta V_b k_m \sigma_{v,i}}{\Delta V_{b,i}} \tag{3.13}$$

Fig. 3.14 represents the relationship between the sum of the bulk volume of Cartesian grid model and each DTOF. Interpolating each DTOF at FMM grids, you can obtain the sum of the bulk volume. By taking the difference of these two sums, you can get the bulk volume of the corresponding FMM grid. As for the arithmetic averaging method, you can gain $\Delta V_b k_m \sigma_{v,i}$ in the same manner. Here, k_m denotes the matrix permeability and σ_v represents the shape factor at the FMM grid. Lastly, from **Eq. (3.13)**, you can back-calculate $k_m \sigma_v$ at the corresponding FMM grid. In case of harmonic and geometric averaging methods, this value can be calculated through the use of the following equations. Incomplete Layer based average is calculated by taking the square root of the arithmetic average and the harmonic average at each FMM grid.

For Harmonic Mean:

$$\Delta(\frac{V_b}{k_m\sigma_v})_i = (\frac{V_b}{k_m\sigma_v})_{i+1} - (\frac{V_b}{k_m\sigma_v})_i \tag{3.14}$$

$$k_m\sigma_{v,i} = \frac{\Delta V_{b,i}}{\Delta(\frac{V_b}{k_m\sigma_v})_i} \tag{3.15}$$

For Geometric Mean:

$$\Delta V_b log(k_m\sigma_v)_i = V_b log(k_m\sigma_v)_{i+1} - V_b log(k_m\sigma_v)_i \tag{3.16}$$

$$k_m\sigma_{v,i} = 10\text{^}(\frac{\Delta V_b \log(k_m\sigma_v)_i}{\Delta V_{b_i}}) \tag{3.17}$$

For Incomplete Layer:

$$k_m\sigma_{v,i} = \sqrt{k_m\sigma_{v,i}{}_{Arithmetic} k_m\sigma_{v,i}{}_{Harmonic}} \tag{3.18}$$

3.6 Input Data and Variable

In this section, the input data used for the case study is shown. Next, the type of the variables and their range are determined. Finally, in order to discuss the results, the objective function representing the error is defined.

The input data used as a base case (homogeneous) in this study is summarized in the following table. In order to avoid mixing the error originated from gravity effect, the 2-D reservoir model is used. A production well is located at the center of the reservoir and it produces oil under the bottom hole pressure constraint.

Table. 3.3 – Reservoir Properties for 2-D Model (Base Case)

Region	Name	Value
Reservoir	Grid Number	41 x 41 x 2 (DPSP)
	Grid Size	100 x 100 x 100 cu-ft
Well	Location	(21,21,2)
	Control	BHP=3000 psia
Fracture	Permeability	1 mD
	Porosity	0.01
Matrix	Permeability	0.001 mD
	Porosity	0.1
	Shape Factor	1E-4 /ft^2
Fluid (Oil)	Density (@SC)	63.02 lb/ft^3
Rock	Compressibility	1E-6 /psi @ 6000 psia
Initial Condition	Pressure	5000 psia

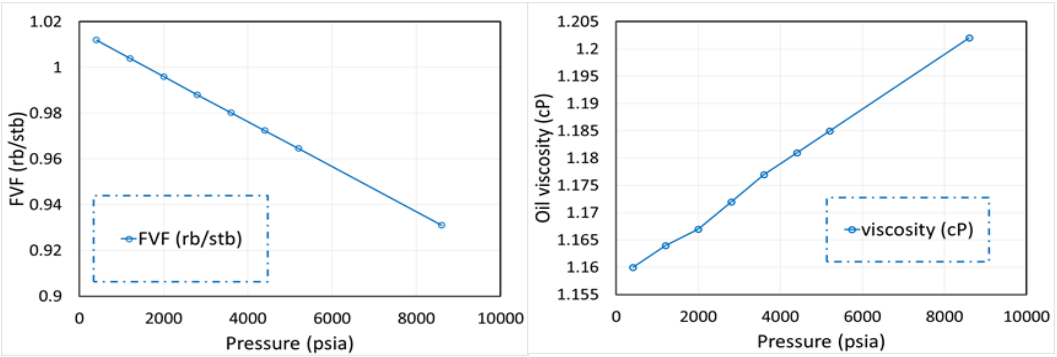

Fig. 3.14 – Pressure Dependent Fluid Properties (Oil Formation Volume Factor, Left and Oil Viscosity, Right)

Next, in order to conduct the case study regarding the matrix heterogeneity, the parameters which may have an influence on error and their ranges are listed. As an indicator for the heterogeneity, the standard deviation of the variable is studied. Besides, as the result is affected by the size of the transmissibility between matrices and fractures, the impact of

average values of the parameters should be investigated as well. Based on the literature review of SPE papers, the standard deviation and the variable range are set for each parameter (matrix permeability, matrix porosity and shape factor) as follows.

Table. 3.4 – Variable Range for Matrix Permeability

Column1	Column2	Column3	Column33	Column32	Column4
Parameter	F / M	Min			Max
Standard Deviation	Matrix	0	0.5	1	1.5
Standard Deviation	Fracture	0	0.3	0.5	1
Ratio of km / kf	Matrix	1e-9 / 1	0.001 / 1	0.05 / 1	

Table. 3.5 – Variable Range for Matrix Porosity

Column1	Column2	Column3	Column33	Column32
Parameter	F / M	Min		Max
Standard Deviation	Matrix	0	0.01	0.03
Standard Deviation	Fracture	0	0.001	0.003
Ratio of porom / porof	Matrix	0.1 / 0.01	0.2 / 0.01	0.3 / 0.01

Table. 3.6 – Variable Range for Matrix Shape Factor

Column1	Column2	Column3	Column33	Column32
Parameter	F / M	Min		Max
Standard Deviation	Matrix	1	1.5	2
Avg	Matrix	1.00E-07	1.00E-04	1.00E-02

Lastly, in order to discuss the results, we need a criterion which represents the corresponding error. As an objective function, the following equation is defined as an error in the case of single phase flow,

$$Error = \frac{1}{N}\sum_{i=1}^{N}\left(\frac{x_i^{true} - x_i^{fmm}}{x_i^{true}}\right)^2 \tag{3.19}$$

where x_i^{true} denotes the oil production rate at the time step, i, calculated from a commercial software and x_i^{fmm} represents the oil production rate at the time step, i, calculated from the FMM based DPSP reservoir simulator.

3.7 Results and Discussion

In this section, the best averaging method is considered from the viewpoint of the error defined above at each standard deviation and average value for the parameters listed in **Chapter 3.5** (i.e. matrix permeability, matrix porosity and shape factor). The 100 different heterogeneous realization maps are used for the purpose of validation for all the cases. First, the errors with regard to averages are shown to study the sensitivity to the average value of each parameter. Second, the errors with different standard deviation are presented. Lastly, by using the realization model which is median (P50) among the 100 cases, the fracture heterogeneity is introduced on top of the matrix heterogeneity to show the robustness of the simulator.

3.7.1 Matrix Permeability

In this section, I studied averaging methods with heterogeneous matrix permeability. Based on the reservoir data shown in **Chapter 3.6**, the heterogeneity is introduced into matrix permeability with 100 different realization maps. Fig.3.17 represents the error with respect to different average of matrix permeability. At each average, 100 cases are tested for the validation purpose. All colored lines connect the average errors of the 100 cases at each point. From this case study, there were not any linear relationships found between

the average value of matrix permeability and the corresponding error. Next, Fig.3.18 represents the error with respect to standard deviation of matrix permeability, and Fig.3.19 shows the histogram of error at std = 1.5. In comparison among these errors, it is observed that the range of the errors calculated from harmonic averaging is quite wide, which indicates the harmonic method is most unstable. On the other hand, the geometric and the incomplete layer based averages tend to generate quite stable errors. Although it is unclear only from Fig.3.18 to tell which is the best method, the average error calculated from the incomplete layer is smaller than that of the geometric method. Hence, the incomplete layer method is selected as the best approach among them for heterogeneous matrix permeability. Lastly, in use of the realization map with median error (P50), the heterogeneity for fracture is introduced in addition to the heterogeneous matrix property to prove the robustness of the simulator. Fig.3.20 represents the error at each fracture heterogeneity, and the colored line connects the average error at each standard deviation. Fig.3.21 describes the oil production rate of P50 at each standard deviation. From the results, you can see that the FMM based DPSP simulator can generate a quite accurate output up to standard deviation with around 0.6 for fracture.

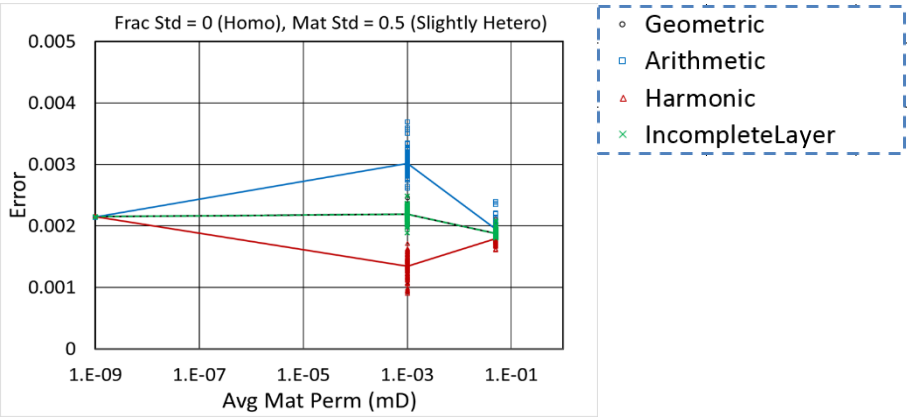

Fig. 3.15 – Error with respect to Average Value for Matrix Permeability

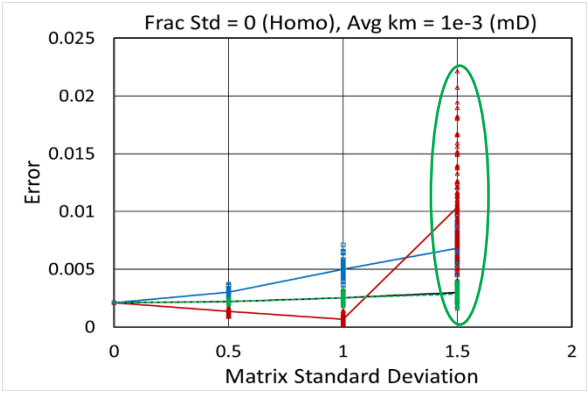

Fig. 3.16 – Error with respect to Standard Deviaition for Matrix Permeability

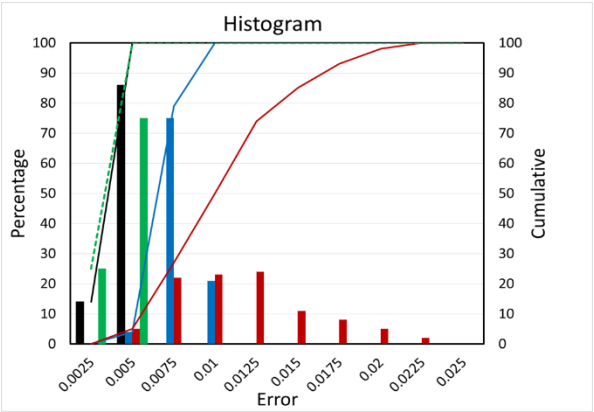

Fig. 3.17 – Histogram at Standard Deviation of 1.5 in Fig.3.16

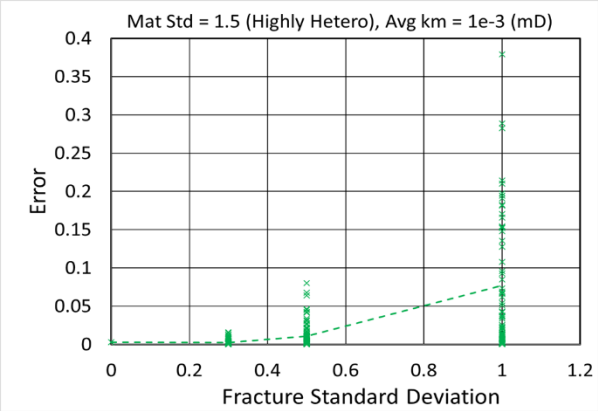

Fig. 3.18 – Error with regard to Fracture Heterogeneity on top of the Heterogeneous Matrix Permeability with P50

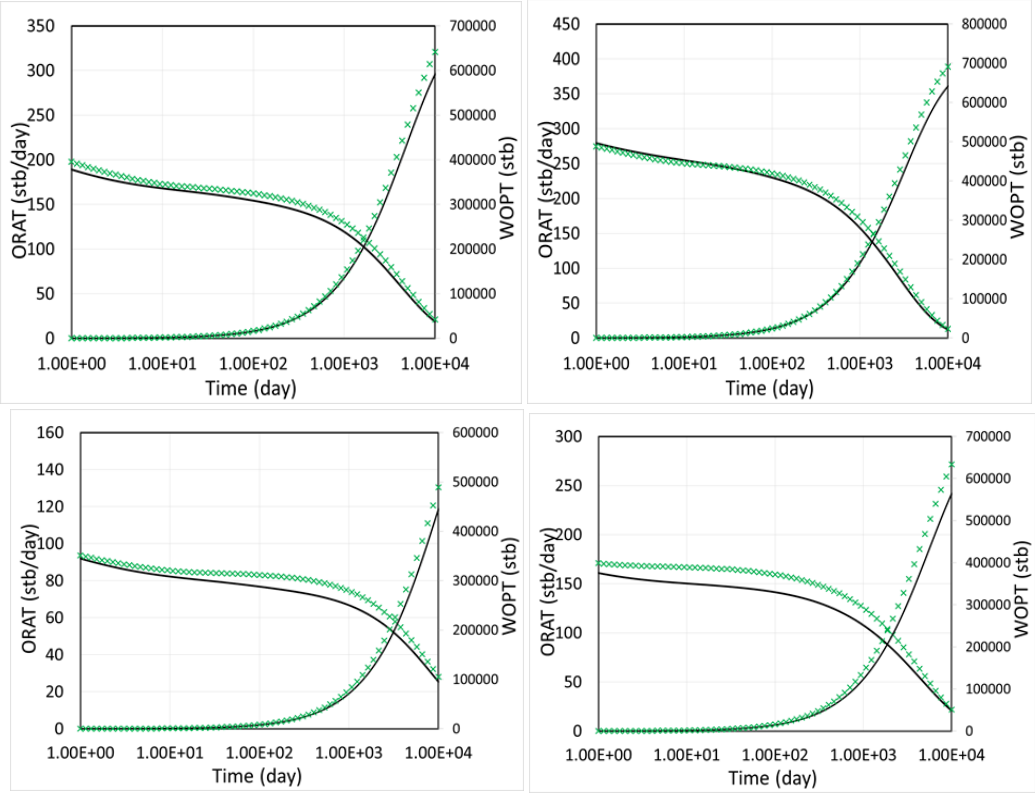

Fig. 3.19 – Oil Production Rate for P50 (std=0 for the Upper Left, std=0.3 for the Upper Right, std=0.5 for the Lower Left and std=1 for the Lower Right)

3.7.2 Matrix Porosity

In this section, the volumetric based averaging was tested with respect to heterogeneity of matrix porosity so that the mass balance equation (MBE) should be preserved. Based on the reservoir data shown in **Chapter 3.6**, the heterogeneity is introduced into matrix porosity with 100 different realization maps. Fig.3.22 represents the error regarding the different average of matrix porosity. At each average, 100 cases are tested for the validation purpose. The black lines connect the average errors of the 100 cases at each point. Next, Fig.3.23 represents the error with respect to standard deviation of matrix porosity. In comparison of these results, it is observed that by taking the volumetric based averaging for matrix porosity, the corresponding error stays almost constant and quite small regardless of the size of the average and the standard deviation. Lastly, in use of the realization map with median error (P50), the heterogeneity for fracture is introduced in addition to the heterogeneous matrix property to prove the robustness of the simulator. Fig.3.24 represents the error at each fracture heterogeneity, and the black line connects the average error at each standard deviation. Fig.3.25 describes the oil production rate of P50 at each standard deviation. From the results, the FMM based DPSP simulator can generate quite accurate outputs up to standard deviation with around 0.68 for fracture.

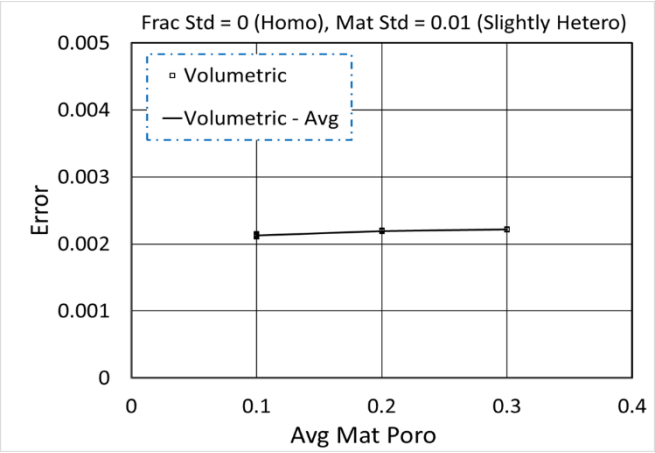

Fig. 3.20 – Error with respect to Average Value for Matrix Porosity

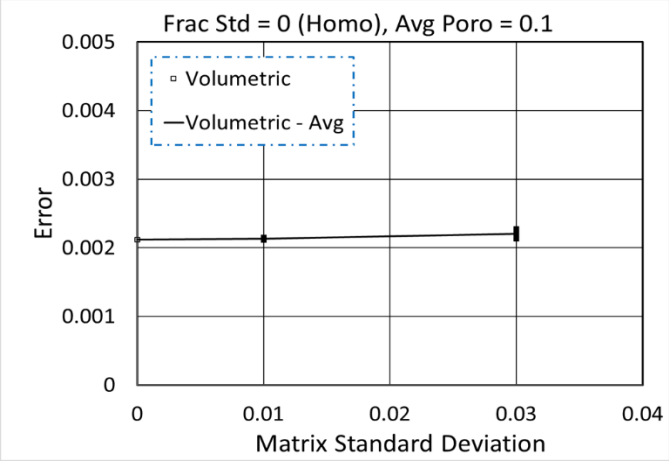

Fig. 3.21 – Error with respect to Standard Deviaition for Matrix Porosity

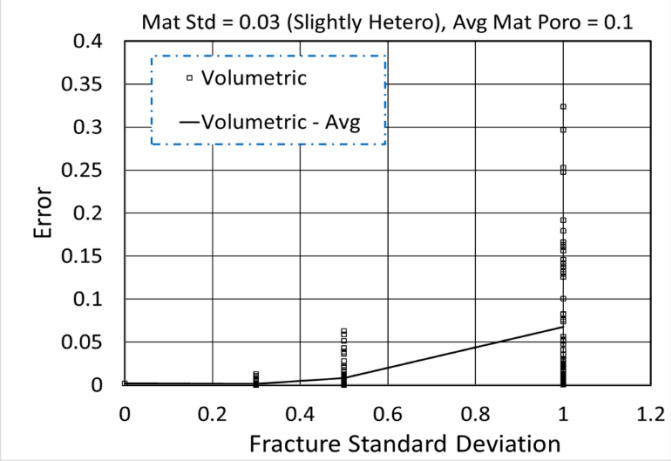

Fig. 3.22 – Error with regard to Fracture Heterogeneity on top of the Heterogeneous Matrix Porosity with P50

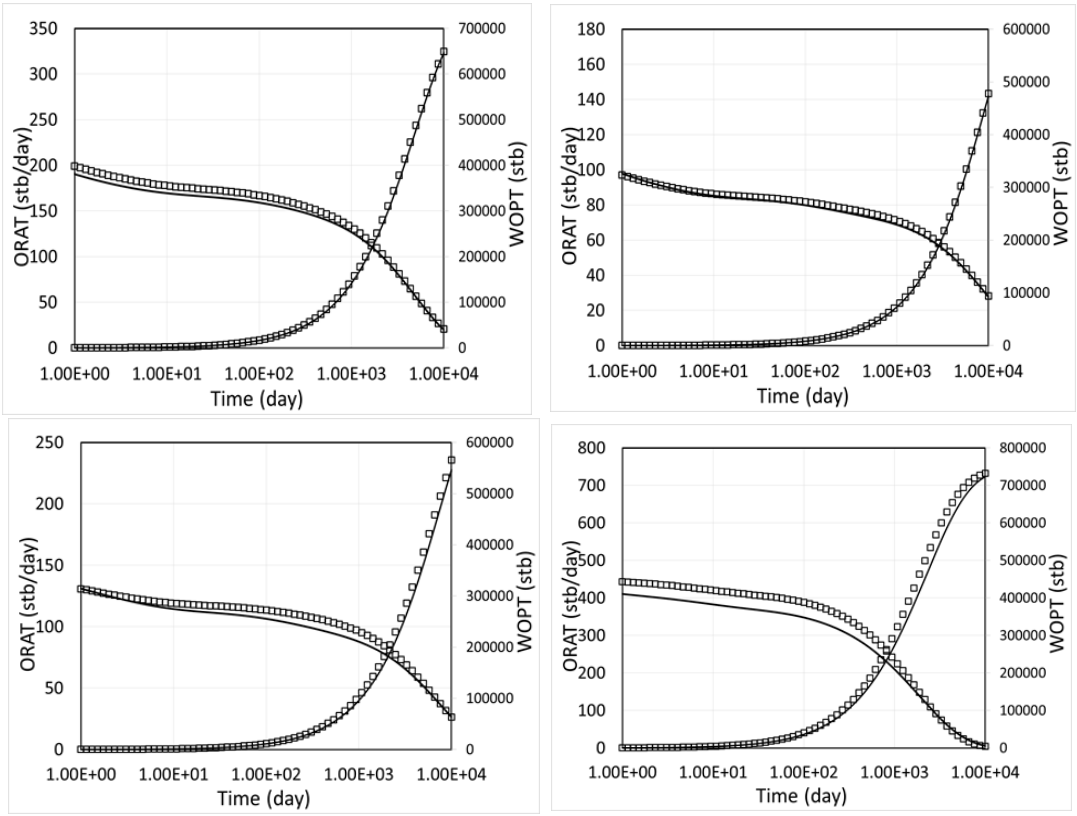

Fig. 3.23 – Oil Production Rate for P50 (std=0 for the Upper Left, std=0.3 for the Upper Right, std=0.5 for the Lower Left and std=1 for the Lower Right)

3.7.3 Matrix Shape Factor

In this section, averaging methods were studied with the heterogeneous matrix shape factor. Based on the reservoir data shown in **Chapter 3.6**, the heterogeneity is introduced into the matrix shape factor with 100 different realization maps. Fig.3.17 represents the error with respect to different averages of the matrix shape factor. At each average, 100 cases are tested for the validation purpose. The colored line connects the average errors of the 100 cases at each point. In this section, the sensitivity of heterogeneous matrix shape

factor was tested separately from that of the matrix permeability since the matrix shape factor, by and large, should be distributed along with DTOF unlike the matrix permeability. However, the overall tendency of its results were found to be similar to that of the matrix permeability because the transmissibility in the DTOF coordinate is expressed as a product of the matrix permeability and the matrix shape factor. From this case study, there were no linear relationships found between the average value of the matrix shape factor and the corresponding error. Next, Fig.3.18 represents the error with respect to standard deviation of the matrix shape factor. In comparison to the results, the range of the errors calculated from the harmonic averaging is quite wide, which indicates the harmonic method is most unstable. On the other hand, the geometric and the incomplete layer based averages tend to generate quite stable errors. In the same manner as the matrix permeability, the PDF and CDF are drawn for the case of standard deviation of 2.0. The incomplete layer method is selected as the best approach among them for the heterogeneous matrix shape factor. Lastly, in use of the realization map with median error (P50), the heterogeneity for fracture is introduced in addition to the heterogeneous matrix property to prove the robustness of the simulator. Fig.3.20 represents the error at each fracture heterogeneity, and the colored line connects the average error at each standard deviation. Fig.3.21 describes the oil production rate of P50 at each standard deviation. From the results, the FMM based DPSP simulator can generate quite accurate outputs up to standard deviation with around 0.6 for fracture.

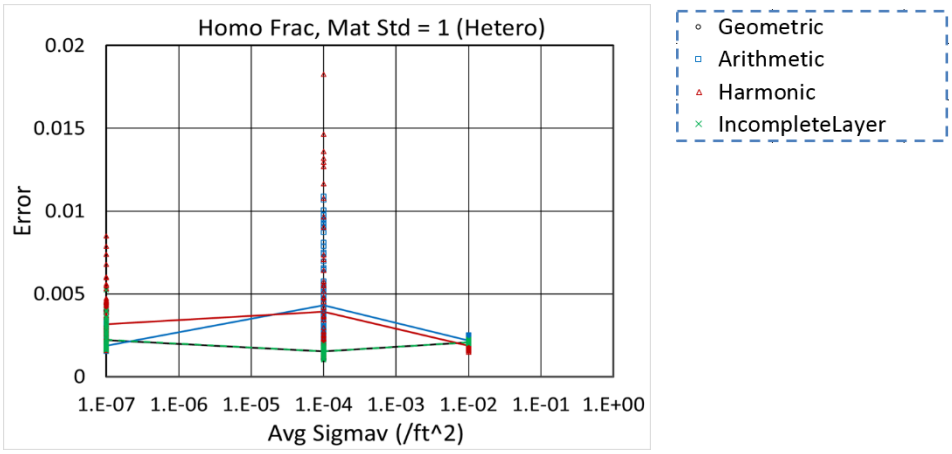

Fig. 3.24 – Error with respect to Average Value for Matrix Shape Factor

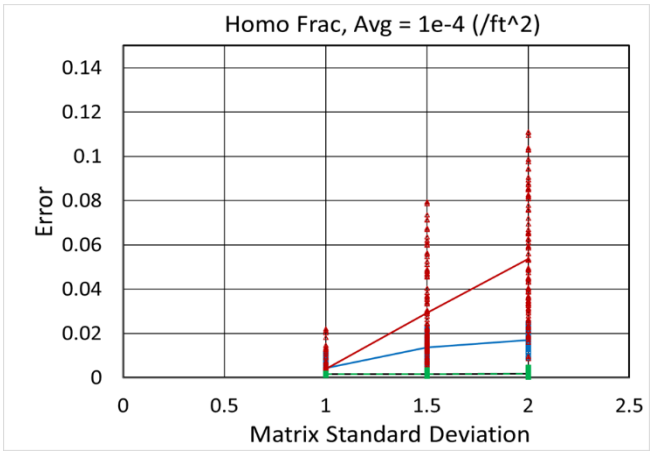

Fig. 3.25 – Error with respect to Standard Deviation for Matrix Shape Factor

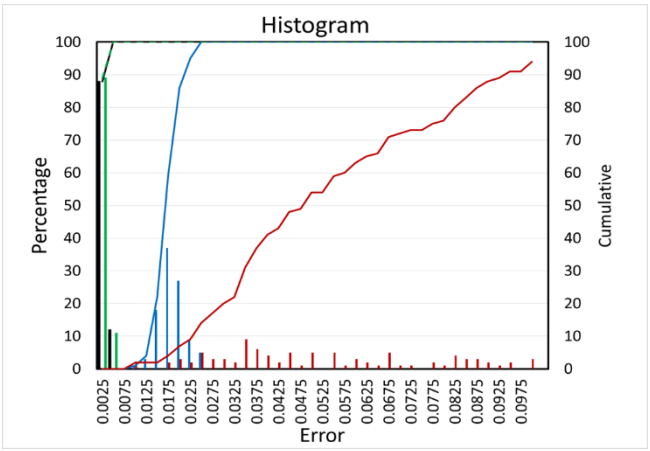

Fig. 3.26 – Histogram at Standard Deviation of 1.5 in Fig.3.25

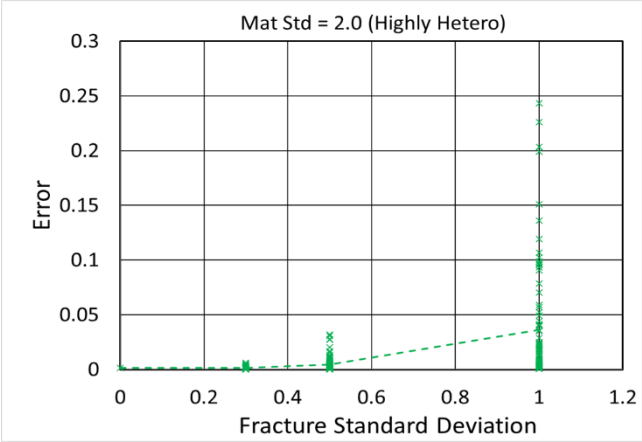

Fig. 3.27 – Error with regard to Fracture Heterogeneity on top of the Heterogeneous Matrix Shape Factor with P50

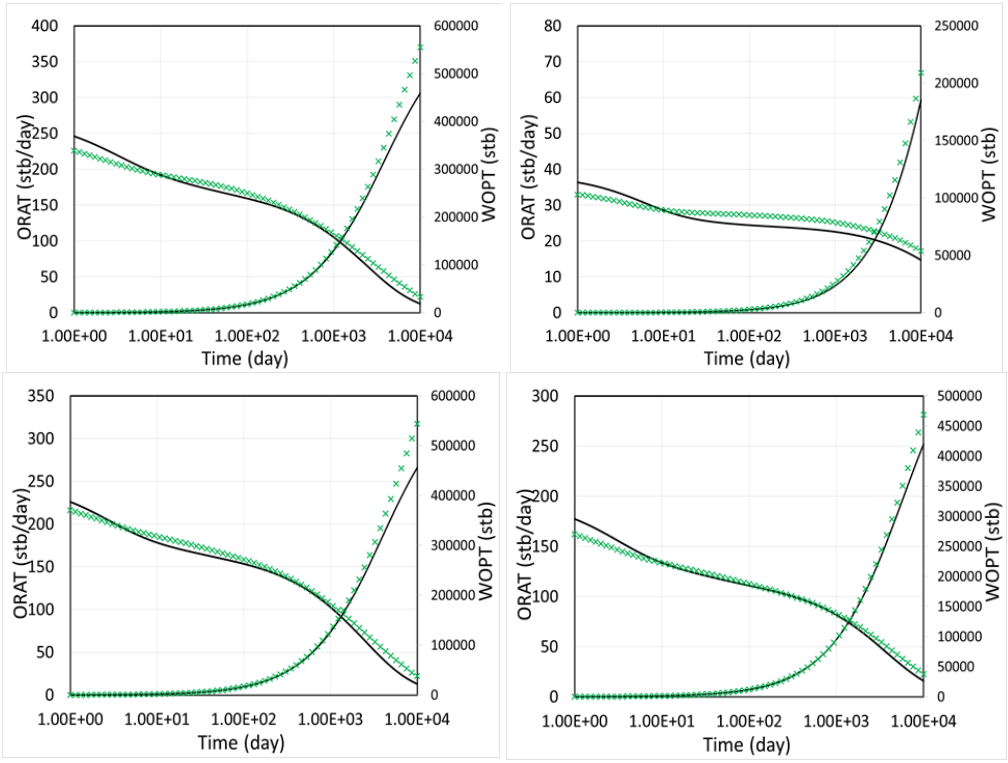

Fig. 3.28 – Oil Production Rate for P50 (std=0 for the Upper Left, std=0.3 for the Upper Right, std=0.5 for the Lower Left and std=1 for the Lower Right)

3.8 Conclusion

In this chapter, averaging for the matrix properties were tested such as permeability, porosity and shape factor. As for matrix porosity, the volumetric based averaging is taken so that the mass balance equation should hold. In use of the volumetric averaging method, the corresponding error stays small regardless of the size of the average and standard deviation. In terms of the permeability and the shape factor, the four approaches are tried: arithmetic, harmonic, geometric and incomplete layer. Among them, the range of the error calculated from the harmonic averaging is quite wide, which indicates the harmonic method is most unstable. On the other hand, the geometric and the incomplete layer based averages tend to generate quite stable errors regardless of the size of the average and standard deviation. Lastly, the fracture heterogeneity is also introduced to the model on top of the matrix heterogeneity to prove the robustness of the simulator. These results show that by taking an appropriate averaging approach, the FMM based DPSP simulator is applicable for heterogeneous reservoir models.

CHAPTER IV

EXTENSION OF DUAL POROSITY FMM INTO MULTI-PHASE FLOW

4.1 Introduction to Multi-Phase Flow

This chapter applies the averaging approach described in the previous chapter into multi-phase flow. First of all, the governing equation for multi-phase flow is explained. To begin with **Eq. (2.1)**, the equation below is derived with respect to each component.

$$\frac{\partial(\phi\rho)}{\partial t} = -\nabla \bullet (\rho \mathbf{u}) \tag{2.1}$$

Considering the sink / source term in addition to the above form,

$$\frac{\partial(\phi\rho)}{\partial t} = -\nabla \bullet (\rho \mathbf{u}) + \rho q \tag{4.1}$$

Since each component, oil, water, and gas, is subject to the above form, **Eq. (4.1)** can be expressed as follows with respect to each component,

$$\frac{\partial}{\partial t}(\phi\rho_\alpha S_\alpha) = -\nabla \bullet (\rho_\alpha \mathbf{u}_\alpha) + \rho_\alpha q_\alpha \tag{4.2}$$

where α denotes each component, oil, water, and gas, and S_α represents the saturation of the corresponding phase. In the same manner as the single phase, the velocity for each component, $\mathbf{u}_\alpha$, is approximated in use of Darcy's law.

$$\mathbf{u}_\alpha = -\mathbf{k}\frac{k_{r\alpha}}{\mu_\alpha}\nabla P \tag{4.3}$$

Where $k_{r\alpha}$ denotes the relative permeability of each phase. Substituting **Eq. (4.3)** into **Eq. (4.2)**, the following form is obtained.

$$\frac{\partial}{\partial t}(\phi\rho_\alpha S_\alpha) = \nabla \bullet \left(\rho_\alpha \frac{k_{r\alpha}}{\mu_\alpha}\mathbf{k}\nabla P\right) + \rho_\alpha q_\alpha \tag{4.4}$$

In the black oil type simulator, it is assumed that there is mass exchange between the oil and gas phase (i.e. through the solution gas in oil and vaporized oil in gas), while the water phase exists independently. Thus, as for the water component, **Eq. (4.4)** can be applied.

$$\frac{\partial}{\partial t}(\phi\rho_w S_w) = \nabla \bullet \left(\rho_w \frac{k_{rw}}{\mu_w}\mathbf{k}\nabla P\right) + \rho_w q_w \tag{4.5}$$

Here, the density can be expressed in the following form,

$$\rho_w = \frac{\rho_{w,sc}}{B_w} \tag{4.6}$$

where B_w represents the formation volume factor for water. In terms of oil, **Eq. (4.4)** can be transformed as follows, considering oil component contained in vaporized gas phase,

$$\begin{aligned}\frac{\partial}{\partial t}\left[\phi\left(\rho_{oo}S_o + R_v\rho_{og}S_g\right)\right] \\ = \nabla \bullet \left[\mathbf{k}\left(\rho_{oo}\frac{k_{ro}}{\mu_o} + R_v\rho_{og}\frac{k_{rg}}{\mu_g}\right)\nabla P\right] + \rho_{oo}q_o + R_v\rho_{og}q_g\end{aligned} \tag{4.7}$$

where R_v represents the ratio of the vaporized oil component in the gas phase and ρ_{oo} and ρ_{og} denote the mass density of the oil in oil phase, that of gas component in the oil phase, respectively. These densities can be expressed in the following form.

$$\rho_{oo} = \frac{\rho_{o,sc}}{B_o}, \qquad \rho_{og} = \frac{\rho_{o,sc}}{B_g} \tag{4.8}$$

In the same way, **Eq. (4.4)** can be transformed with respect to the gas component,

$$\begin{aligned}\frac{\partial}{\partial t}\left[\phi\left(\rho_{gg}S_g + R_{so}\rho_{go}S_o\right)\right] \\ = \nabla \bullet \left[\mathbf{k}\left(\rho_{gg}\frac{k_{rg}}{\mu_g} + R_{so}\rho_{go}\frac{k_{ro}}{\mu_o}\right)\nabla P\right] + \rho_{gg}q_g \\ + R_{so}\rho_{go}q_o\end{aligned} \tag{4.9}$$

where R_{so} denotes the solution gas oil ratio and and ρ_{gg} and ρ_{go} denote the mass density of the gas component in the gas phase, that of the gas component in the oil phase, respectively. These densities can be expressed in the following form.

$$\rho_{gg} = \frac{\rho_{g,sc}}{B_g}, \qquad \rho_{go} = \frac{\rho_{g,sc}}{B_o} \tag{4.10}$$

Dividing **Eqs. (4.5)**, **(4.7)**, and **(4.9)** by **Eqs. (4.6)**, **(4.8)**, and **(4.10)**, respectively, the following governing equations are derived in terms of component.

Mass Balance for Water:

$$\frac{\partial}{\partial t}\left(\phi \frac{S_w}{B_w}\right) = \nabla \bullet \left(\mathbf{k} \frac{k_{rw}}{B_w \mu_w} \nabla P\right) + \frac{q_w}{B_w} \tag{4.11}$$

Mass Balance for Oil:

$$\frac{\partial}{\partial t}\left[\phi \left(\frac{S_o}{B_o} + R_v \frac{S_g}{B_g}\right)\right] = \nabla \bullet \left[\mathbf{k}\left(\frac{k_{ro}}{B_o \mu_o} + R_v \frac{k_{rg}}{B_g \mu_g}\right) \nabla P\right] + \frac{q_o}{B_o} + R_v \frac{q_g}{B_g} \tag{4.12}$$

Mass Balance for Gas:

$$\frac{\partial}{\partial t}\left[\phi \left(\frac{S_g}{B_g} + R_{so} \frac{S_o}{B_o}\right)\right] = \nabla \bullet \left[\mathbf{k}\left(\frac{k_{rg}}{B_g \mu_g} + R_{so} \frac{k_{ro}}{B_o \mu_o}\right) \nabla P\right] + \frac{q_g}{B_g} + R_{so} \frac{q_o}{B_o} \tag{4.13}$$

The additional equation is given by the saturation constraint.

$$S_w + S_o + S_g = 1 \tag{4.14}$$

Eqs. (4.11) – **(4.14)** give the four independent equations to be solved and contain the four primary unknowns: the pressure, P, and each phase saturation, S_o, S_g, S_w. By solving these four non-linear equations, these four unknowns are obtained in the use of discretization.

4.2 Parameters to Be Averaged

In the previous chapter, the three parameters have been averaged in the case of single phase. As for the matrix permeability and the shape factor, there is no guarantee that the best averaging approach for the single phase is always the best for the multi-phase. Thus, the optimum way of averaging is to be studied as well as the single phase. Next, as for the matrix porosity, it is averaged based on the volumetric averaging method so that the mass balance equation should hold. In addition to those three properties, it is necessary to consider averaging for saturation and density. Both of them should be averaged so that the mass balance equation should be preserved as well. Thus, saturation is averaged based on the volumetric average. As for the density, it is determined based on the density at surface condition and the relationship between the formation volume factor and pressure. Since the density at the surface condition is constant, and it is not desirable to change the relationship between the formation volume factor and pressure. The initial pressure is averaged so that it calculates the same density in each FMM grid. The following table summarizes the properties to be averaged in the case of multi-phase flow.

Table.4.1 – Averaging Approach for 3-Phase

Parameter	Method	Comment
k_m	Needed to be studied	-
σ_v	Needed to be studied	-
ϕ_m	Volumetric	To preserve MBE
P_{init} (ρ_l)	So that it generates ρ_l under which MBE holds	To preserve MBE
S_l (k_{rl})	Volumetric	To preserve MBE

4.3 Input Data and Variable

As for the input data shown in Table 4.2, the same reservoir model and the fluid property for oil are used for the matrix permeability, the matrix porosity and the shape factor as those of single phase flow expressed in the previous chapter. The gas fluid properties used in this chapter are shown below.

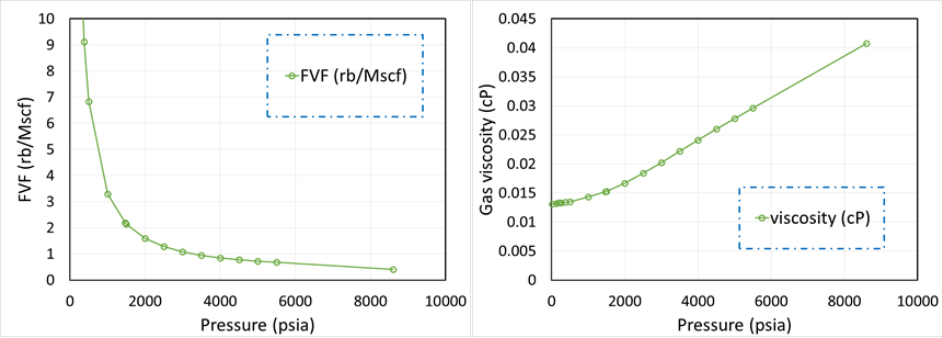

Fig. 4.1 – Pressure Dependent Fluid Property (Gas Formation Volume Factor, Left, and Gas Viscosity, Right)

However, in terms of the density (i.e. initial pressure), the initial pressure is normally given layer by layer. Thus, in order to generate initial pressure heterogeneity, the 3-D reservoir model is assumed. This initial pressure is calculated based on the pressure decline curve along depth used in an example problem of the reservoir engineering textbook (L.P. Dake, Fundamental of Reservoir Engineering). The initial pressure in matrix is usually in equilibrium with that in fracture.

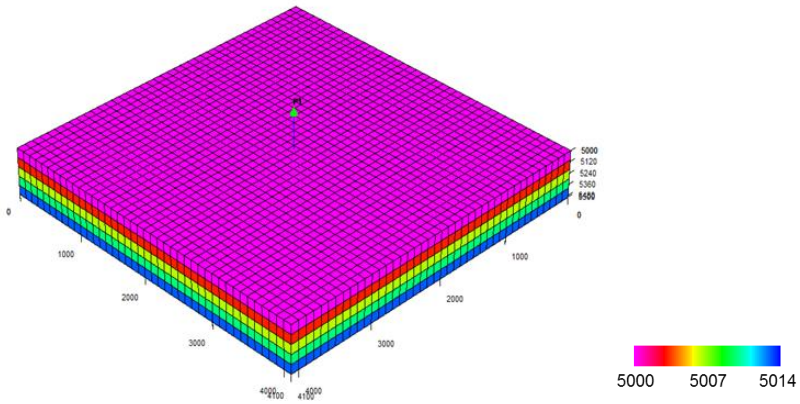

Fig. 4.2 – 3-D Reservoir Model for Density (Initial Pressure)

Table. 4.2 – Reservoir Properties for 3-D Model (Base Case)

Region	Name	Value
Reservoir	Grid Number	41 x 41 x 10 (DPSP)
	Grid Size	100 x 100 x 10 cu-ft
Well	Location	(21,21,10)
	Control	BHP=3000 psia
Fracture	Permeability	1 mD
	Porosity	0.01
Matrix	Permeability	0.001 mD
	Porosity	0.1
	Shape Factor	1E-4 /ft^2
Fluid (Oil)	Density (@SC)	63.02 lb/ft^3
Rock	Compressibility	1E-6 /psi @ 6000 psia
Initial Condition	Pressure	5000 psia @ Tops

As for the saturation, the same reservoir model is used as that of the single phase shown in the previous chapter and the initial water saturation used is described in Table 4.3. In this case, the reservoir is supposed to be in under-saturated condition, and so it is filled

with oil and water. The initial saturation is assumed to be in equilibrium between fracture and matrix.

Table.4.3 – Initial Water Saturation

Column1	Column2	Column3	Column33	Column32
Parameter	F / M	Min		Max
Standard Deviation	Matrix & Fracture	0	0.05	0.1
Avg	Matrix & Fracture		0.4	

Lastly, the objective function for the multi-phase is expressed in summation of the error for each phase.

$$Error = \left[\frac{1}{N}\sum_{i=1}^{N}\left(\frac{x_i^{true} - x_i^{fmm}}{x_i^{true}}\right)^2\right]_O + \left[\frac{1}{N}\sum_{i=1}^{N}\left(\frac{x_i^{true} - x_i^{fmm}}{x_i^{true}}\right)^2\right]_G + \left[\frac{1}{N}\sum_{i=1}^{N}\left(\frac{x_i^{true} - x_i^{fmm}}{x_i^{true}}\right)^2\right]_w \quad (4.15)$$

4.4 Results and Discussion (Synthetic Cases)

In this section, the best averaging method is studied from the viewpoint of the error defined above, at each standard deviation and average value for the parameters listed in **Table 4.1**. The 100 different heterogeneous realization maps are used for the purpose of validation for all of the cases. First, the errors with regard to averages are shown to study the sensitivity to the average value of each parameter. Second, the errors with different standard deviation are presented. Lastly, in the use of the realization model, which is median (P50) among the 100 cases, the fracture heterogeneity is introduced on top of the matrix heterogeneity to show the robustness of the simulator.

4.4.1 Matrix Permeability

In this section, I extended matrix permeability averaging into multi-phase flow. Based on the reservoir data shown, in the previous chapter, the heterogeneity is introduced into matrix permeability with 100 different realization maps. Fig.4.3 represents the error with respect to different averages of matrix permeability. At each average, 100 cases are tested for the validation purpose. Each colored line connects the average errors of the 100 cases at each point. From this case study, there was no linear relationship found between the average value of matrix permeability and the corresponding error. Next, Fig.4.4 represents the error with respect to the standard deviation of the matrix permeability. The range of the errors calculated from harmonic averaging is quite wide, which indicates a harmonic method is most unstable. On the other hand, geometric and incomplete layer based averages tend to generate quite stable errors. Lastly, in the use of the realization map with median error (P50), the heterogeneity for fractures is introduced in addition to the heterogeneous matrix property to prove the robustness of the simulator. Fig.4.6 represents the error at each fracture heterogeneity and the colored line connects the average error at each standard deviation. Fig.4.7 – Fig.4.9 describe the fluid production rate of P50 at each standard deviation. From the results, it can be concluded that the FMM based DPSP simulator can generate quite accurate outputs up to standard deviations of 0.5 as seen in Fig4.4.

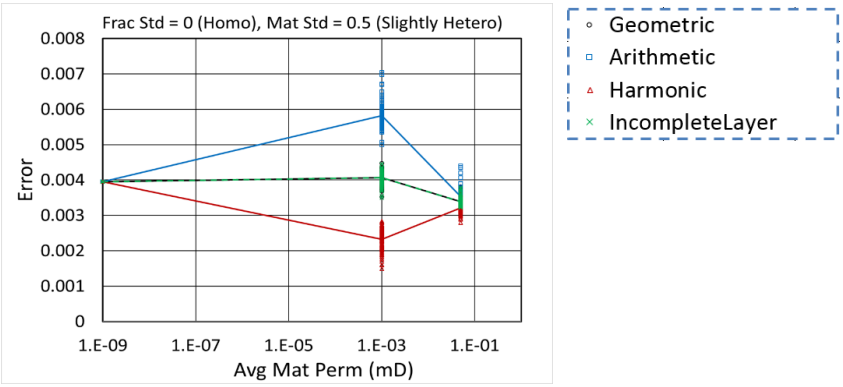

F Fig. 4.3 – Error with respect to Average Value for Matrix Permeability (Multi-Phase)

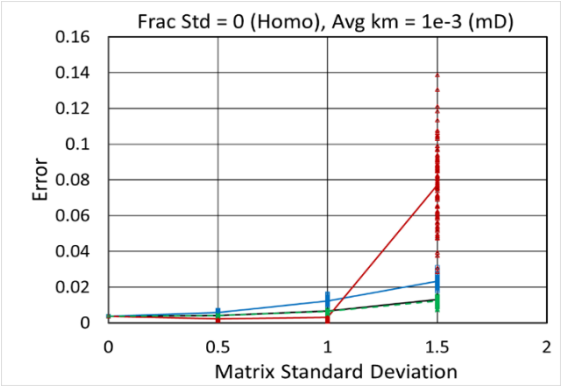

Fig. 4.4 – Error with respect to Standard Deviation for Matrix Permeability (Multi-Phase)

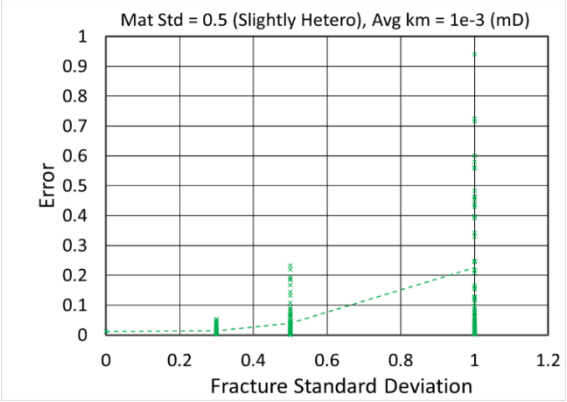

Fig. 4.5 – Error with regard to Fracture Heterogeneity on top of the Heterogeneous Matrix Permeability with P50 (Multi-Phase)

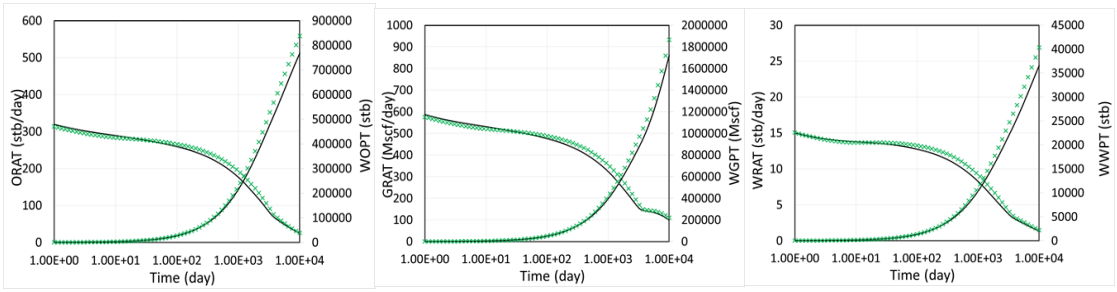

Fig. 4.6 – Fluid Production Rate for P50 (std=1.5 for Matrix Permeability and std=0 for Fracture (Vdp=0))

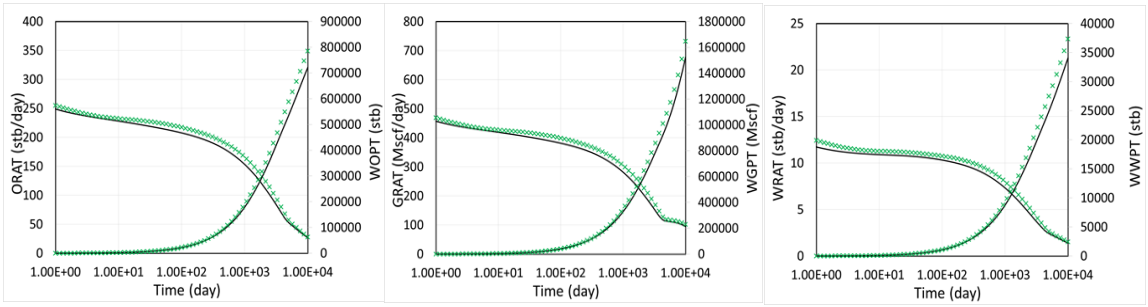

Fig. 4.7 – Fluid Production Rate for P50 (std=1.5 for Matrix Permeability and std=0 for Fracture (Vdp=0.5))

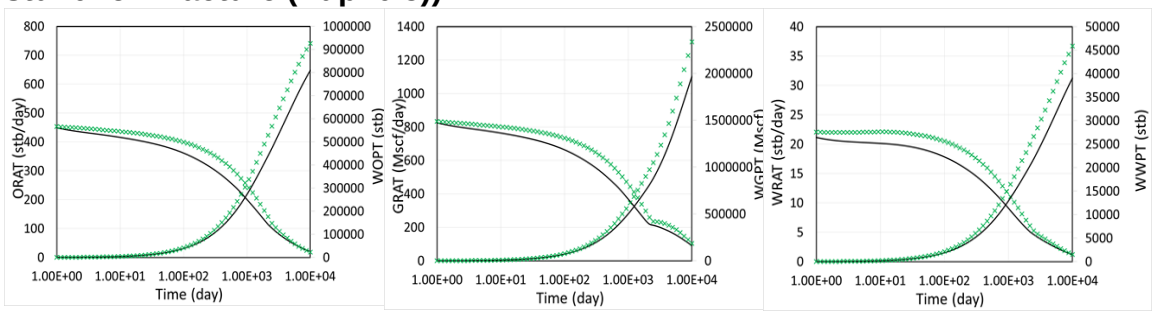

Fig. 4.8 – Fluid Production Rate for P50 (std=1.5 for Matrix Permeability and std=0 for Fracture (Vdp=0.68))

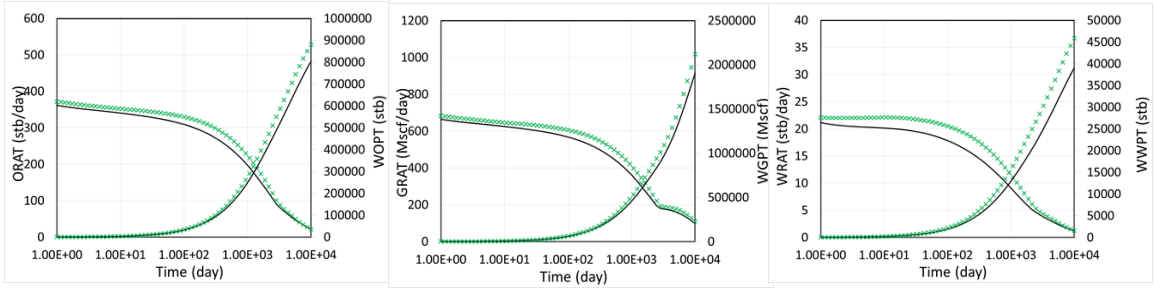

Fig. 4.9 – Fluid Production Rate for P50 (std=1.5 for Matrix Permeability and std=0 for Fracture (Vdp=0.9))

4.4.2 Matrix Porosity

In this section, matrix porosity averaging is extended into multi-phase flow to preserve the mass balance equation (MBE). Based on the reservoir data shown in the previous chapter, the heterogeneity is introduced into a matrix porosity with 100 different realization maps. Fig.4.10 represents the error regarding different averages of matrix porosity. At each average, 100 cases are tested for the purpose of validation. The black lines connect the average errors of the 100 cases at each point. Next, Fig.4.11 represents the error with respect to standard deviation of matrix porosity. The comparison of this result tells that by taking volumetric based averaging for matrix porosity, then the corresponding error stays almost constant and quite small regardless of the size of the average and the standard deviation. Lastly, in the use of the realization map with median error (P50), the heterogeneity for fracture is introduced in addition to the heterogeneous matrix property to prove the robustness of the simulator. Fig.4.12 represents the errors at each fracture heterogeneity and the black line connects the average error at each standard deviation. Fig.4.13 – Fig.4.16 describes the fluid production rate of P50 at each standard deviation. From the results, it can be derived that the FMM based DPSP simulator can generate quite accurate outputs up to standard deviations of 0.68 for fracture.

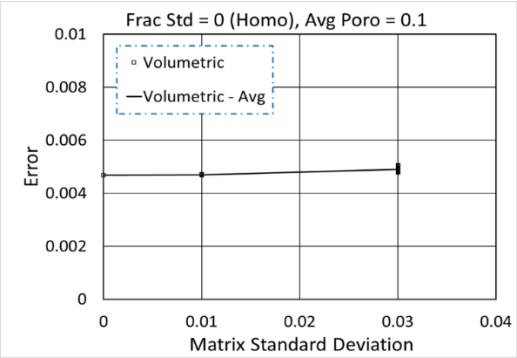

Fig. 4.10 – Error with respect to Average Value for Matrix Porosity (Multi-Phase)

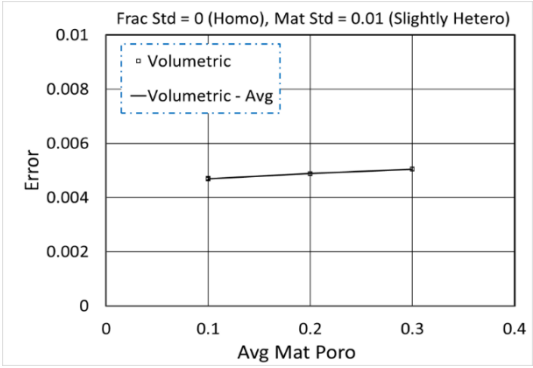

Fig. 4.11 – Error with respect to Standard Deviation for Matrix Porosity (Multi-Phase)

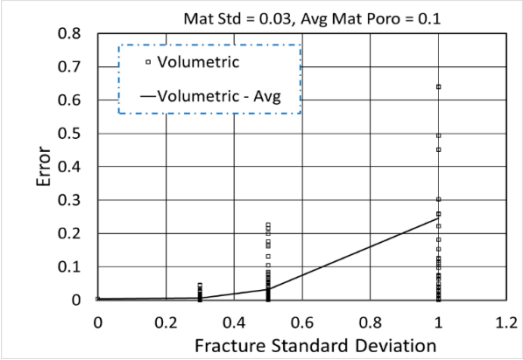

Fig. 4.12 – Error with regard to Fracture Heterogeneity on top of the Heterogeneous Matrix Porosity with P50 (Multi-Phase)

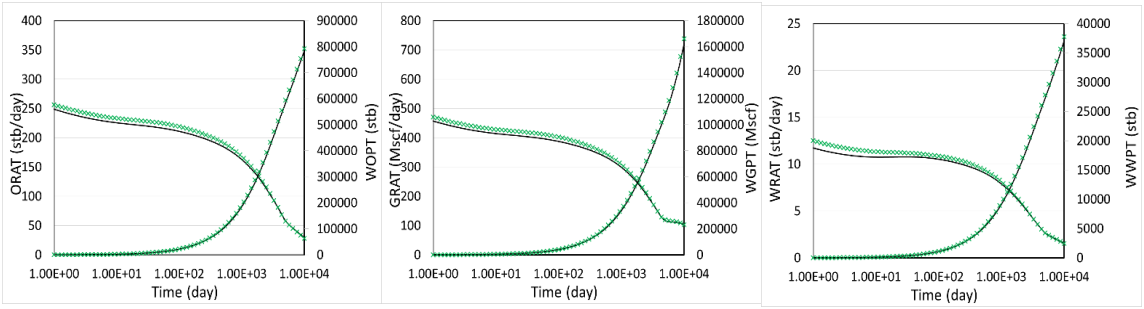

Fig. 4.13 – Fluid Production Rate for P50 (std=0.03 for Matrix Porosity and std=0 for Fracture (Vdp=0))

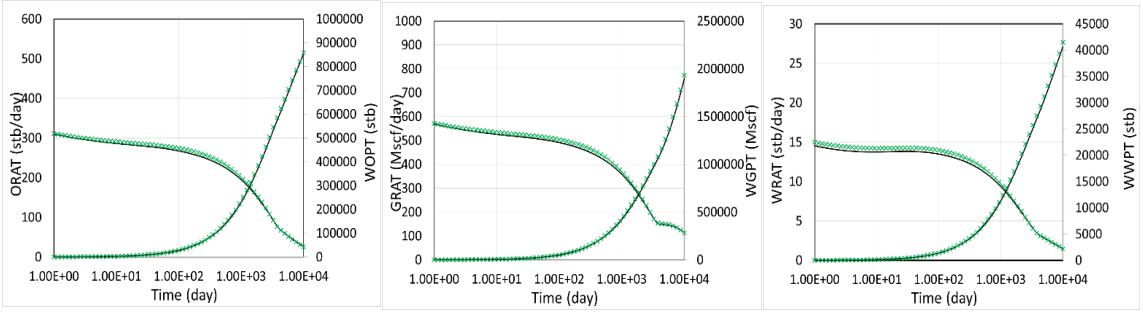

Fig. 4.14 – Fluid Production Rate for P50 (std=0.03 for Matrix Porosity and std=0.3 for Fracture (Vdp=0.5))

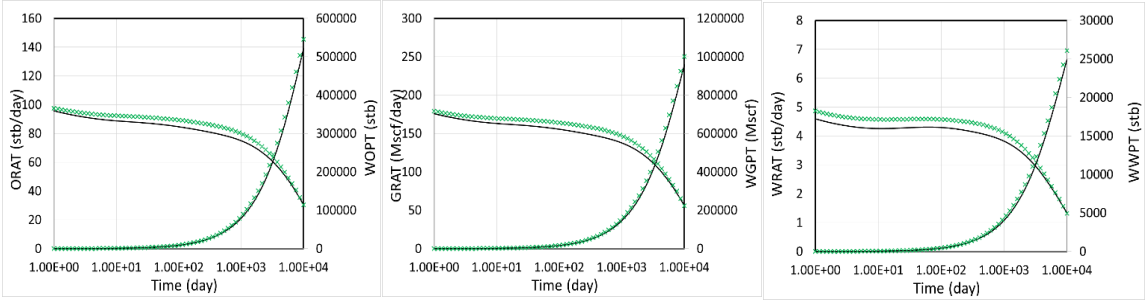

Fig. 4.15 – Fluid Production Rate for P50 (std=0.03 for Matrix Porosity and std=0.5 for Fracture (Vdp=0.68))

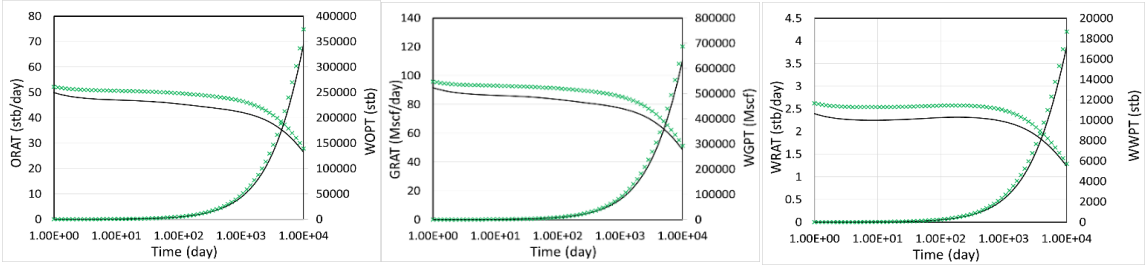

Fig. 4.16 – Fluid Production Rate for P50 (std=0.03 for Matrix Porosity and std=1.0 for Fracture (Vdp=0.9))

4.4.3 Matrix Shape Factor

In this section, matrix shape factor averaging methods are extended into multi-phase flow. Based on the reservoir data shown in the previous chapter, the heterogeneity is introduced into matrix shape factors with 100 different realization maps. Fig.4.17 represents the error with respect to different averages of the matrix shape factors. At each average, 100 cases are tested for the purpose of validation. The colored line connects the average errors of the 100 cases at each point. In this section, the sensitivity of heterogeneous matrix shape factor was tested separately from that of the matrix permeability, but the overall tendency of its results were found to be similar to that of the matrix permeability because of the same reason as that of the single phase flow. From this case study, there was no linear relationship found between the average value of matrix shape factor and the corresponding error. Next, Fig.4.18 represents the error with respect to standard deviation of the matrix shape factor. In the analysis of the results, the range of the errors calculated from harmonic averaging is quite wide, which indicates harmonic method is most unstable. On the other hand, geometric and incomplete layer based averages tend to generate quite stable errors. In the same manner as matrix permeability, the PDF and CDF are drawn for the case of standard deviation of 2.0. An incomplete layer method was selected as the best approach among the proposed methods for heterogeneous matrix shape factor. Lastly, in the use of the realization map with a median error (P50), the heterogeneity for fracture is introduced in addition to the heterogeneous matrix property to prove the robustness of the simulator. Fig.4.19 represents the error at each fracture heterogeneity and the colored lines connect the average error at each standard deviation. Fig.4.20 – Fig.4.23 describe the fluid

production rate of P50 at each standard deviation. From the results, it can be observed that the FMM based DPSP simulator can generate quite accurate outputs up to standard deviations of 0.5 for fracture.

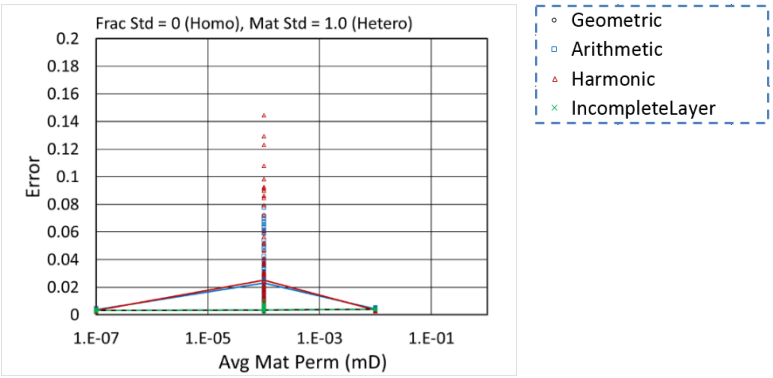

Fig. 4.17 – Error with respect to Average Value for Matrix Shape Factor (Multi-Phase)

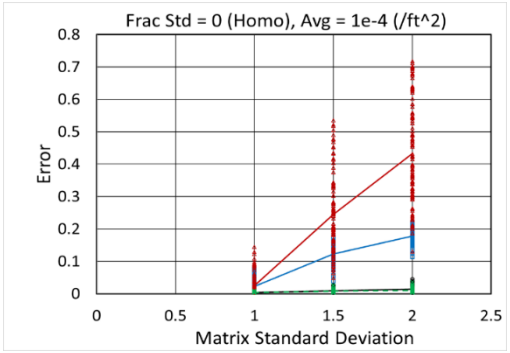

Fig. 4.18 – Error with respect to Standard Deviation for Matrix Shape Factor (Multi-Phase)

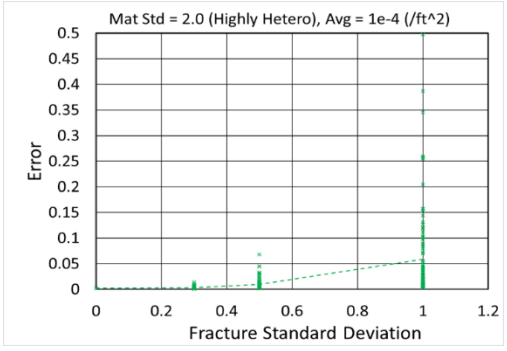

Fig. 4.19 – Error with regard to Fracture Heterogeneity on top of the Heterogeneous Matrix Shape Factor with P50 (Multi-Phase)

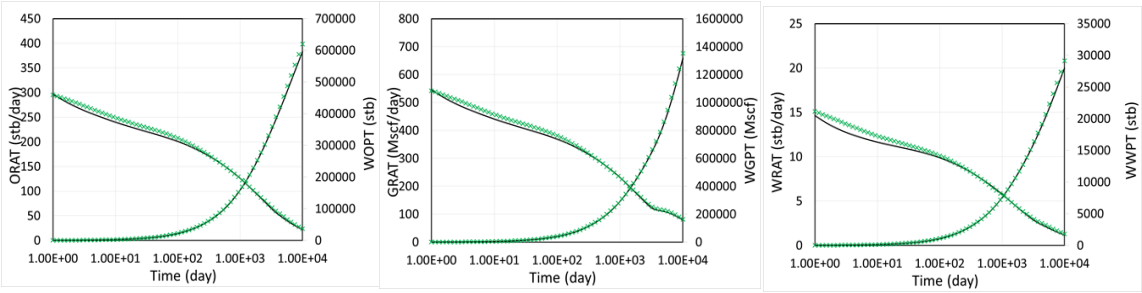

Fig. 4.20 – Fluid Production Rate for P50 (std=2.0 for Shape Factor and std=0 for Fracture (Vdp=0))

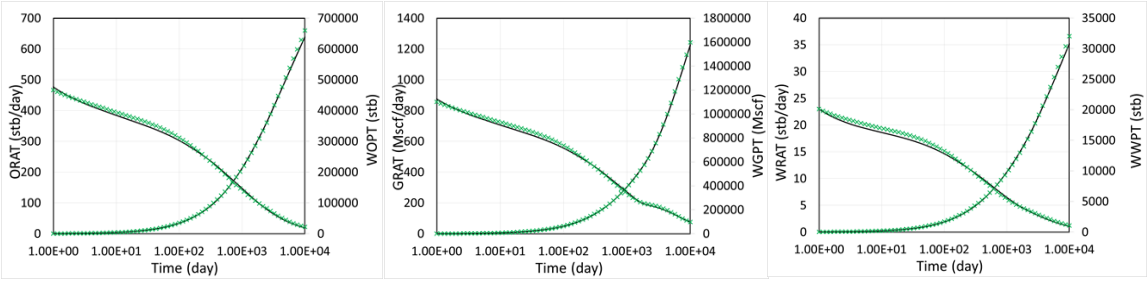

Fig. 4.21 – Fluid Production Rate for P50 (std=2.0 for Shape Factor and std=0.3 for Fracture (Vdp=0.5))

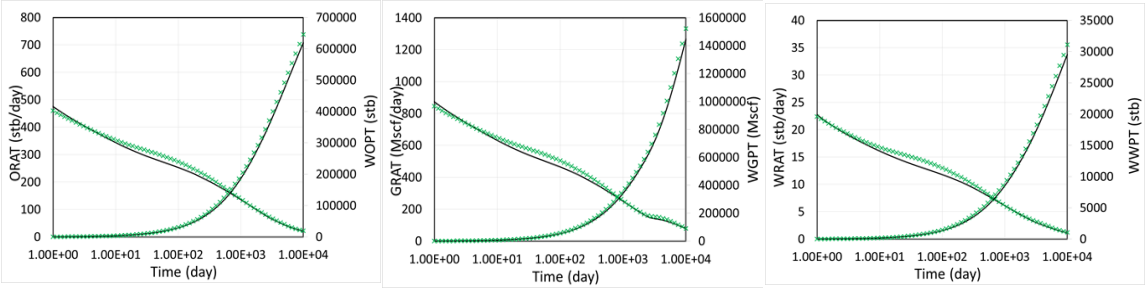

Fig. 4.22 – Fluid Production Rate for P50 (std=2.0 for Shape Factor and std=0.5 for Fracture (Vdp=0.68))

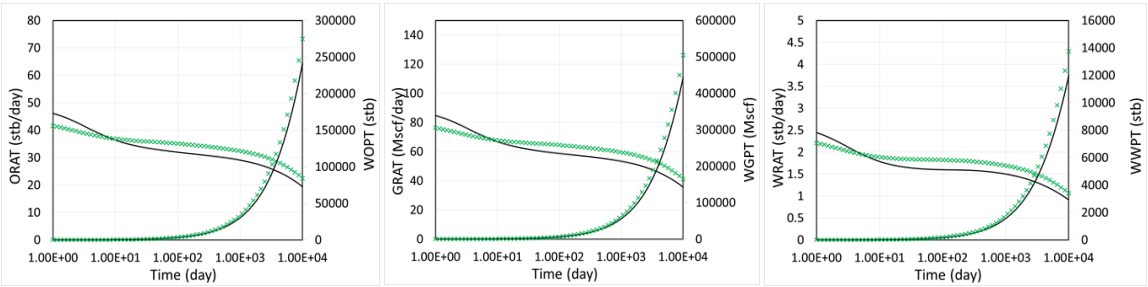

Fig. 4.23 – Fluid Production Rate for P50 (std=2.0 for Shape Factor and std=1.0 for Fracture (Vdp=0.9))

4.4.4 Density (Initial Pressure)

In this section, density averaging was conducted in a manner that selected initial pressure which generates the appropriate density so that material balance equation should hold in each FMM grid. As explained in the Chapter 4.3, a 3-D reservoir model is assumed since initial pressure is normally given layer by layer. Unlike other properties such as permeability or shape factor, heterogeneity for initial pressure distributions cannot be generated from geostatistical commercial softwares. Thus, the averaging is conducted in the use of the 3-D reservoir model described in the previous chapter. The corresponding fluid production rates are shown in comparison with those of commercial reservoir software. From these results, it can be confirmed that by taking appropriate method, the FMM based DPSP simulator can properly take into consideration the heterogeneous initial pressure.

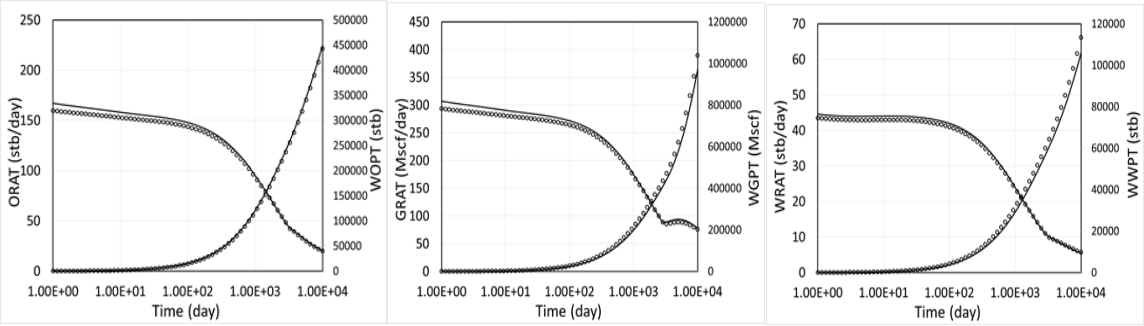

Fig. 4.24 – Fluid Production Rate with Heterogeneous Initial Pressure Distribution

4.4.5 Initial Saturation

In this section, saturation averaging was conducted so that material balance equation should hold in each FMM grid. A 2-D reservoir model is assumed with different standard deviations. The reservoir is supposed to be in under saturated condition. The corresponding fluid production rates are shown in Fig.4.25 in comparison with those of the commercial reservoir software. Fig.4.26 – Fig.4.29 describe the fluid production rate of P50 at each standard deviation. From these results, it can be confirmed that by taking the appropriate method, the FMM based DPSP simulator can properly take into consideration the heterogeneous initial pressure.

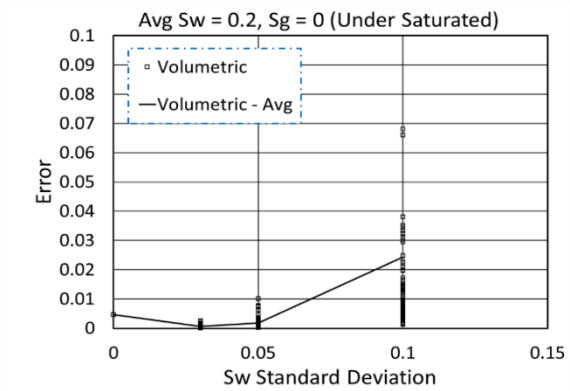

Fig. 4.25 – Error with respect to Standard Deviation for Initial Saturation (Multi-Phase)

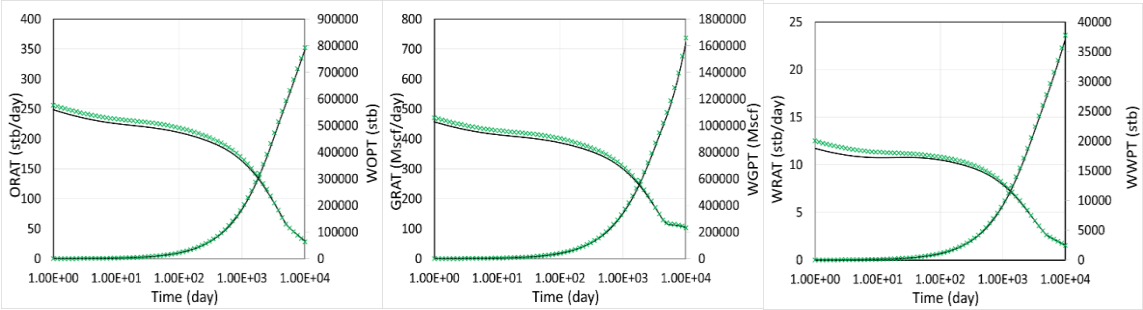

Fig. 4.26 – Fluid Production Rate for P50 (std=0 for Initial Water Saturation at Fracture & Matrix)

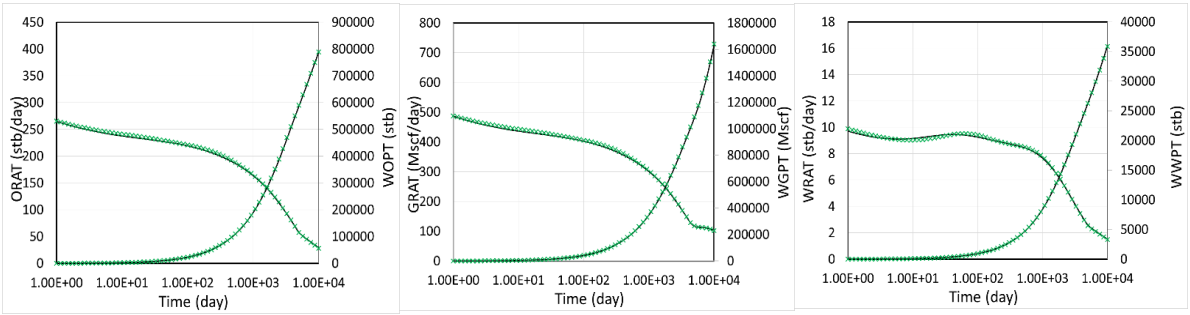

Fig. 4.27 – Fluid Production rate for P50 (std=0.03 for Initial Water Saturation at Fracture & Matrix)

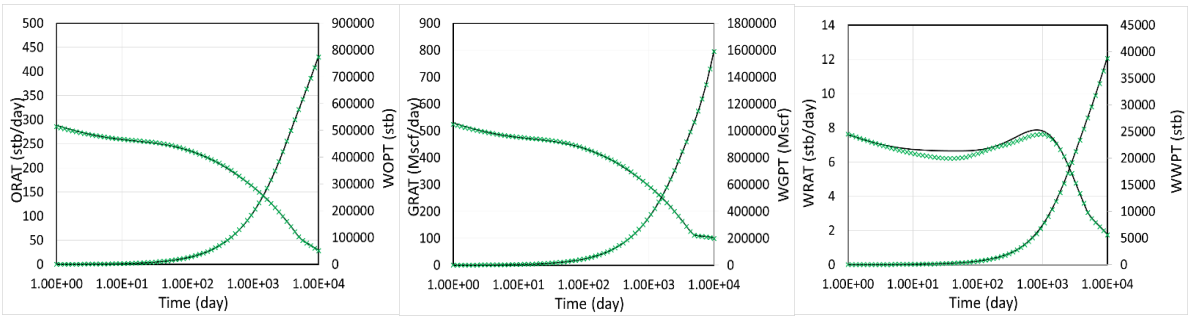

Fig. 4.28 – Fluid Production Rate for P50 (std=0.05 for Initial Water Saturation at Fracture & Matrix)

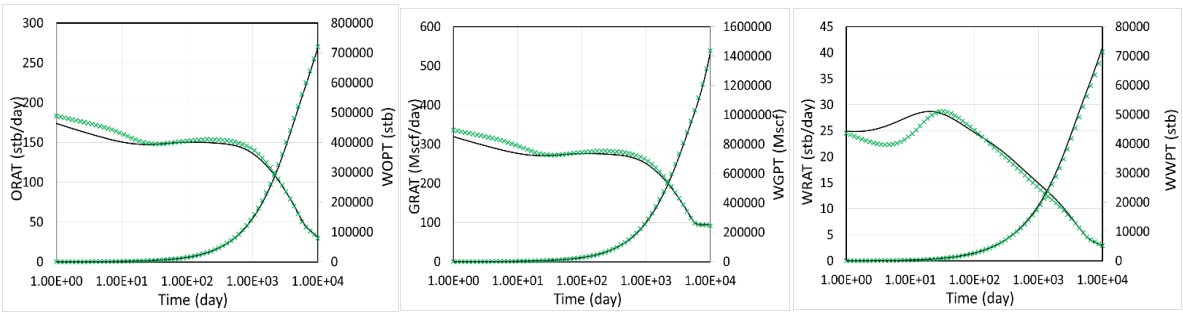

Fig. 4.29 – Fluid Production Rate for P50 (std=0.10 for Initial Water Saturation at Fracture & Matrix)

4.5 Field Application

In this chapter, the field application is conducted using the FMM based DPSP simulator.

In the same manner as Chapter 4.3 and Chapter 4.4, the following five parameters are

averaged: the matrix permeability, the matrix porosity, the shape factor, saturation and density. As discussed above, the three parameters, the matrix porosity, saturation and density, are averaged so that the mass balance equation should hold in each FMM grid. The remaining two of them, the matrix permeability and the shape factor, are tested using arithmetic averaging, harmonic averaging, geometric averaging and the incomplete layer method.

4.5.1 Field Data

In this section, the field data used is described. This reservoir is initially under-saturated and filled with oil and water. Table 4.4 summarizes the reservoir data. This reservoir can be categorized into the three main regions: hydro fracturing part (HF), stimulated reservoir volume part (SRV) and the outer region (Outer). In each region, all the properties have different average values and heterogeneities. The values in the table below correspond to the average values at HF, SRV and Outer, respectively. The production well is located horizontally and controlled by bottom hole pressure constraint. In the end, the five properties to be averaged are illustrated below. Fig.4.30 – Fig.4.34 describe the properties maps for fractures and matrices with respect to permeability, porosity, shape factor, initial water saturation and initial pressure, respectively.

Table 4.4 – Reservoir Properties in Field Data

Region	Name	Value
Reservoir	Number of Grids	71 x 25 x 26 (DPSP)
	Reservoir Size	7500 x 2400 x 300 cu-ft
Well	Type	Horizontal
	Control	BHP
Fracture	Avg Permeability	0.55, 0.1, 5.65E-5 mD
	Avg Porosity	0.01, 0.01, 0.00001
	Water Saturation	0.40, 0.35, 0.05
Matrix	Avg Permeability	2.7E-5 mD
	Avg Porosity	0.08
	Avg Shape Factor	0.005, 0.00125, 1.2E-7 /ft^2
	Water Saturation	0.41
Fluid	Fluid Type	Oil & Water
Initial Condition	Avg Pressure	3940 psia

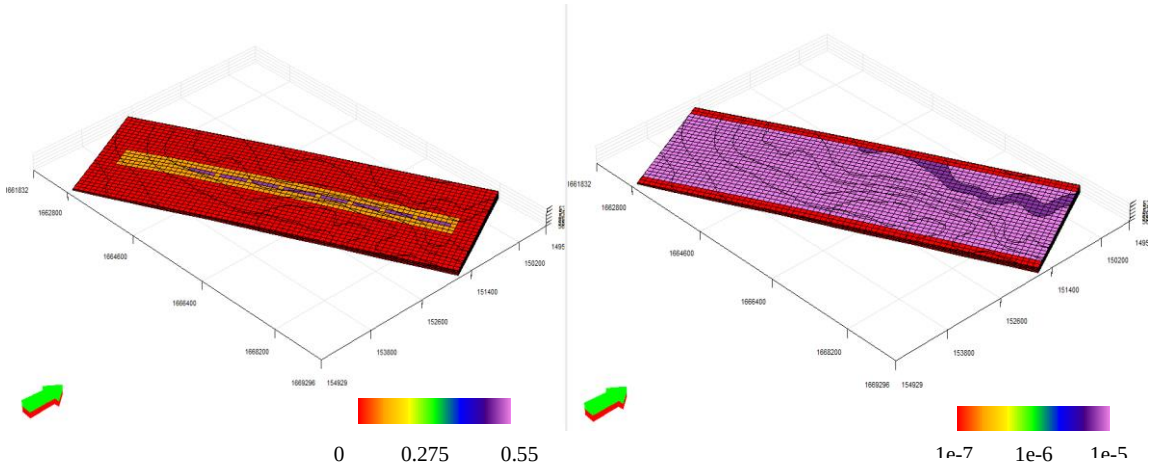

Fig. 4.30 – Permeability Map (the Left for Fractures and the Right for Matrices)

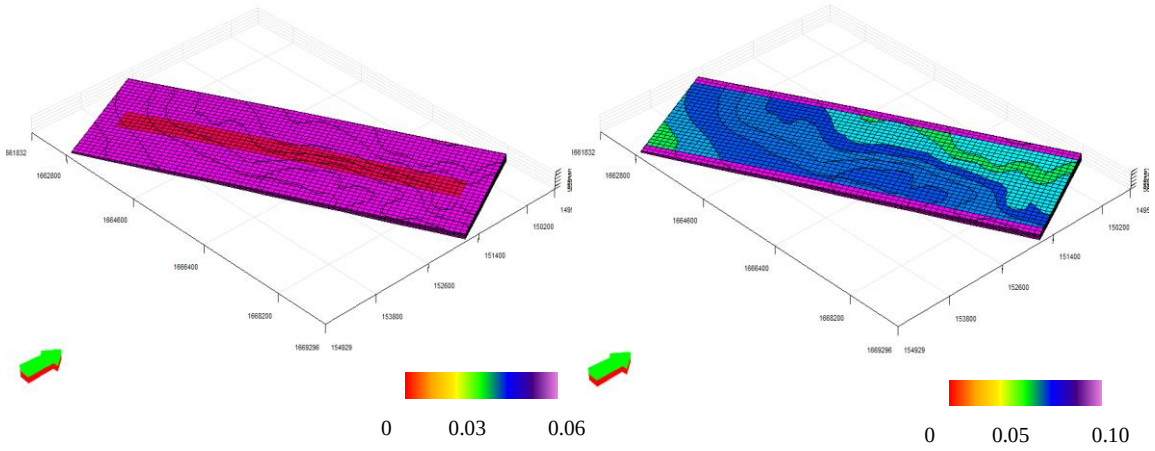

Fig. 4.31 – Porosity Map (the Left for Fractures and the Right for Matrices)

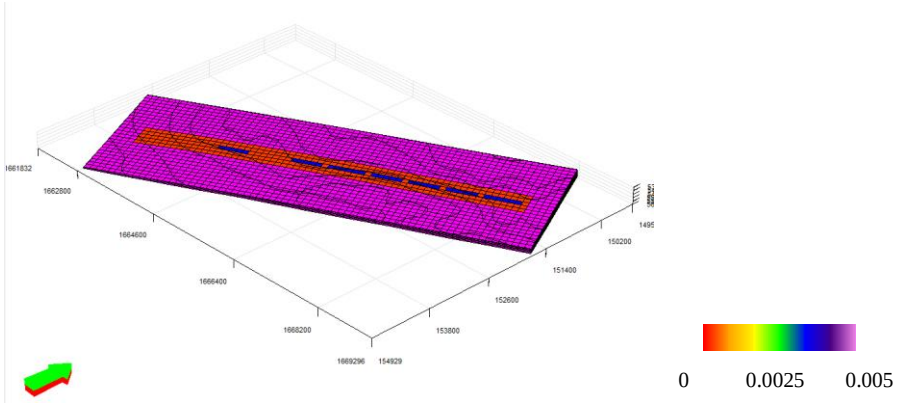

Fig. 4.32 – Shape Factor Map in Matrices

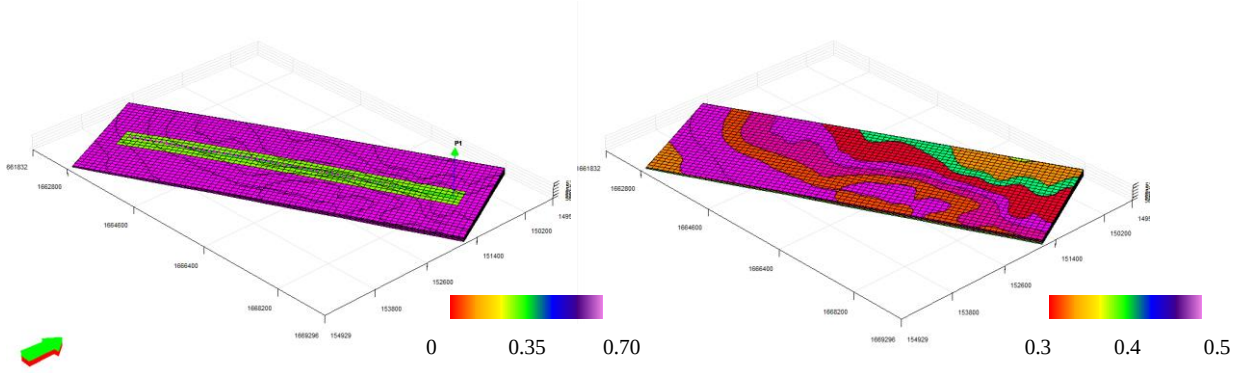

Fig. 4.33 – Water Saturation Map (the Left for Fractures and the Right for Matrices)

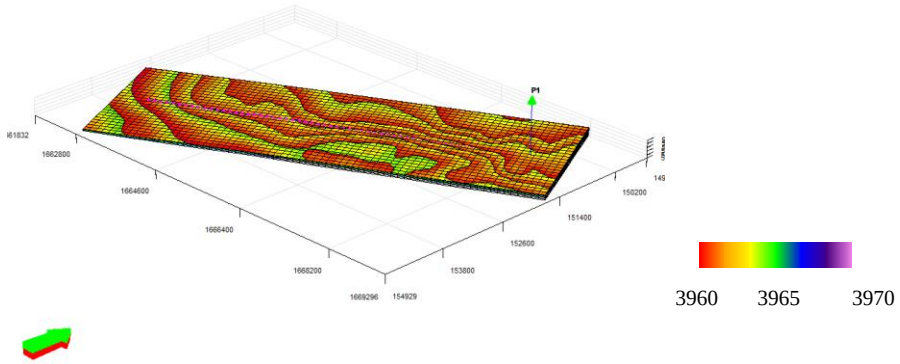

Fig. 4.34 – Initial Pressure Map (Both for Fractures and Matrices)

4.5.2 Results and Discussion

Based on the reservoir data shown in the previous chapter, the fluid was produced for 440 days. The following figures represent the fluid production rate for oil, gas and water, respectively. The black line describes the fluid production rate generated by the commercial software, and the colored lines are those of the FMM based DPSP simulator. From the figures below, it can be observed that the fluid production rate, based on arithmetic averaging, is the most optimistic and that of harmonic averaging is the most pessimistic. The geometric and incomplete layer based results are always between these two lines. The fluid production rate generated by the geometric-based average shows the best match with that of the commercial software. Next, Fig.4.39 and Fig4.40 represent the pressure maps at the initial and final time step for fractures and matrices, respectively. From these figures, it can be observed that the pressure drop is found only in HF and SRV for matrices, although it is found throughout the reservoir (HF, SRV and Outer) for fractures. These illustrations imply that the matrices only in HF and SRV work as fluid

storages, and the matrices in Outer have no influence on fluid production rate. Thus, the reservoir properties in HF and SRV are investigated in more detail. Fig.4.41 describes the scatter plots of the matrix permeability and the shape factor, respectively. The region within the red circle corresponds to HF and SRV. In these scatter plots, the distribution of the matrix permeability is close to homogeneous, which can be confirmed from its Dykstra Parsons Coefficient, $\boldsymbol{\sigma_v}$, of 0.33. According to the definition of Dykstra Parsons Coefficient, the reservoir is supposed to be almost homogenous if its Dykstra Parsons Coefficient is equal to or less than around 0.3. In terms of the shape factor, it can be regarded to be almost homogeneous because its value is distributed region by region (0.005 for HF and 0.00125 for SRV). This fact means that the distribution of matrix properties (the matrix permeability and shape factor) in HF and SRV can be regarded to be almost homogeneous. Thus, the corresponding fluid production rates are close to each other regardless of the different averaging methods. In case of the synthetic case studies conducted in Chapter IV, the fluid production rate based on the geometric and incomplete layer averaging using the FMM simulator was quite close to that of the commercial. However, the fluid production rate based on the incomplete layer method slightly deviates from that of the commercial software. This is because the lower bound of the matrix permeability in the pay zone (within the red circle), illustrated in Fig4.41, is off from the other data points. Generally speaking, if the upper or lower bound is too far away from the other clusters, the incomplete layer averaging is affected too much. Hence, in this field

data, geometric generates the best match with the commercial software. These results are consistent with that of the previous work.

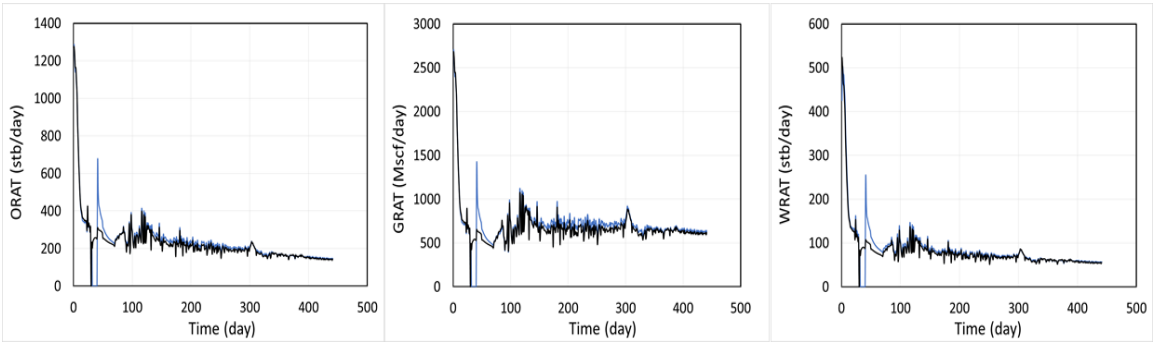

Fig. 4.35 – Fluid Production Rate Based on Arithmetic Averaging (Oil, Gas and Water from the Left)

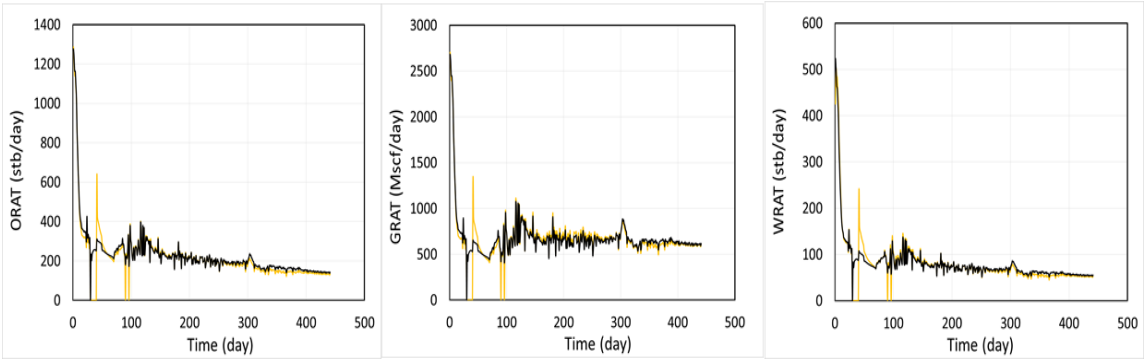

Fig. 4.36 – Fluid Production Rate Based on Geometric Averaging (Oil, Gas and Water from the Left)

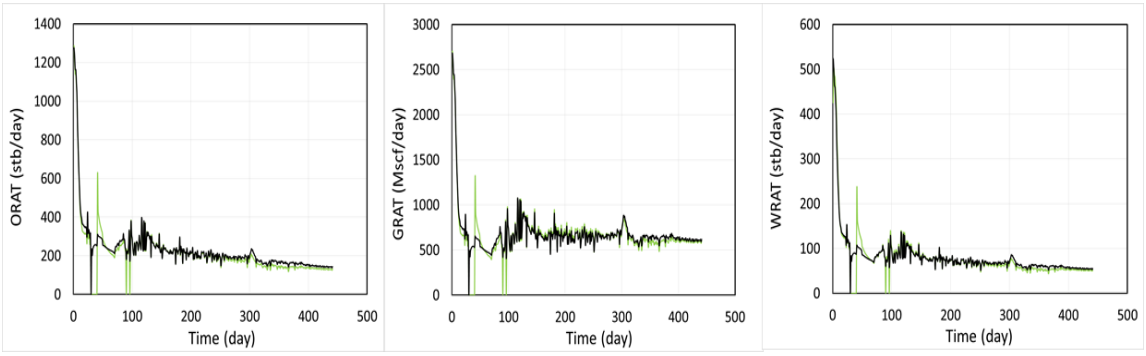

Fig. 4.37 – Fluid Production Rate Based on Incomplete Layer (Oil, Gas and Water from the Left)

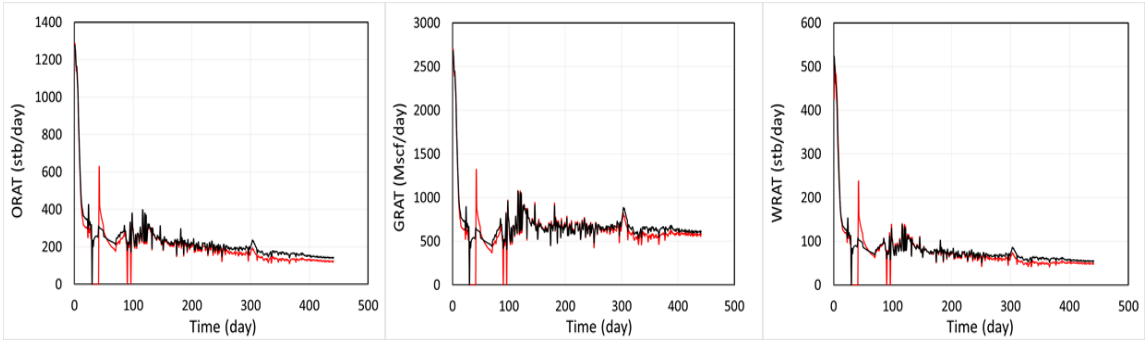

Fig. 4.38 – Fluid Production Rate Based on Harmonic Averaging (Oil, Gas and Water from the Left)

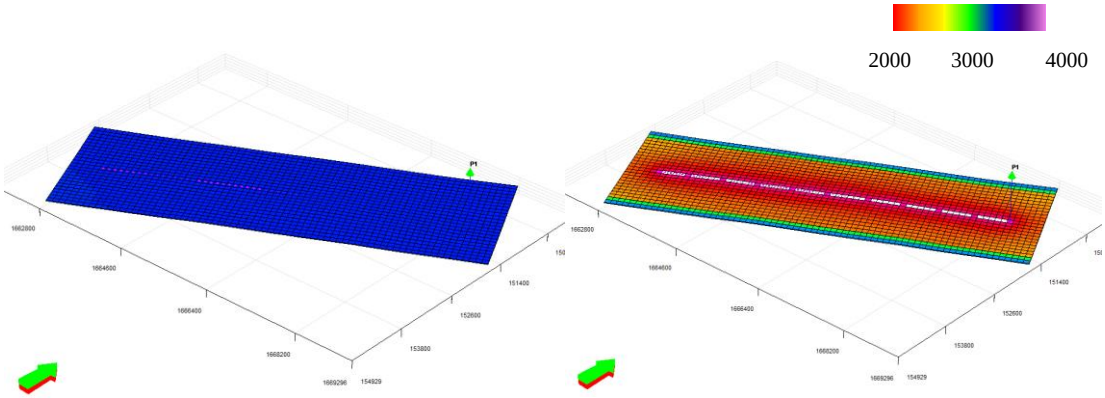

Fig. 4.39 – Pressure Maps in Fractures (Initial, Left and 440 Days after Production, Right)

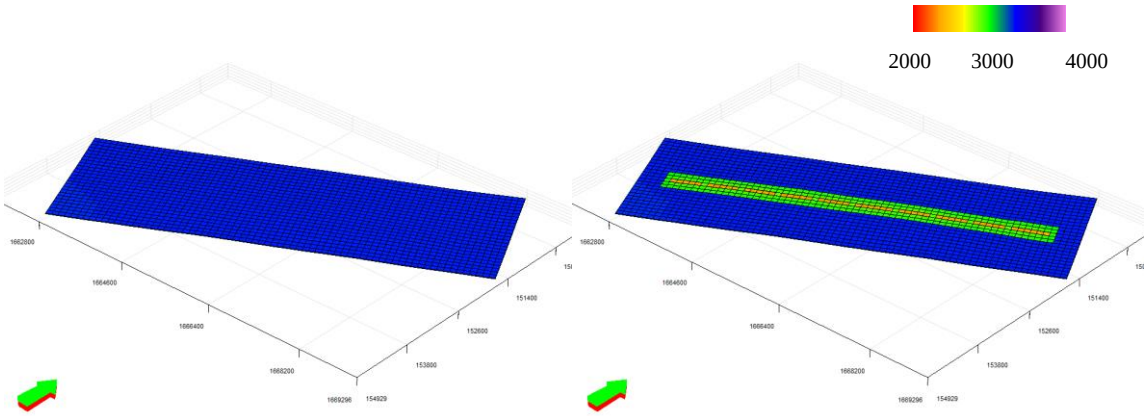

Fig. 4.40 – Pressure Maps in Matrices (Initial, Left and 440 Days after Production, Right)

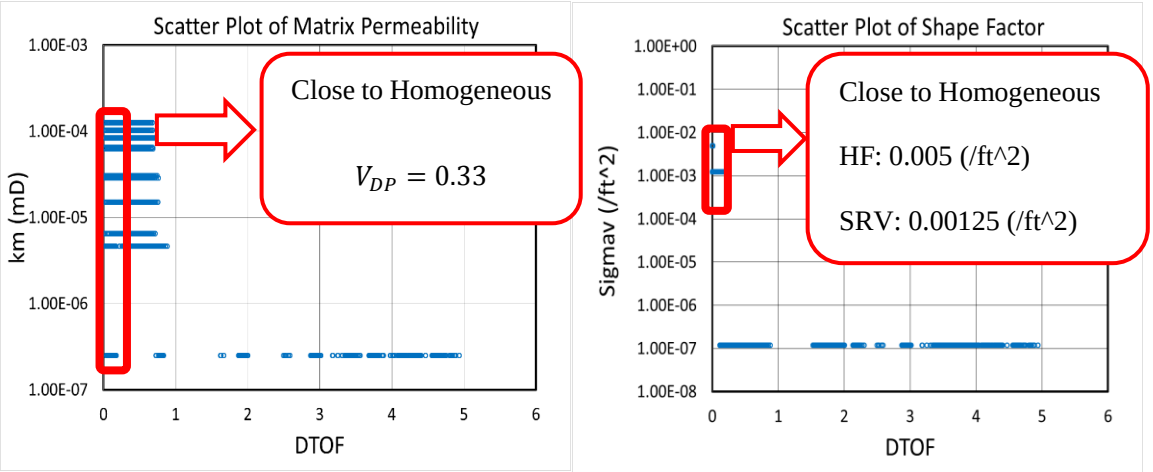

Fig. 4.41 – Scatter Plots of Permeability and Shape Factor in Matrices (Matrix Permeability, Left and Matrix Shape Factor, Right)

4.6 Conclusion

In this chapter, averaging methods were extended into multi-phase flow. Through this process, the five parameters were averaged: matrix permeability, matrix porosity, shape factor, density (initial pressure) and initial saturation. As for matrix porosity, the volumetric based averaging is taken so that the mass balance equation should hold. In the use of a volumetric averaging method, the corresponding errors stay small regardless of the size of the average and standard deviation. In terms of permeability and shape factor, the four approaches were tried: arithmetic, harmonic, geometric and incomplete layer. Among them, the range of the error calculated from harmonic averaging was quite wide, which indicated the harmonic method is most unstable. In contrast, the geometric and incomplete layer based averages tend to generate quite stable errors regardless of the size of the average and standard deviation. In terms of the remaining parameters, the initial pressure and initial saturation, were averaged so that the mass balance in each FMM grid

should be preserved. Lastly, the field application was conducted based on the averaging approach expressed in this chapter. These results show that by taking an appropriate averaging approach, FMM based DPSP simulator is applicable for heterogeneous reservoir models even in the presence of fracture heterogeneity.

CHAPTER V

CONCLUSIONS AND RECOMMENDATIONS

5.1 Conclusions

This research is focused on the developments of the DTOF theory for heterogeneous dual porosity reservoirs.

In **Chapter II** of this study, a Multi-stencil Fast Marching Method was introduced to improve the accuracy of Diffusive Time of Flight (DTOF) calculation. Originally, a Fast Marching Method has taken into account only directly adjacent cells to derive DTOF, which end with smaller transmissibility than that of the commercial softwares. In this research, the derivation of a more accurate DTOF is achieved by considering the diagonal cells in addition to the directly adjacent cells. In the end, the Multi-stencil Fast Marching is tested using the homogeneous and heterogeneous reservoir models both in the 2-D and 3-D cases. In all the cases, the improvement of the accuracy in terms of error is observed.

In **Chapter III** of this study, the Fast Marching Method was applied into heterogeneous dual porosity reservoir models (DPSP). In this method, Fast Marching grids are generated based on DTOF of fracture and with the requirement that matrix grids belong to their fracture grids. Thus, appropriate averaging methods for matrix properties are investigated so that they select the most representative parameters among the heterogeneous matrices. In this process, the three parameters are averaged: the matrix permeability, the matrix porosity and the shape factor. This study proves that, by taking an appropriate averaging

approach, the DPSP based FMM simulator is applicable for highly heterogeneous reservoirs.

In **Chapter IV of this study**, Fast Marching Method is extended to the multi-phase reservoir models. In this case, it is necessary to consider more parameters, saturation and density, to be averaged so that mass balance in each grid should be preserved. Besides, some case studies not only with heterogeneous matrix properties but also with heterogeneous fracture properties are conducted in order to show the robustness of this method. Finally, the wide applicability of FMM is proved in the use of the actual reservoir field data. This study verifies that the appropriate averaging method enables the DPSP based FMM simulator to be applicable for highly heterogeneous reservoirs in the multi-phase flow.

5.2 Recommendations

5.2.1 Vertex Based FMM

In this research, DTOF is calculated based on cell centered nodes. In this process, the travel time of the pressure front between adjacent cells is calculated by the summation of the travel time from the center to face of the seed grid and then from the face to the center of the adjacent cell. Based on the DTOF at the center of the each cell, DTOF at each grid face is back-calculated by taking the arithmetic average of the two adjacent cells. However, the travel time of these two can be significantly different in the case of highly heterogeneous reservoirs, which can generate the inaccurate DTOF at the grid face. Regarding the problem, vertex based FMM can solve the issue. In this approach, the

DTOF is calculated at each vertex of the grid, and it is obtained at cell center by linear interpolation. Since the travel time inside a grid is constant, this method can generate more accurate DTOF at grid face.

5.2.2 Anisotropic Case

In this research, Multi-stencil FMM is investigated in isotropic reservoirs. However, in the actual complex reservoirs, the permeability of horizontal direction can be different from that of vertical direction with respect to the sedimentary environment. The 5-stencil FMM (2-D) and 7-stencil FMM (3-D) can be applied to anisotropic models. However, the current multi-stencil FMM cannot because it needs to consider the velocity along each diagonal direction from the input data about the vertical and horizontal velocity so that it does not violate the causality. As for the further explanation of the causality problem, please look at the paper by Yang. et. al (2017).

5.2.3 Gravity Effect

In this research, all the results generated by FMM are compared with that of commercial software based on the assumption that there is no gravity effect. This is because DTOF is calculated only from fluid diffusivity (fluid velocity) in each grid which is determined by permeability, porosity, viscosity and total compressibility. More accurately in 3-D reservoir models, it is necessary to account for the gravity effect to calculate the velocity on top of these properties. Although it is not difficult to consider gravity effect in case of the single phase flow, the fluids start to segregate by phase in case of the 3-D models (i.e. the gas phase at the top of the reservoir, the oil phase at the middle and the water phase at

the bottom). Since FMM cannot consider the gas-oil and oil-water contact, it is necessary to handle the phase segregation properly, if the gravity effect is accounted for.

5.2.4 Averaging the Fluid Properties with Different Table Data

In this research, the pressure or saturation dependent fluid properties, such as formation volume factor, fluid velocity and relative permeability, are supposed to be determined based on only one table data. However, in the quite complex reservoirs, there are several tables of data for each fluid property for which each property is governed. In this kind of situation, it is necessary to generate the best representative table data set, from the sets of table data, for each fluid property because FMM cannot consider several table data sets for fluid properties.

REFERENCES

Ambegaokar, V., Halperin, B.I., and Langer, J.S. 1971. Hopping Conductivity in Disordered Systems. *Physical Review B* **4** (8): 2612-2620.

Atsushi Iino, Aditya Vyas, Jixiang Huang and Akhil Datta-Gupta 2017. Efficient Modeling and History Matching of Shale Oil Reservoirs Using the Fast Marching Method: Field Application and Validation. Paper SPE-185719-MS presented at the 2017 SPE Western Regional Meeting held in Bakersfield, California, USA, 23 April.

Brouwer, G.K., Fokker, TNO., et al. 2013. Upscaling and Downscaling with an Effective Medium Theory, Applied to Heterogeneous Reservoir. Paper SPE-164803-MS presented at the EAGE Annual Conference & Exhibition incorporation SPE Europec held in London, United Kingdom, 10-13 June 2013.

Browning, J., Ikonnikova, S., Gulen, G., and Tinker, S.W. 2013. Barnett Shale Production Outlook. *SPE Economics & Management* **5** (3): 89-104.

Cardwell, W. T., and R. L. Parsons, Average permeabilities of heterogeneous oil sands, Trans. Am. Inst. Min. Metall. Pet. Eng., 160, 34-42, 1945.

Chaitanya, K., King, M. J., Datta-Gupta, A., 2014. Diffuse Source Transmissibility Upscaling. Master of Science Thesis, Texas A&M University: 1-22.

Civian, F. 2010. Effective Correlation of Apparent Gas Permeability in Tight Porous Media. *Transport in Porous Media* **82** (2): 375-384.

Civian, F., Rai, C.S., and Sondergeld, C.H. 2011. Shale-Gas Permeability and Diffusivity Inferred by Improved Formulation of Relevant Retention and Transport Mechanisms. *Transport in Porous Media* **86** (3): 925-944.

Datta-Gupta, A, King, M. J., Xie, J., Gupta, N. et al. 2011. Radius of Investigation and its Generalization to Unconventional Reservoirs. *Journal of Petroleum Technology* 63: 52-55.

Dijkstra, E.W. 1959. A Note on Two Problems in Connection with Graphs. *Numerische Mathematik* **1**: 269-271.

Ertekin, T., King, G.R., and Schwerer, F.C. 1986. Dynamic Gas Slippage: A Unique Dual-Mechanism Approach to the Flow of Gas in Tight Formations. *SPE Formation Evaluation* **1** (1): 43-52.

Farmer, C.L. 2002. Upscaling: A Review. *International Journal for Numerical Methods in Fluids* **40** (1-2): 63-78. DOI: 10.1002/fld.267

Florence, F.A., Rushing, J.A., Newsham, K.E., and Blasingame, T.A. 2007. Improved Permeability Prediction Relations for Low-Permeability Sands. Paper SPE-107054 presented at the SPE Rocky Mountain Oil & Gas Technology Symposium, Denver, Colorado, USA, 16-18 April.

Fujita, Y., Datta-Gupta, A, King, M. J., 2014. Fast Marching Method with Multiphase Flow and Compositional Effects. Master of Science Thesis, Texas A&M University: 1-129.

Huang, J., Datta-Gupta, A, King, M. J., 2017. Analysis of Hydraulic Fracture Propagation and Well Performance Using Geomechanical Models and Fast Marching. Doctor of Philosophy Thesis, Texas A&M University: 89-135.

Javadpour, F., Fisher, D., and Unsworth, M. 2007. Nanoscale Gas Flow in Shale Gas Sediments. *Journal of Canadian Petroleum Technology* **46** (10): 55-61.

Javadpour, F. 2010. Nanoscale and Apparent Permeability of Gas Flow in Mudrocks (Shale and Siltstone). *Journal of Canadian Petroleum Technology* **48** (8): 16-21.

Jones, F.O., and Owens, W.W. 1980. A Laboratory Study of Low-Permeability Gas Sands. *Journal of Petroleum Technology* **32** (9): 1631-1640.

Kasap, E., Lake, L.W., et al. 1990. Calculating the Effective Permeability Tensor of a Gridblock. *Society of Petroleum Engineers Journal*: SPE-18434-PA.

Kelkar, M., Perez, G., et al. 2002. Applied Geostatistics for Reservoir Characterization. *Society of Petroleum Engineers*:189-209, 246-248.

King, P.R. 1989. The Use of Renormalization for Calculating Effective Permeability. *Transport in Porous Media* **4** (1): 37-58. DOI: 10.1007/bf00134741

King, M.J., 2007. Upgridding and Upscaling: Current Trends and Future Directions. Paper SPE-112810-DL General based on a speech presented as a Distinguished Lecture during the 2006-2007 season.

Klinkenberg, L.J. 1941. The Permeability of Porous Media to Liquid and Gases. *API Drilling and production Practice,* 200-213.

Lee, J., Rollins, J.B., Spivey. J.P., et al. 2003. Pressure Transient Testing. *Society of Petroleum Engineers*. ISBN 1-55563-099-5: 41-61.

Michel, G.G., Sigal, R.F., Civan, F., and Devegowda, D. 2011. Parametric Investigation of Shale Gas Production Considering Nano-Scale Pore Size Distribution, Formation Factor, and Non-Darcy Flow Mechanisms. Paper SPE-147438 presented at the SPE Annual Technical Conference and Exhibition, Denver, Colorado, USA, 30 October-2 November.

Nelson, P.H. 2009. Pore-throat Sizes in Sandstones, Tight Sandstones, and Shales. *AAPG Bulletin* **93** (3): 329-340.

Renard, P. and de Marsily, G. 1997. Calculating Equivalent Permeability: A Review. Advances in Water Resources Vol. 20 Issues 5–6: 253-278. DOI: http://dx.doi.org/10.1016/S0309-1708(96)00050-4

Sabry, M., Aly, A., et al. 2007. Multistencils Fast Marching Methods: A Highly Accurate Solution to the Eikonal Equation on Cartesian Domains. IEEE Transactions on Pattern Analysis and Machine Intelligence Vol 29, No. 9: 1-7

Sampath, C.W, and Keighin, K. 1982. Factors Affecting Gas Slippage in Tight Sandstones of Cretaceous Age in the Uinta Basin. *Journal of Petroleum Technology* **34** (11): 2715-2720.

Swami, V., Clarkson, C.R., and Settari, A.T. 2012. Non Darcy Flow in Shale Nanopores: Do We Have a Final Answer?. Paper SPE-162665 presented at the SPE Canadian Unconventional Resource Conference, Calgary, Canada, 30 October-1 November.

Sethian, J.A. 1996. *Level Set Method*. Cambridge University Press, New York City.

Sethian, J.A. 1999. *Level Set Methods and Fast Marching Methods*. Cambridge University Press, New York City.

U.S. Energy Information Administration. 2013. *Annual Energy Outlook 2013 with Projections to 2040*, http://www.eia.gov/forecasts/aeo/pdf/0383(2013).pdf.

Wang, Z., Li, C., King, M.J., 2017. Validation and Extension of Asymptotic Solutions of Diffusivity Equation and Their Applications to Synthetic Cases. Paper SPE-182716-MS presented at the SPE Reservoir Simulation Conference held in Montgomery, TX, USA, 20-22 February 2017.

Xie, J., Datta-Gupta, A, King, M. J., Application of Level Set and Fast Marching Methods in Reservoir Characterization. Doctor of Philosophy Thesis, Texas A&M University: 37-52.

Yang, C., Xue, X., King, M. J., Datta-Gupta, A., 2017. Flow Simulation of Complex Fracture Systems with Unstructured Grids using Fast Marching Method. Unconventional Resources Technology Conference, Austin, Texas, USA, 24-26 July. URTEC-2691393-MS. http://dox.doi.org/10.15530/urtec-2017-2691393.

Zhang, Y., Bansal, N., Fujita, Y., Datta-Gupta, A., King, M. J., et al. 2014. From Streamlines to Fast Marching: Rapid Simulation and Performance Assessment of Shale Gas Reservoirs Using Diffusive Time of Flight as a Spatial Coordinate. Paper SPE-168997-MS presented at the SPE Unconventional Resources Conference – USA held in The Woodlands, Texas, USA, 1-3 April.

Zhang, Y., Datta-Gupta, A., King, M. J., 2013. Dynamic Reservoir Characterization Using Complex Grids Based on Streamline and Fast Marching Methods. Doctor of Philosophy Thesis, Texas A&M University: 68-96.